

## ABSTRACT

Title of Document:                    **SPRAY DROPLET GENERATION BY  
BREAKING WATER WAVES.**

  David M. Towle, M.S., 2014

Directed By:                            Dr. James H. Duncan, Mechanical Engineering

This thesis presents the results of an experiment in which the generation of spray droplets in two mechanically generated plunging breaking water waves was investigated. In both breaking waves, the wind velocity at the free surface was zero and droplets were produced only by means of plunging jet impact, free surface turbulence and bubble bursting. The free surface was kept free of particulates and surfactants for each wave in one set of measurements, while in a second set of experiments, using only the higher amplitude wave, the tank water was mixed with a soluble surfactant.

The experiment was able to deliver information on the diameter distributions of droplets produced in both waves. Also, the positional and time dependence of droplet production throughout the stages of wave breaking was investigated.

Ultimately, it was determined that under these conditions droplet frequency is influenced primarily the impact of the plunging jet with the front face of the wave. Higher amplitude waves generally lead to markedly higher amounts of droplets

produced and a shift towards higher diameters. The addition of surfactant reduced the diameter and suppressed the production of spray droplets. The positional distribution of droplet production within the wave was also altered significantly by the presence of surfactant: droplets were more evenly produced throughout the breaking zone in the wave with surfactant, whereas the wave generated in clean water had a much smaller region of significant droplet production.

SPRAY DROPLET GENERATION BY BREAKING WATER WAVES.

By

David M. Towle

Thesis submitted to the Faculty of the Graduate School of the  
University of Maryland, College Park, in partial fulfillment  
of the requirements for the degree of  
Master of Science  
2014

Advisory Committee:  
Professor James H. Duncan, Chair  
Professor Kenneth T. Kiger  
Assistant Professor Johan Larsson

© Copyright by  
David M. Towle  
2014



## Acknowledgements

Many thanks is due to my advisors Dr. Duncan and Dr. Liu for pushing me through the process of getting all of the research and writing done in less than a year. Thanks to Dan Wang for providing the ground work on the project and Dai for producing some of the code used to complete the data processing.

# Table of Contents

Acknowledgements.....	iii
Table of Contents.....	iv
List of Tables.....	v
List of Figures.....	vi
Chapter 1: Introduction.....	1
Chapter 2: Experimental Setup.....	10
Chapter 3: Diameter Dependent Out-of-Focus and Depth-of-Field Corrections.....	24
Chapter 4: Droplet Measurement and Results for the 0.074 Amplitude Wave.....	51
Chapter 5: Droplet Measurement and Results for the 0.070 Amplitude Wave.....	69
Chapter 6: Droplet Measurement and Results for the Surfactant Wave.....	80
Chapter 7: Wave Comparison and Concluding Remarks.....	90
Bibliography.....	99

## List of Tables

Table 1.1 .....	7
Table 2.1 .....	14
Table 4.1 .....	53
Table 7.1 .....	93



## List of Figures

Figure 1.1 .....	2
Figure 1.2 .....	3
Figure 1.3 .....	4
Figure 1.4 .....	5
Figure 2.1 .....	11
Figure 2.2 .....	16
Figure 2.3 .....	17
Figure 2.4 .....	22
Figure 2.5 .....	22
Figure 2.6 .....	23
Figure 3.1 .....	25
Figure 3.2 .....	26
Figure 3.3 .....	27
Figure 3.4 .....	28
Figure 3.5 .....	28
Figure 3.6 .....	29
Figure 3.7 .....	30
Figure 3.8 .....	30
Figure 3.9 .....	31
Figure 3.10 .....	32
Figure 3.11 .....	34
Figure 3.12 .....	35
Figure 3.13 .....	37
Figure 3.14 .....	38
Figure 3.15 .....	39
Figure 3.16 .....	42
Figure 3.17 .....	43
Figure 3.18 .....	45
Figure 3.19 .....	46
Figure 3.20 .....	48
Figure 3.21 .....	49
Figure 3.22 .....	49
Figure 3.23 .....	50
Figure 4.1 .....	52
Figure 4.2 .....	52
Figure 4.3 .....	54
Figure 4.4 .....	55
Figure 4.5 .....	57
Figure 4.6 .....	58

Figure 4.7 .....	59
Figure 4.8 .....	59
Figure 4.9 .....	62
Figure 4.10 .....	65
Figure 4.11 .....	66
Figure 4.12 .....	67
Figure 4.13 .....	68
Figure 5.1 .....	70
Figure 5.2 .....	71
Figure 5.3 .....	72
Figure 5.4 .....	73
Figure 5.5 .....	73
Figure 5.6 .....	74
Figure 5.7 .....	76
Figure 5.8 .....	77
Figure 5.9 .....	78
Figure 5.10 .....	79
Figure 5.11 .....	79
Figure 6.1 .....	80
Figure 6.2 .....	81
Figure 6.3 .....	82
Figure 6.4 .....	83
Figure 6.5 .....	84
Figure 6.6 .....	84
Figure 6.7 .....	85
Figure 6.8 .....	86
Figure 6.9 .....	87
Figure 6.10 .....	88
Figure 6.11 .....	89
Figure 6.12 .....	89
Figure 7.1 .....	92
Figure 7.2 .....	94
Figure 7.3 .....	95
Figure 7.4 .....	96
Figure 7.5 .....	98



# Chapter 1: Introduction

The investigation of sea spray generation is a topic of significant oceanographic and climatological interest. Droplet evaporation plays an integral role in the transfer of heat to the atmosphere and the formation and strengthening of tropical cyclones (Andreas, 2001 and Wang, 2001). Aside from heat transfer, droplet production greatly influences the mass flux of aerosols at this interface. Sea spray droplet evaporation is second only to wind-blown dust in the introduction of suspended particles into the atmosphere (Hoppel, et al., 2002). The aerosol production of sea spray additionally affects numerous chemical phenomena in the atmosphere (Erickson, et al., 1999).

## 1.1 Previous Research in the Field of Sea Spray Generation

Much of the body of research conducted in the area of sea spray production focuses on two primary means: droplets torn from the crests of waves by wind and droplets produced from the bursting of bubbles at the sea surface (Norris, et al., 2013). A multitude of studies have been conducted—in the environment and in the laboratory—in an attempt to characterize droplet production rates and size distributions. The predictions of a number of these models for droplet generation were consolidated and are displayed in Figure 1.1 (Andreas, 1998).

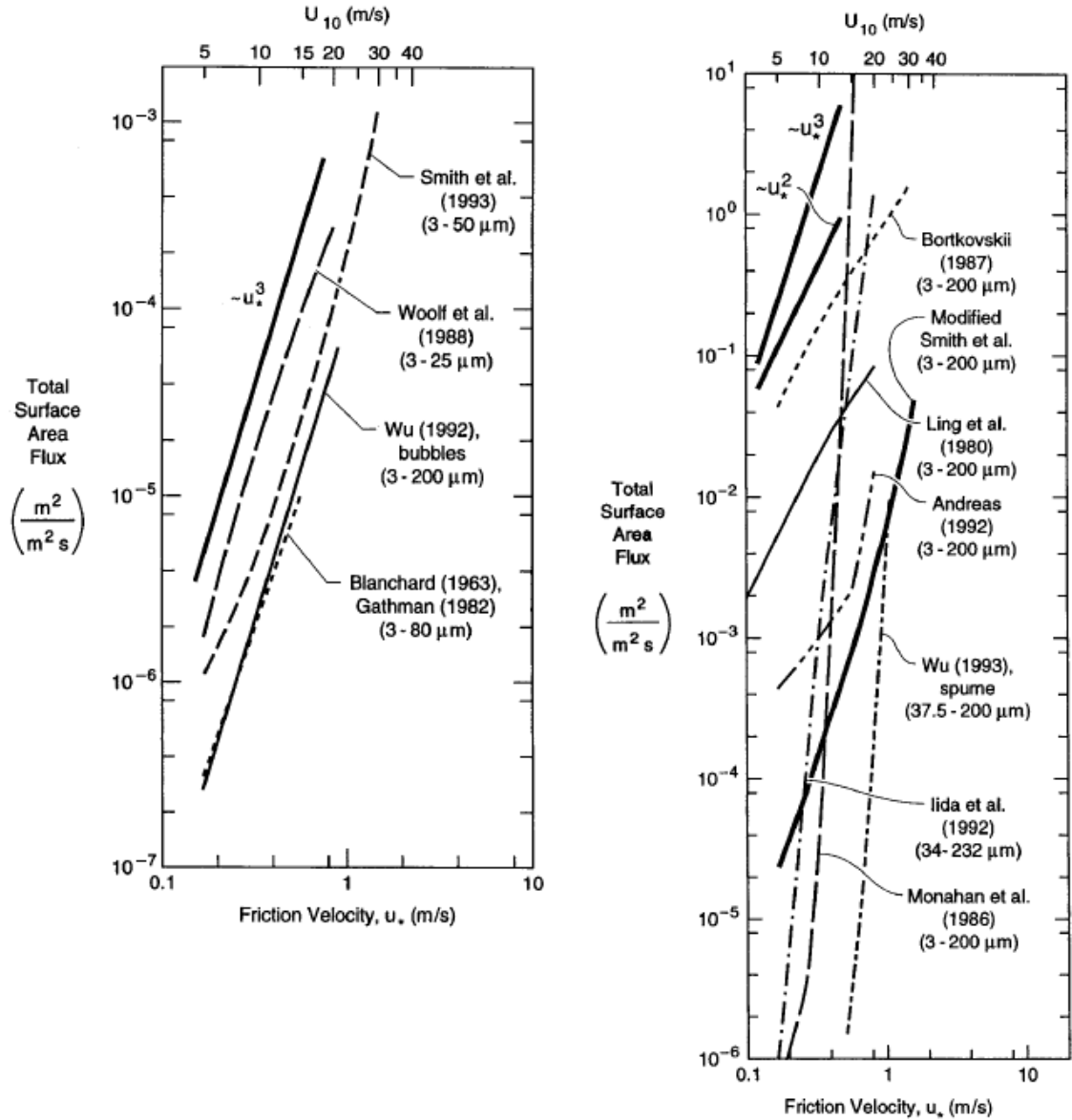
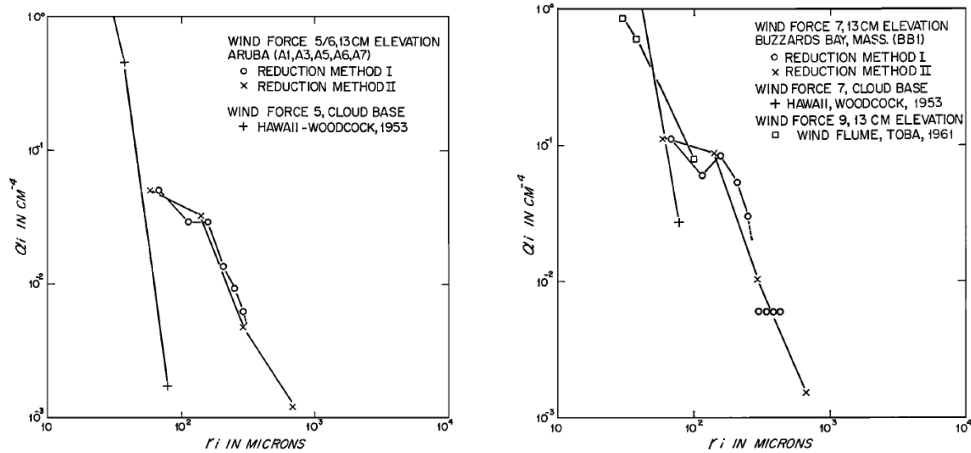


Figure 1.1: Summary of droplet surface flux models consolidated by Edgar Andreas.

As evidenced by these plots, there is significant variation between the models. Because of this, any investigation into the production of spray droplets is highly dependent upon the experimental configuration, the range of droplet diameters capable of being detected and the environmental conditions under which the experiment is

conducted. Nevertheless, some agreement in the role of certain phenomena and governing distributions can be seen in the literature.

One of the first attempts to characterize the concentration and size distribution of sea spray was conducted by Edward Monahan during 1964 and 1965. These experiments were conducted at sea from a raft-mounted camera using a shadowgraph technique. He published his results in a paper three years later (Monahan, 1968). Two of his droplet diameter distributions are displayed in Figure 1.2.



**Figure 1.2: Droplet diameter distributions as a function of droplet radius in  $\mu\text{m}$  from Monahan’s Experiment (1968).**

Though admittedly lean on data, Monahan’s work nevertheless set the precedent for a number of follow-on experiments that sought to better characterize droplet distributions under varying ocean and laboratory conditions. His methodology of using shadowgraph photography in the ocean environment was repeated many times over.

In further investigations conducted in the open ocean, Wu et al. (1984) concluded also that droplet diameter distributions were segmented into two regions. Furthermore, this study concluded that the shape of the distribution was independent of the elevation

above the free surface and the wind velocity. Figure 1.3 shows the diameter distributions from this study and Figure 1.4 shows the droplet flux as a function of radius.

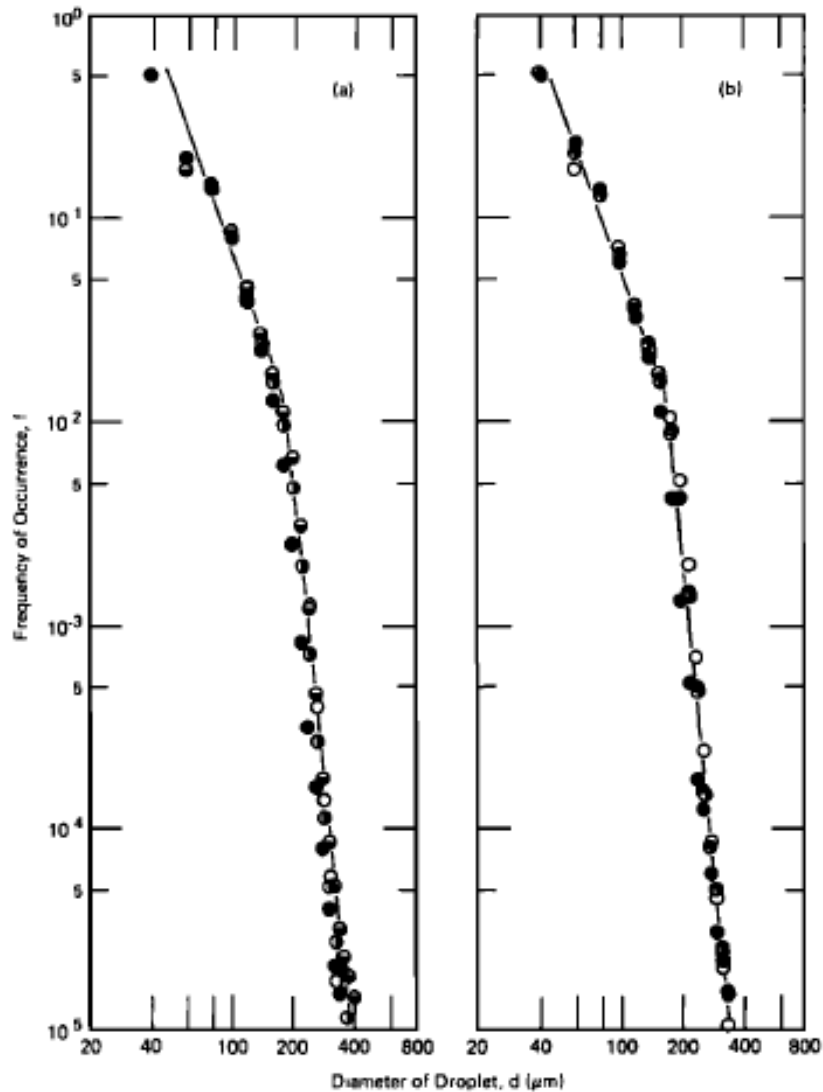


Figure 1.3: Droplet diameter distributions in open ocean sea spray. Plot on the left is for 13 and 18 cm above the free surface and 10 meter wind velocities of 6.4, 7.5 and 8.0 m/s. Plot on the right is for 30, 50, 70 and 90 cm above the free surface and 10 meter wind velocities of 6.0 and 7.5 m/s (Wu, 1984).

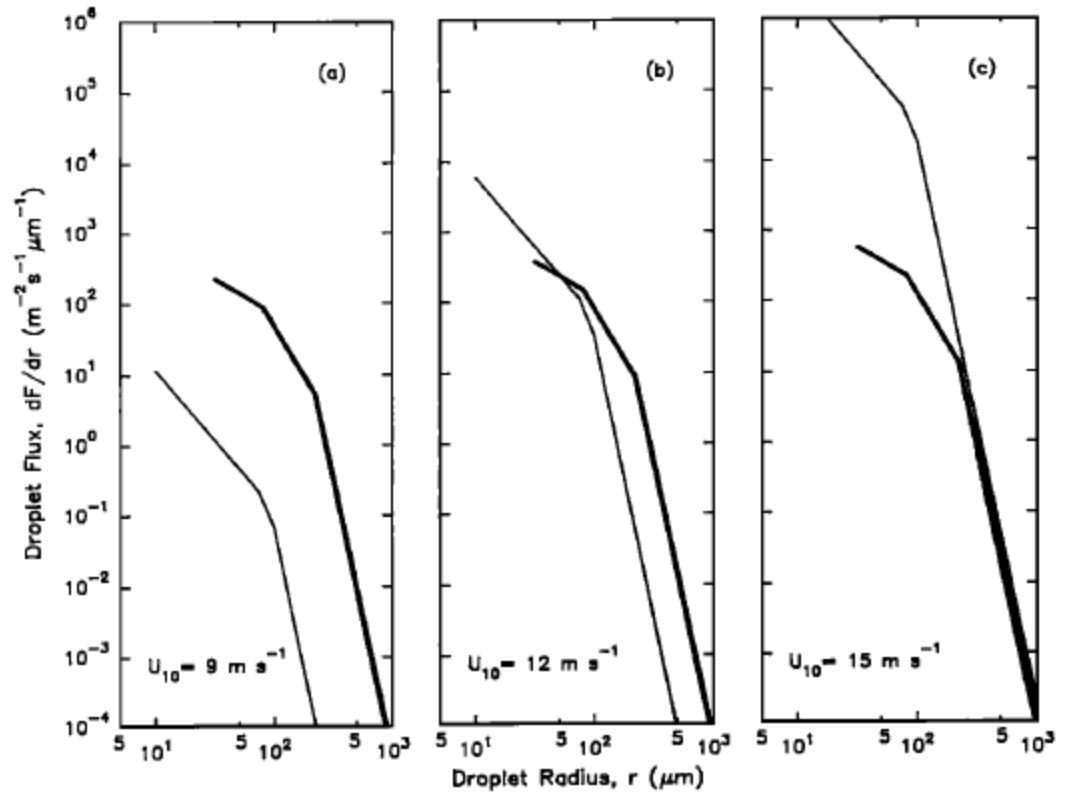


Figure 1.4: Droplet flux as a function of droplet radius (Wu, 1993).

Whereas characterizing sea spray generation in ocean waves is most valid in experiments that are conducted in the field, studies conducted in a laboratory are relevant for their ability to consistently and quickly replicate waves with controlled parameters. Thus, numerous studies have been carried out with mechanically generated waves and wind. Bonmarin (1989), Melville and Rapp (1988) and Rapp and Melville (1990) are among some of the significant studies conducted using this methodology. Additionally, Duncan et al, (1994 and 1999) and Qiao and Duncan (2001) investigated mechanically generated spilling breakers with wavelengths from 0.77 m to 1.2 m.

These laboratory investigations of waves have been conducted both with and without surfactants. Ocean surface tension can vary widely from 73.2 mN/m in the



cleanest water to 55 mN/m in near-shore locations. In some cases, where the presence of surfactants is exceptionally high, surface tensions less than 40 mN/m have been observed (Frysinger, 1992). To some extent, surfactants influence ocean surface tension even for relatively clean, organism-free water (Liss, et al., 1997).

It has been concluded that surfactants play a major role in ocean wave dynamics. After analyzing his data and some from other researchers (Cox and Munk, 1954, Barger et al., 1970, Ermakov et al., 1986 and Croswell, 1982) Wu came to the conclusion that surfactants diminish the amplitude of waves from 2 to 40 cm in conditions where the wind speeds do not exceed 7 m/s. Waves exposed to surfactants exhibited decreased slopes over those generated in clean water according to studies conducted by Tang and Wu (1992) and Bock et al. (1999). Additionally, it has been shown experimentally by Liu and Duncan (2003 and 2006) that surfactant films reduce the number and amplitude of capillary waves until their presence is completely eliminated and replaced by small plunging jets when the surface tension is extremely low.

Droplet generation has been shown to favor smaller diameters in the presence of surfactants by Sellegri et al. (2006). The reduction in surface tension enables smaller droplets to be produced in higher quantities. Simultaneously, the reduction in wave amplitude with decreasing surface tension contributes significantly to the overall production of spray droplets.

## 1.4 Droplet Production Mechanism in Waves

There are four general means by which droplets can be generated in waves. The names assigned to these mechanisms for this paper are stated below in Table 1.1. Spume droplets constitute a large part of the droplets considered in the literature up to this point. Jet and film droplets are even more important when considering sea spray that is present at more than a meter from the free surface. This is because jet and film droplets are relatively small and can be carried aloft by wind conditions at the surface. Splashing droplets—which are generally large like spume droplets—are another means of droplet production that is driven by the wave motion itself. Practically, it is difficult to distinguish jet and film droplets unless the camera is angled such that the free surface is in view. In laboratory experiments where wind is not present, the larger droplets will be exclusively produced via the splashing mode.

**Table 1.1: Means of droplet production in breaking waves.**

<b><u>Droplet Name</u></b>	<b><u>Means of Production</u></b>
Spume	Sheared from wave surface by wind
Splashing	Ejected from wave due to turbulence and impact of wave crest
Jet	Central water column produced in bubble bursting
Film	Bursting of bubble envelope

## 1.5 Areas Requiring Further Investigation

This project sought to investigate the character of spray droplets created solely from mechanically generated breaking waves in clean water. Unlike waves found in most ocean conditions, which are influenced by the local wind, this experiment only considered the dynamics of the wave and its effect on droplet production. The droplet diameter distributions and time-dependent and position-dependent droplet production was investigated. Additionally, the effect of turbulence-generated versus bubble-generated droplets on these parameters was sought.

## 1.6 Overview

In this thesis, an experimental study of droplets produced by mechanically generated plunging breaking waves in clean water and in water mixed with a soluble surfactant is presented. The temporal history of the wave profiles during breaking are measured with a cinematic laser induced fluorescence technique and the droplets are measured with a cinematic pulse shadowgraph technique. This work is described in the following chapters. The experimental setup is described in Chapter 2. This is followed in Chapter 3 by a detailed description of the calibration methods used for the droplet measurements. The results are then presented in Chapters 4, 5 and 6. Finally, analysis and conclusions from this experimental study are presented in Chapter 7.

## Chapter 2: Experimental Setup

### 2.1 Wave Tank

The experiments were performed within a 14.8m long by 1.22m wide wave tank with a water depth of 0.909m (3 feet). At one end of the tank are a wedge-shaped programmable wave maker and a set of two 7.5 hp fans that blow air at speeds up to 10 m/s through honeycomb flow straighteners across the free surface. Though these fans were used in other experiments to simulate wave-wind interactions, in this series of experiments the air above the water surface was kept calm. A beach is located at the end of the tank opposite to the wave maker. This beach is used to dissipate wave energy. A water surface skimmer is also located behind the beach and is used to remove particulate or surfactants from the free surface. From the skimmer, the water is directed through a filtration system before being returned to the tank near the wave maker assembly. The walls of the tank consist of Plexiglas windows separated by steel supporting columns. The entire series of wave and droplet measurements were conducted within one of the Plexiglas windows. The beginning of this window is approximately 60 inches from the minimum carriage position. Figure 2.1 illustrates the setup of the full wave tank. Not depicted in Figure 2.1 is the moveable instrument carriage which is supported on the top of the wave tank on four hydrostatic oil bearings. In the present experiments, the measurement systems were mounted on the instrument carriage, which was held in a fixed position during each breaking wave event.

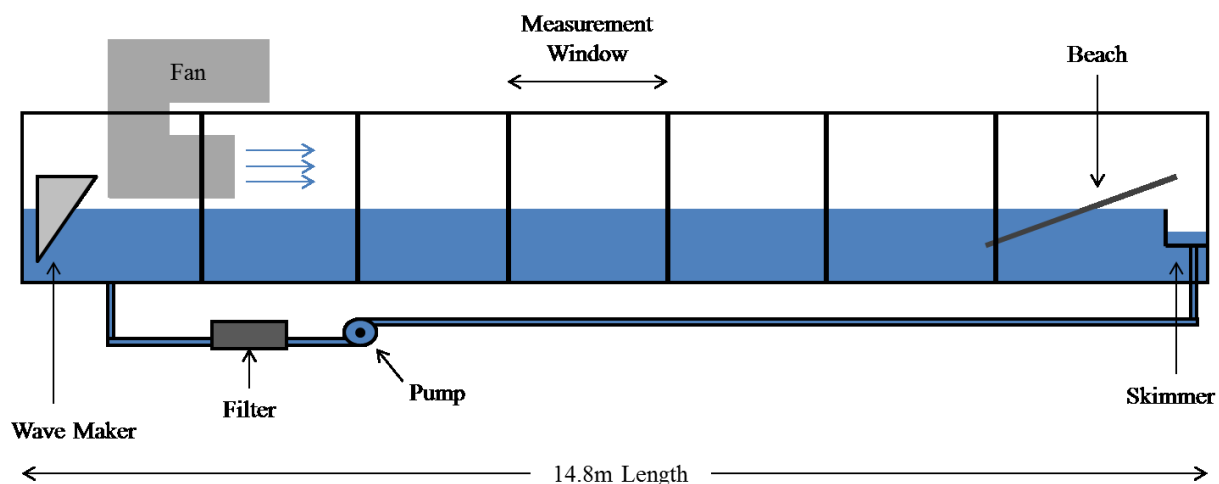


**Figure 2.1: Schematic of full wave tank as configured for experiments.**

At the beginning and end of a series of wave runs the surface tension of the water within the tank was measured and recorded. Water from inside the tank was siphoned to a three liter beaker and allowed to overflow so that the surface of this sample was skimmed of particulates and surfactants. Then, a Wilhelmy Plate tensiometer from NIMA was used to record the surface tension continuously for the duration of the experimental runs (up to 12 hours on some occasions). In measurements of this type, the initial surface measurement is the surface tension of clean water. Then, as surfactants adsorb on the water surface, the surface tension drops. In all cases in the present experiments, the surface tension remained at the clean water surface tension for the entire duration of the experimental runs. This indicates that during the breaking wave experiments, the surface was essentially surfactant free.

## 2.2 Wave Generation

The breaking waves were generated by a dispersive focusing technique. In this technique, a packet of wave composed of 32 frequency components is generated in manner such that the packet focuses to a single wave at position  $x_b$  and time  $t_b$ . The amplitudes of these waves were high enough such that a breaking wave was formed at the focal point. This technique is described briefly below; a detailed description can be found in (Duncan, et. al 1999). The wave maker motion is given by:

$$z_w(t) = w(t) \frac{2\pi}{N} A \sum_{i=1}^N \frac{1}{k_i} \cos \left( x_b \left( \frac{\omega_i}{\bar{c}} - k_i \right) - \omega_i t + \frac{\pi}{2} \right)$$

where  $A$  is the overall wave maker amplitude,  $k_i$  and  $\omega_i$  are the wavenumber and frequency of the  $i$ th components and  $\bar{c}$  is given by the equation:

$$\bar{c} = \frac{\omega_i}{2k_i}$$

The leading term,  $w(t)$  is a window function that permits wave maker motion only when its contribution to the wave packet is significant and is given by:

$$w(t) = \frac{1}{4} [\tanh(\beta \bar{\omega}(t - t_1)) + 1][1 - \tanh(\beta \bar{\omega}(t - t_2))]$$

In this equation  $\beta$  is selected as 5.0 and  $\bar{\omega}$  is the average of the 32 frequencies. The times  $t_1$  and  $t_2$  were selected in a manner such that the desired waveform was created and are derived from the following equations:

$$t_1 = x_b \left( \frac{1}{\bar{c}} - \frac{1}{c_n} \right)$$

$$t_2 = x_b \left( \frac{1}{\bar{c}} - \frac{1}{c_1} \right)$$

For this series of experiments, three waves were investigated. Between them, only two parameters were changed enabling two comparisons to be drawn. The first comparison was between the wave amplitudes. The second investigated one wave with clean water, and then the same wave in a tank with surfactant. The control parameters, where  $h$  is the vertical distance between the mean water level and the vertex of the wedge,  $H$  is the water depth in the tank and  $\lambda_0 = 2\pi g/\bar{\omega}$ , are displayed below in Table 2.1.



**Table 2.1: Dimensionless parameters for both types of waves generated.**

<u>Parameter</u>	<u>Value</u>
$N$	32
$\frac{h}{2\pi g/\bar{\omega}^2}$	0.35792
$\frac{H}{2\pi g/\bar{\omega}^2}$	0.7458
$\frac{N\Delta\omega}{\bar{\omega}}$	0.77
$f_0 = \frac{\omega_0}{2\pi}$	1.15
$\frac{x_b}{\lambda_0}$	6.2

### 2.3 Wave Profile Measurement

In order to correlate droplet generation and behavior on the microscopic scale to phenomenon in the breaking wave behavior on the large scale, profile measurements of both the 0.074 and 0.070 amplitude waves were taken. For these measurements, a Phantom v9 camera with an image resolution of 1632x1200 was positioned at the mid-

point of the measurement window and angled downward at approximately  $30^\circ$  to view the horizontal profile of each passing wave. A 24 mm Nikon lens was fixed to the v9 for all measurements. In order for the images to yield quantitative measurements of the wave profile at the center plane of the tank, a Laser-Induced Fluorescence (LIF) technique was used (Liu and Duncan, 2006; Liu et al. 2003, Duncan et al 1999). In this technique, a vertically oriented light plane—produced from a 7 Watt Argon-Ion laser operating at 488 and 514 nm—was projected along the long axis of the tank mid-way between the Plexiglas windows. The water was mixed with Fluorescein dye which, when excited by the laser light sheet, emitted light in the green wavelength range. An optical filter was placed in front of the camera lens. This filter blocked out the laser light while transmitting the light from the glowing dye into the camera lens. Thus, specular reflections of laser light were eliminated. A schematic for this set-up is shown in Figure 2.2.

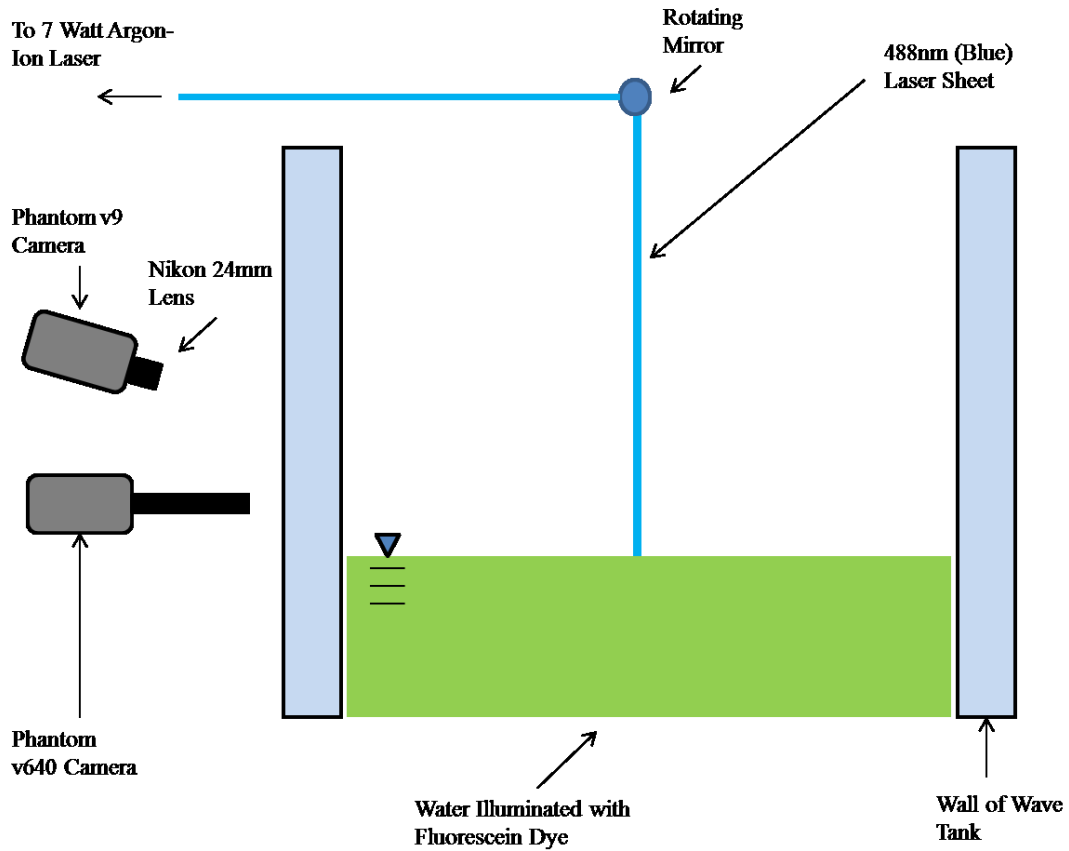
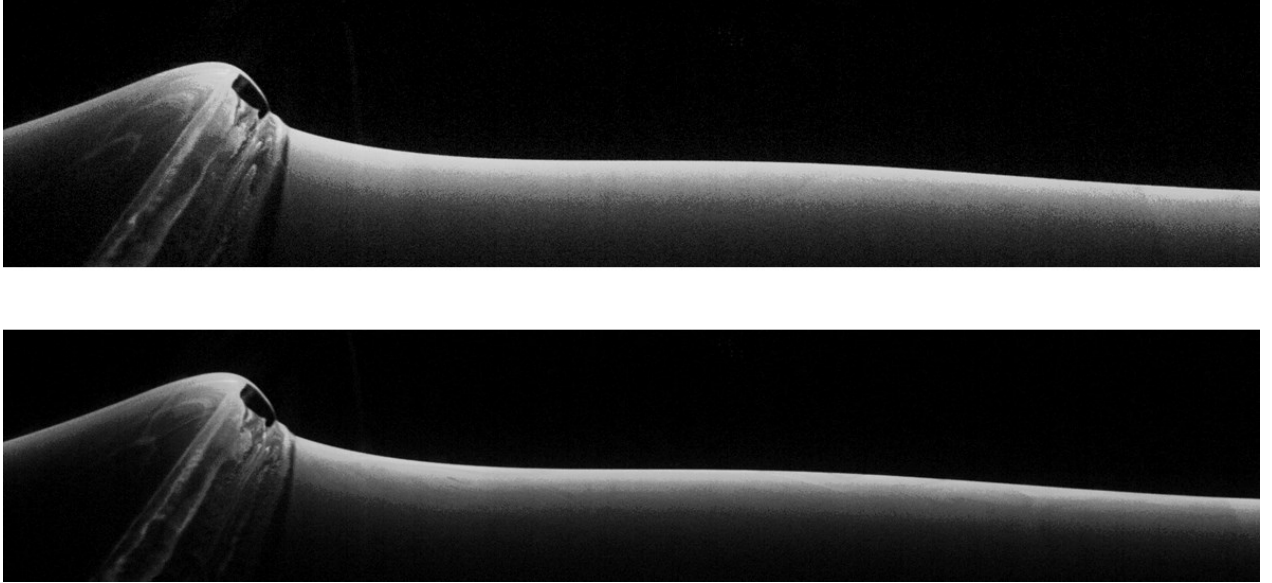


Figure 2.2: Schematic of the set-up for wave profile measurement.

The wave profiles from the movies generated by the v9 cameras spanned the width of the measurement window and recorded the full time that the breaking wave passed through this interval. One still image from each of the two wave profile movies is shown in Figure 2.4. These images show the jet in each wave just prior to impact.



**Figure 2.3: Still images from the profile movies of the 0.074 amplitude (Top) and 0.070 amplitude (bottom) waves at the instant of crest impact for each wave.**

## 2.4 Droplet Measurements

The droplet measurements were performed with a cinematic pulsed shadowgraph technique that employs an Nd:YLF pulsed laser and a high-speed digital movie camera fitted with a long distance microscope lens. The laser was a Photonics Industries DM50-527 designed for particle image velocimetry (PIV). The laser head was mounted on the instrument carriage and a set of optical components was used expand and re-direct the laser beam down from the top of the carriage to near the water level where it was split into two 5-cm-diameter beams. These beams were directed perpendicular to the tank walls and at the same height above the undisturbed water surface, see Figure 2.5. The laser was operated in PIV mode with a time delay of 200  $\mu\text{s}$  between pulses in each pulse pair. With this time delay, the typical displacement of the droplet images was a small

fraction of the total image width, thus enabling accurate measurements of droplet velocity.

The shadowgraph images were recorded by two Phantom v640 high-speed movie cameras which have sensor consisting of 12-bit pixels in a 2560 by 1600 array with a pixel pitch of 10  $\mu\text{m}$ . The cameras were fitted with Infinity K2 long-distance microscope lenses. The cameras were positioned on the opposite side of the tank from the incoming laser beams and oriented so that the beam axes were coincident with the optical axes of the camera lenses. The lenses were focused at the midplane of the tank and produced a 1 to 1 magnification ratio. This results in a resolution of 10  $\mu\text{m}/\text{pixel}$ . A sample shadowgraph image of droplets generated by a breaking wave is shown in Figure 2.6. (A detailed description of the calibration procedures and accuracy of the droplet measurements is presented in the following chapter.) The two cameras and laser beams were positioned 40.64 cm apart in the streamwise direction. The camera nearest the wave maker had a serial number ending in 9138 and for the purposes of naming, will hereafter be referred to as “Camera 9138.” The camera positioned further from the wave maker is named “Camera 9139” for precisely the same reason.

The time sequences of laser pulse pairs and camera images were controlled by an 8-channel digital time-delay device (Berkeley Nucleonics, Inc.). The device was set to send a 325 Hz trigger signal to the laser and a 650 Hz trigger signal to the camera. The laser control unit then produced two laser pulses with the above mentioned 200  $\mu\text{s}$  time delay between pulses for each trigger signal from the delay device. The phasing between the laser trigger signal and the camera trigger signal were adjusted so that each image received a single light pulse from the laser. The frame pair rate of 325 Hz chosen such

that approximately two seconds of data was recorded in each camera's internal memory per run. This time fully included the passage and breaking sequence of the wave packet through the measurement window.

The laser is nominally rated for a maximum output of 50 W in single pulse mode and a 1000 Hz frequency. Due to deterioration of the diode due to extensive use and excessive humidity, the maximum power of the laser during the course of the experiment was 32 W. Unfortunately, the laser's performance in twin pulse mode was only guaranteed at the maximum energy output. Since this was not possible for the reasons mentioned above, there were two difficulties that had to be overcome during the experiments. First, when manipulating the laser's controls, the energy distributions between the two pulses could not be made equal. A result of this was that one pulse would be brighter than the other. This led to some degree of complication with regards to data processing. Second, the manufacturer warned that time separation between the pulses might be inaccurate and vary from one pulse pair to another. To determine the accuracy of the laser pulse separation in each pulse pair, one of the Phantom v640 cameras was set to record 32x8 pixel images with a frame rate of 341,463 Hz and an exposure of 1.43 $\mu$ s. It was found that the laser consistently illuminated the camera with 325 pulse pairs per second with a separation of  $200 \pm 1.43 \mu$ s. Thus, despite the manufacturer's reservations, the laser pulse separation was deemed accurate enough to proceed with measurements.

## 2.4 Procedures and Plan of Experiments

Two investigations were undertaken. The first investigation dealt with the influence of wave maker amplitude on droplet generation. The wave maker motion for these two different waves had non-dimensionalized amplitude parameters ( $A/\lambda_0$ ) of 0.074 and 0.070. Since the wave maker motions are identical except for their respective amplitudes, the corresponding waves are hereafter referred to in this paper as the “0.070 Amplitude Wave” and the “0.074 Amplitude Wave”. It should be noted, however, that these amplitudes refer to the amplitude of the wave maker, not the amplitude of the wave it generates. The 0.070 amplitude wave is a weak plunging breaker and the 0.074 amplitude wave is a strong plunging breaker.

In the second investigation, surfactant was added to the tank and its effects on the 0.074 amplitude wave were observed. In this study, 50 mL of Triton X-100 surfactant manufactured by BASF were added to the tank and allowed to mix so that it was homogeneously distributed throughout the water. The water surface tension was reduced to 42.4 mN/m for the course of these runs. All of the measurements were taken continuously over 48 hours so as to minimize the deterioration of Triton X-100.

The wave profile measurements were done with the wave profile camera centered in the middle of the measurement window and with the water mixed with fluorescein dye. The droplets were measured in a separate set of experiments without dye in the water. For each wave maker motion, the droplets were measured at approximately 16 locations in a horizontal line located just above the highest point that the wave profile reaches. This resulted in the bottom of the images being located at 11 cm and 12 cm above the undisturbed water level for the 0.070 wave and the 0.074 wave, respectively. This

distance was chosen such that the wave crest would not be visible within the images yet pass just below the lower edge of this area.

Measurements were taken for 10 waves at each camera position. The manner in which this was carried out is detailed in Figure 2.5. For the complete measurement of one breaking condition, it was necessary to record 160 movies each consisting of 2 seconds of images and 10 GB of data apiece.

For each experimental run, the following procedure was followed. In order to ensure a clean water surface, the wind generation fans were operated at low speed for about 10 minutes to blow surfactants and any particulate matter that settled on the free surface down the tank towards the skimmer behind the beach between. Simultaneously, the pump and filter were operated. Following this, both the fans and pump were shut off and the free surface was allowed to calm. The calming of the free surface required at least an additional 10 minutes of waiting time between runs. While the surface was being cleaned and then calmed, the movies from the previous runs were written to an external hard drive. Saving these two 10 GB files required approximately 20 minutes which was consumed concurrently with the tank cleaning procedure. Surface tension was monitored periodically throughout the course of the runs. Once these steps were completed, another wave was generated, measurements were taken, and then the process was repeated over again.



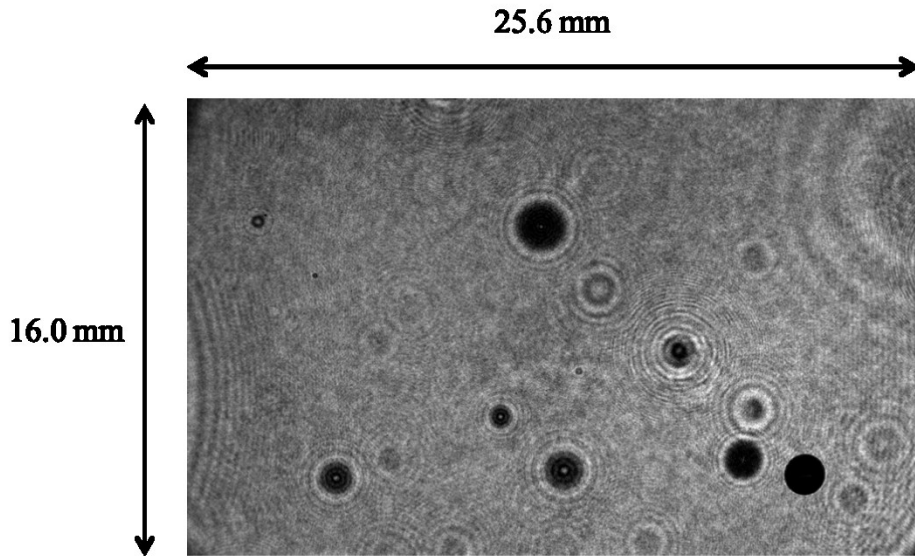


Figure 2.4: Still image through K2 microscopic lens showing droplets suspended in air. Image resolution is 2560x1600 pixels.

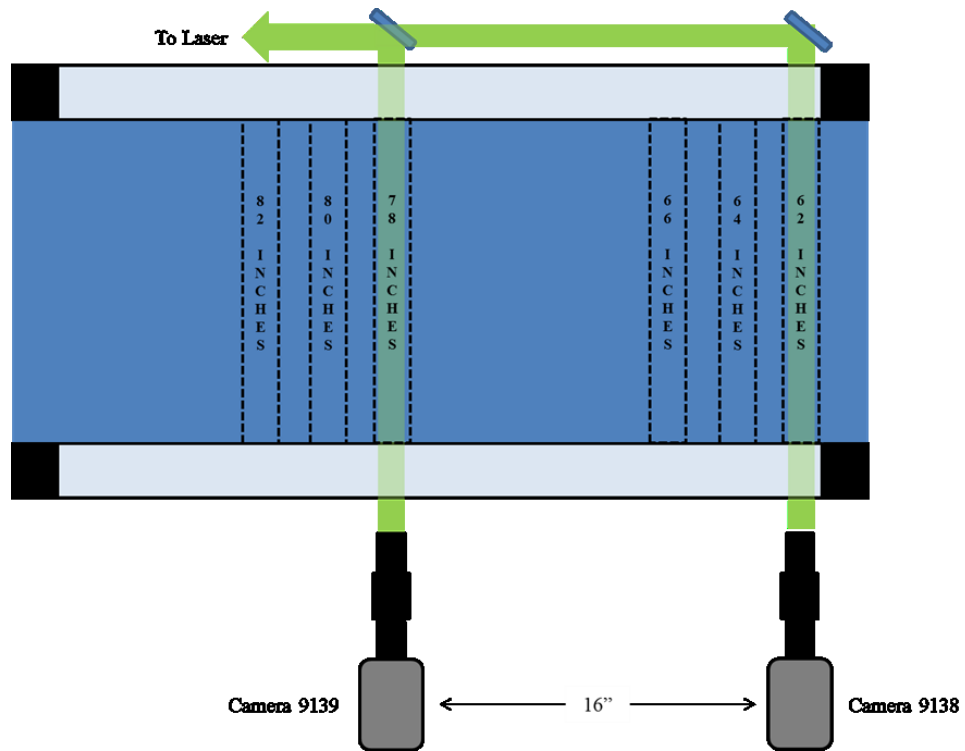


Figure 2.5: Top-Down view of measurement window and positioning of Cameras 9138 and 9139. Note that each camera is moved in tandem to the next position such that the 16 in separation is maintained regardless of run.

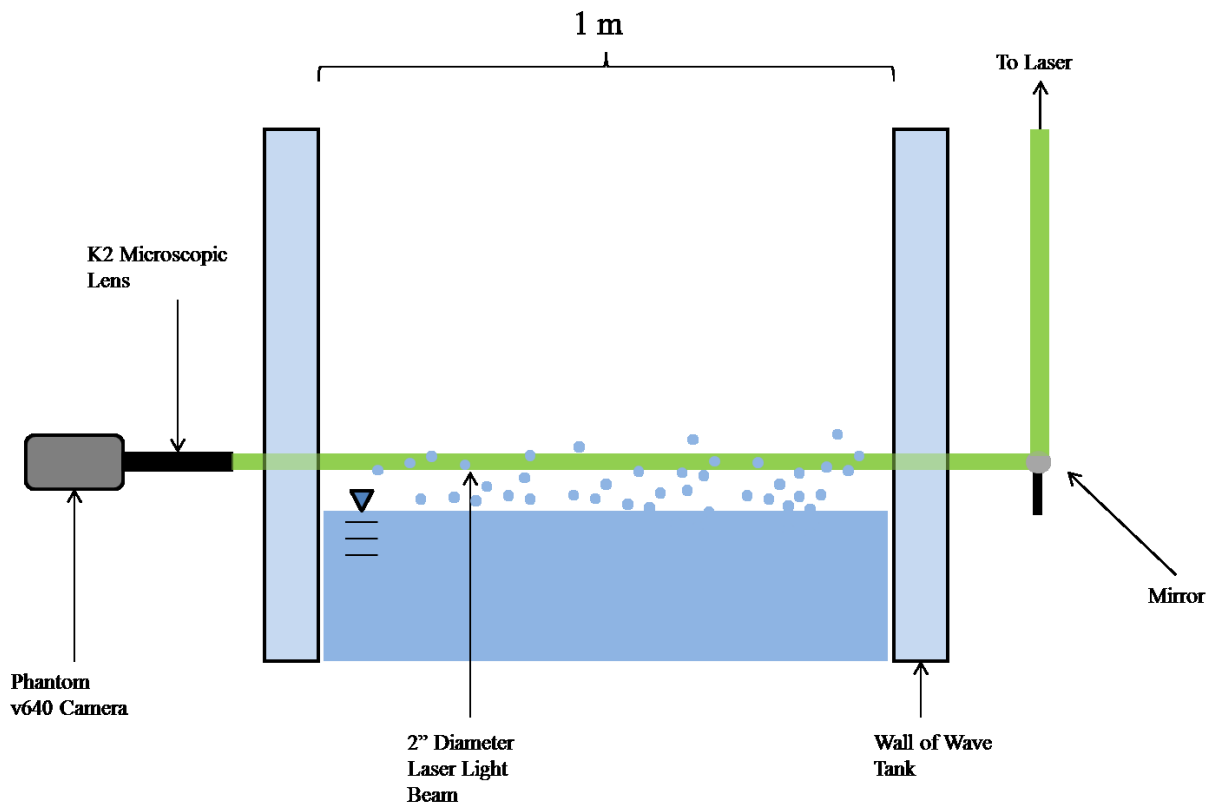


Figure 2.6: Schematic of the set-up for droplet measurement.

## Chapter 3: The Diameter-Dependent Out-of-Focus and Depth-of-Field Corrections

### 3.1 The Diameter Dependent Out-of-Focus Correction

Images of droplets that are located in the focal plane of the camera lens will appear well focused with sharp edges and black intensity in the camera image. Droplets that are measured either closer to or farther from the focal plane will appear out of focus resulting in dilated diameters and increased image intensity (grey instead of black). Additionally, the images of droplets that are not in the focal plane are subject to light diffraction. Both of these effects increase with increasing distance from the focal plane and with decreasing droplet diameter. As such, a calibration method to determine both an effective depth of field for the measurement volume for each droplet and the accuracy of the droplet diameter measurements was developed.

In this calibration method, a glass reticle with black circles of known diameters was photographed at various distances from the focal planes of the K2 lenses. Both focal planes were located at the midpoint of the tank width. The dot on the reticle varied in diameter from 3000  $\mu\text{m}$  at the largest to 30  $\mu\text{m}$  at the smallest, arranged in two horizontal rows across its surface. An image of this reticle located at the focal plane of the K2 lens is displayed below in Figure 3.1.

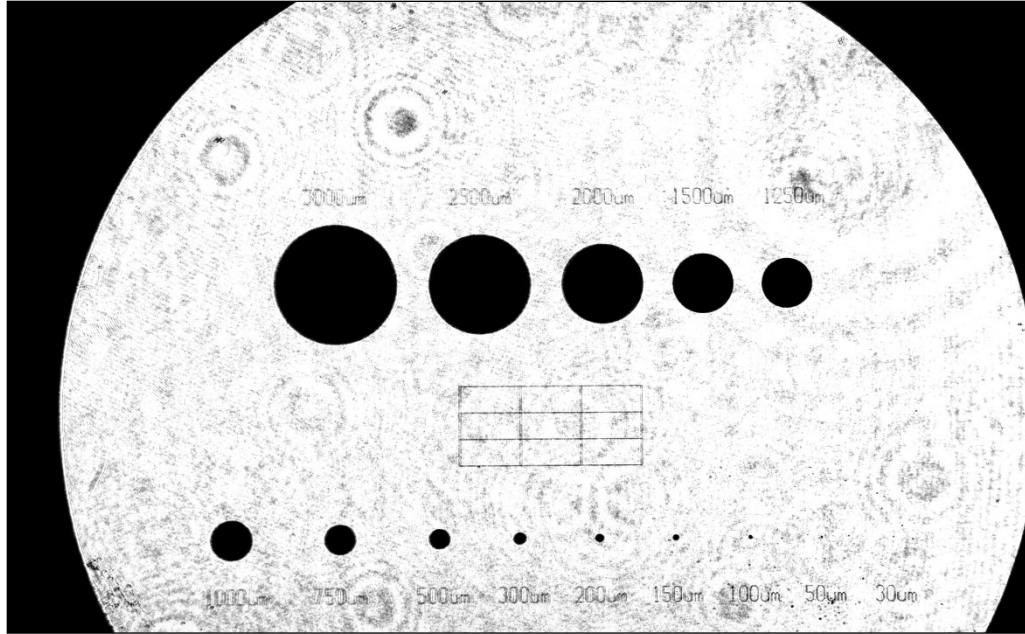


**Figure 3.1: Image of the glass reticle used to generate out-of-focus and depth of field corrections.**

The reticle was positioned within the measurement volume and was moved across the width of the wave tank using a NEAT 310M motorized traverser as can be seen in the schematic diagram shown in Figure 3.2. Images were taken with the reticle placed at the focal plane and positions toward and away from the focal plane in 0.1 mm steps up to a distance of  $\pm 4$  mm from the focal plane and in 40mm steps outside the  $\pm 4$  mm range. The smallest dot becomes too faint for its diameter to be determined accurately within the  $\pm 4$  mm range, whereas the largest dot's diameter can be determined accurately even when positioned at the near and far walls of the tank.

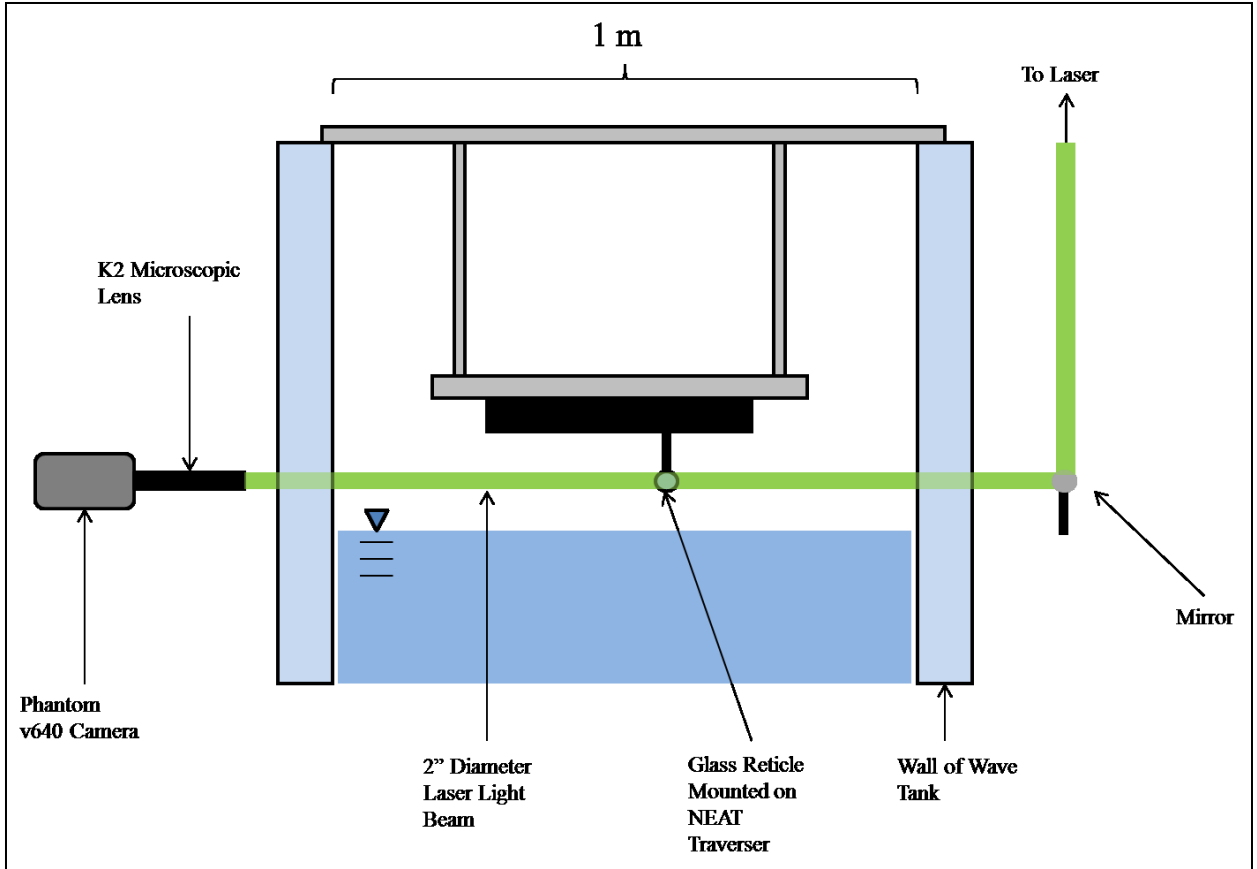
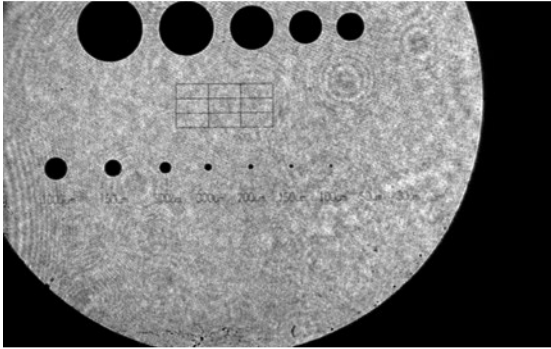


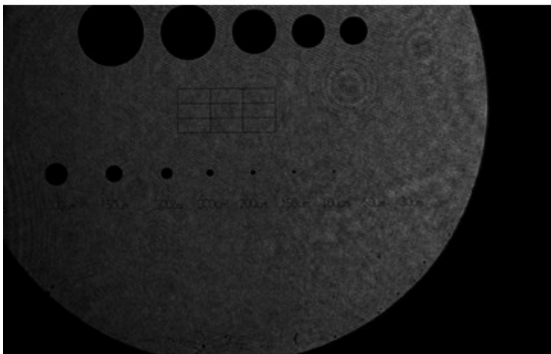
**Figure 3.2: Wave tank configured for traversing of reticle for the generation of out-of-focus and depth-of-field corrections.**

As mentioned previously, the laser light being delivered to the two cameras is separated into two distinct pulses for the purpose of calculating the velocities of the droplets. The laser, however, delivered these pulses with unequal energies resulting in the first pulse being brighter than the second. Thus, each camera will alternate between recording one bright and one darker image per pulse pair. Additionally, the beam splitter that separates the laser light traveling to Camera 9138 and Camera 9139 does not divide the energy evenly. Altogether, each twin pulse from the laser results in four images of differing intensities: a bright and a dark image on Camera 9138, and a bright and dark image on Camera 9139. These differences in intensities can be observed in Figure 3.3.

### Camera 9138

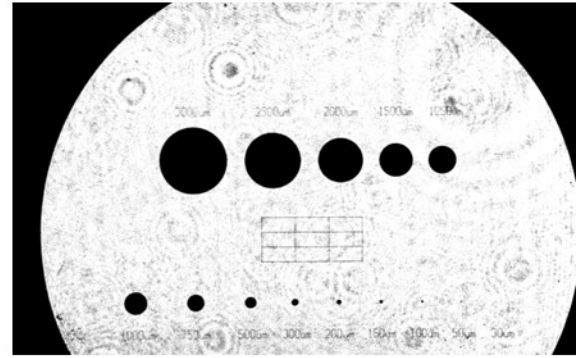


**Bright Pulse**

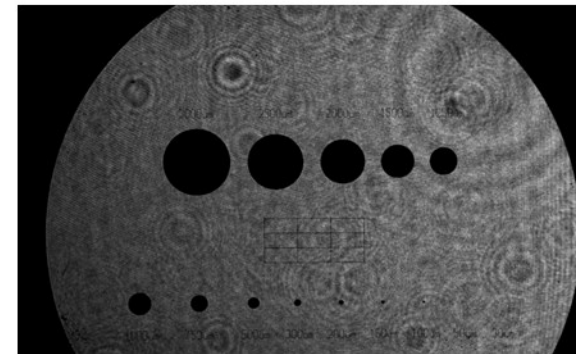


**Dark Pulse**

### Camera 9139



**Bright Pulse**



**Dark Pulse**

**Figure 3.3: Difference in laser light intensity due to uneven distribution of pulse energy and optical beam splitter.**

Since the light intensity affects the degree to which the diameters of droplets are dilated when they are out of focus, it was necessary to perform the calibration procedure on both cameras. However, since the diameters were only calculated from the brighter of the two pulses in each camera, only two separate image sets were generated. The darker images were only used for velocity calculations.

After the calibration images for both cameras were collected, the diameters and intensities of each dot image were calculated using a MATLAB script. This script inverted the original image intensity and then used an edge detection algorithm to

identify the dots. Then, using a least squares regression of an inverse hyperbolic tangent function, a fit of the dot was generated. Figures 3.4 and 3.5 show an intermediate step in this MATLAB script where the dot image intensity is plotted and the least squares regression.

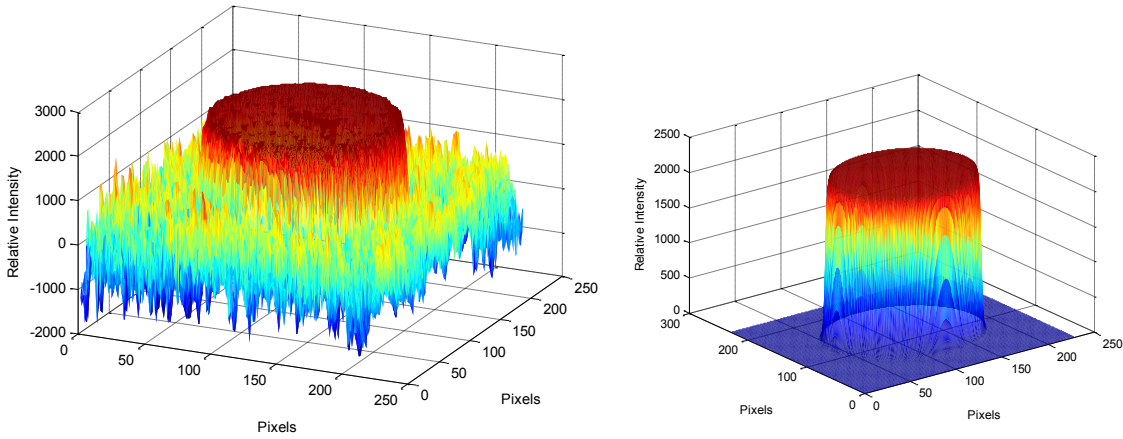


**Figure 3.4: Contours of relative intensity as a function of position for an image of a 1500  $\mu\text{m}$  dot near the focal plane. Plot at left shows intensity from original image showing noise surrounding dot due to speckle and dust. Plot at right shows the fit of the dot after applying a least-squares regression of a hyperbolic tangent function.**

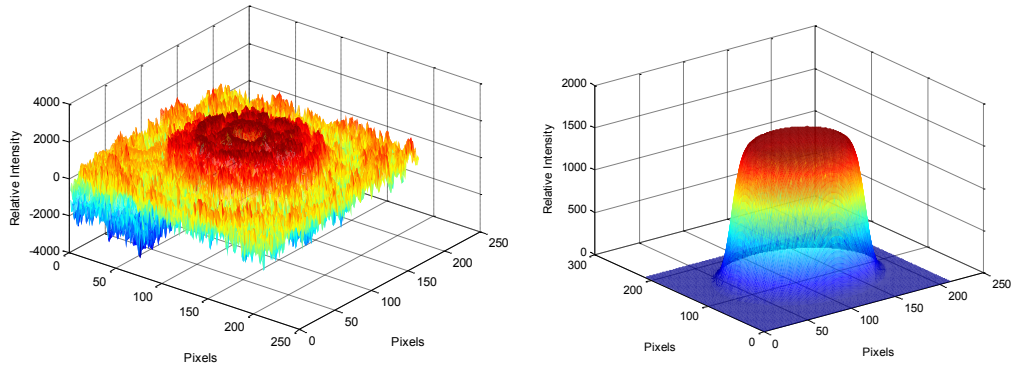


**Figure 3.5: Contours of relative intensity as a function of position for an image of a 1250  $\mu\text{m}$  dot 210 mm away from the focal plane. Note the characteristic rings of the interference pattern in the intensity plot at the left. The fit is plotted on the right. Note that the slope of the hyperbolic tangent function is more gradual due to the image being less distinct.**

This MATLAB script was applied to the calibration images and the measured radius and measured intensity data of the dots at various positions was compiled. The

results of the calibration for the dots with diameters ranging from 1,250 to 3,000  $\mu\text{m}$  are plotted below in Figures 3.6 through 3.9.

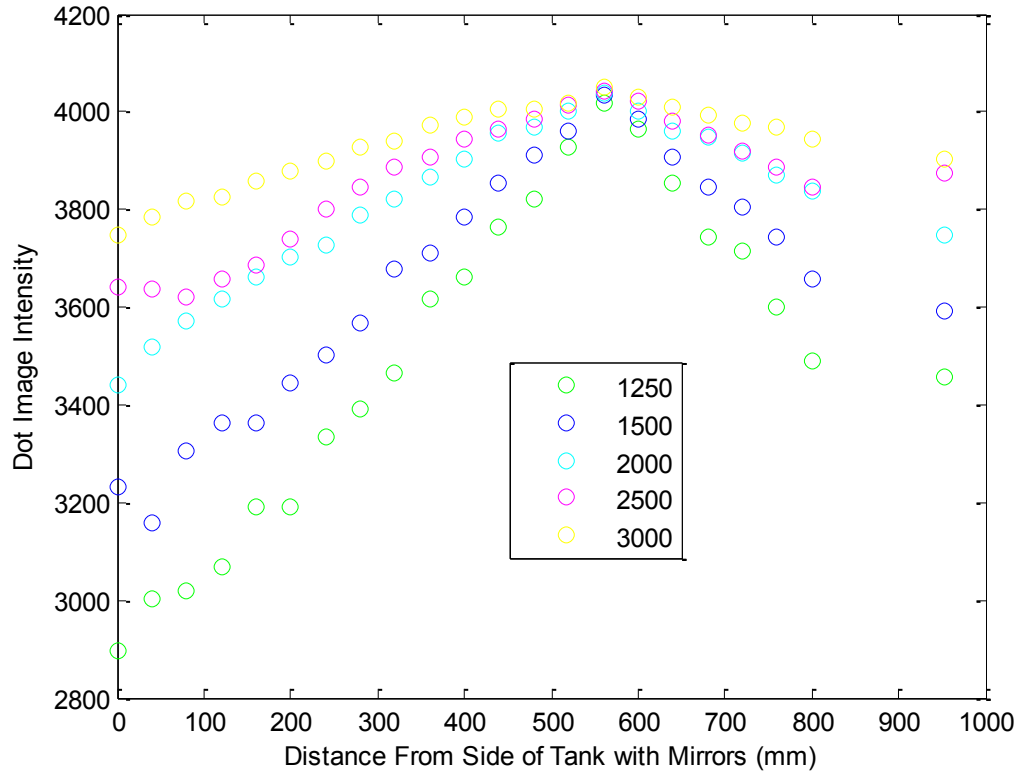


**Figure 3.6: Camera 9138—Average intensity of the images of the dots versus position across the tank width for the top row of dots on the reticle (see Figure 3.3). The focal plane of the camera is at a distance of 560 mm and 0 mm is the location of the tank wall on the opposite side of the tank from the camera.**



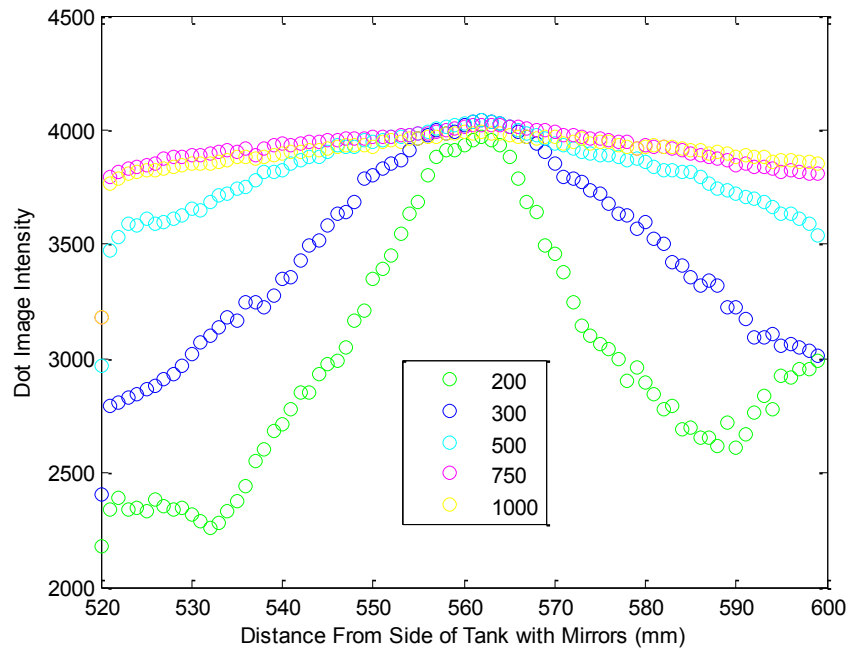


**Figure 3.7: Camera 9138—Average intensity of the images of the dots versus position across the tank width for the dots ranging in diameter from 200 to 1000  $\mu\text{m}$ . The focal plane of the camera is at a distance of 560 mm. Measurements taken at 1 mm intervals  $\pm 40$  mm from the focal plane.**

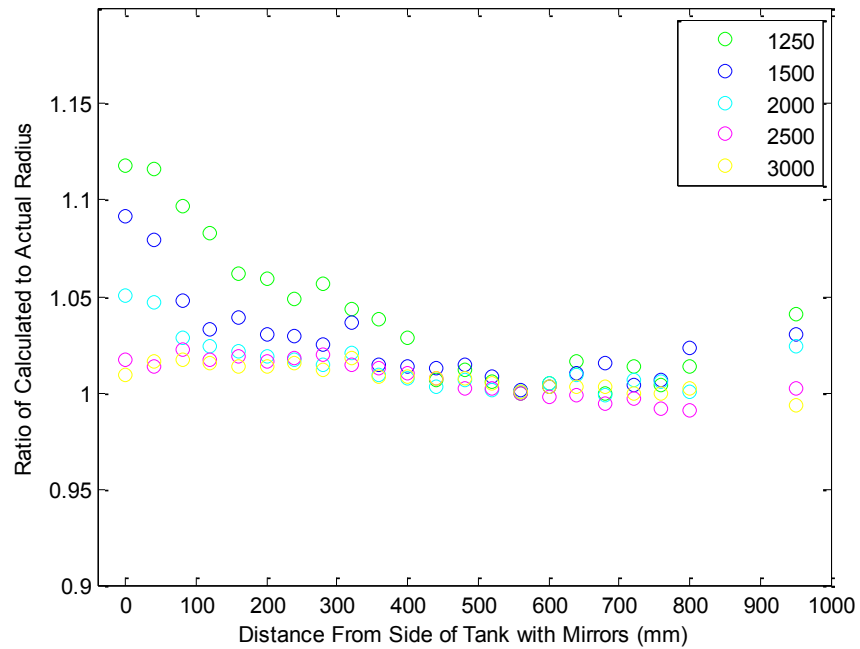


**Figure 3.8: Camera 9138—Ratio of measured dot diameter to actual dot diameter versus position across the tank width for dots ranging in diameter from 1250 to 3000  $\mu\text{m}$ . The focal plane of the camera is at a distance of 560 mm and 0 mm is the location of the tank wall on the opposite side of the tank from the camera.**

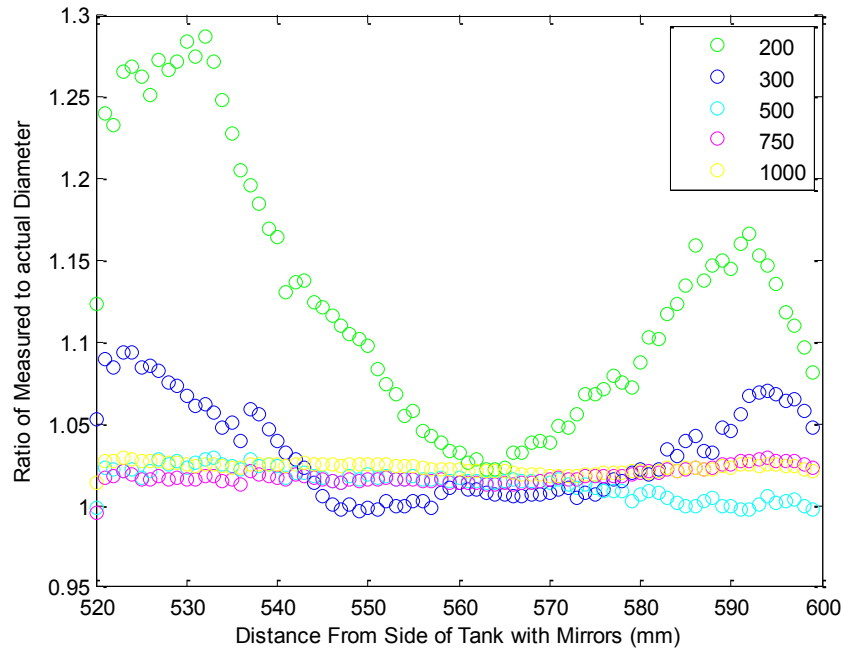


**Figure 3.9: Camera 9138—Ratio of measured dot diameter to actual dot diameter versus position across the tank width for dots ranging in size from 200 to 1000  $\mu\text{m}$ . The focal plane of the camera is at a distance of 560 mm and the reticle has been traversed in 1mm steps  $\pm 40$  mm from the focal plane.**

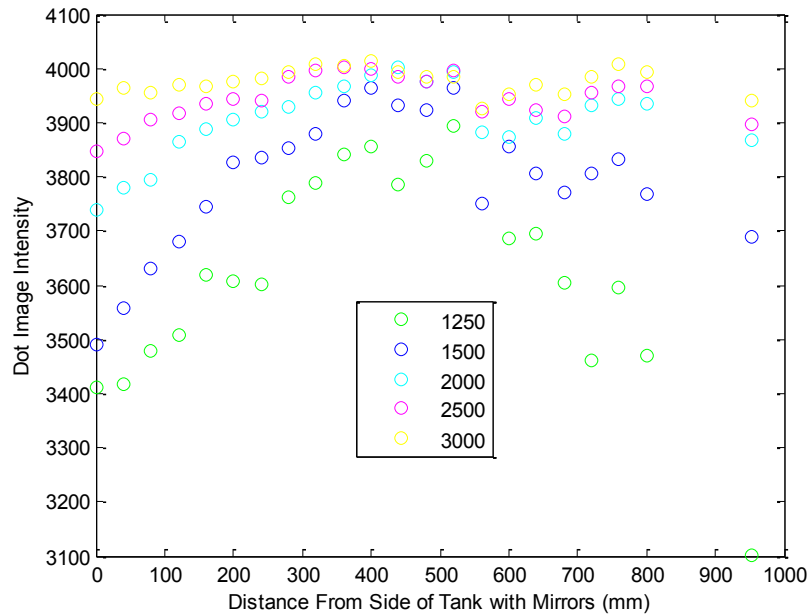


**Figure 3.10: Camera 9139— Average intensity of the images of the dots versus position across the tank width for the top row of dots on the reticle (see Figure 3.3). The focal plane of the camera is at a distance of 560 mm and 0 mm is the location of the tank wall on the opposite side of the tank from the camera.**

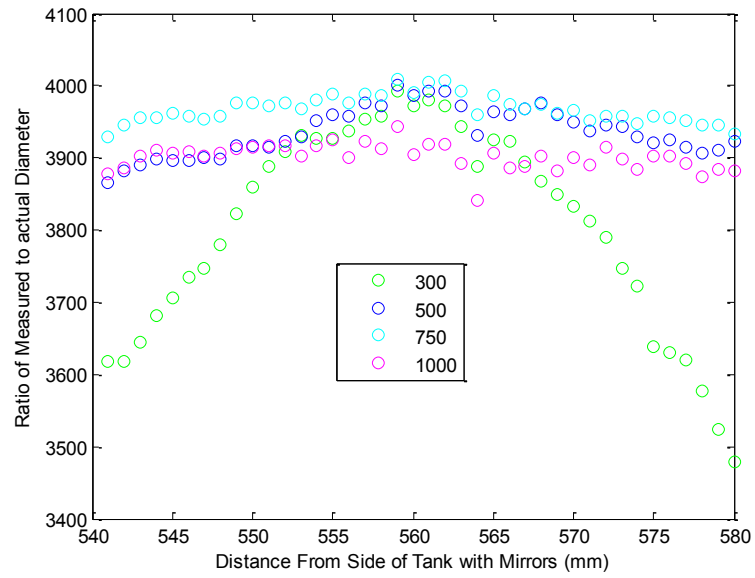


**Figure 3.11: Camera 9139—Average intensity of the images of the dots versus position across the tank width for the dots ranging in diameter from 300 to 1000  $\mu\text{m}$ . The focal plane of the camera is at a distance of 560 mm. Measurements were taken at 1mm intervals  $\pm 20$  mm from the focal plane.**

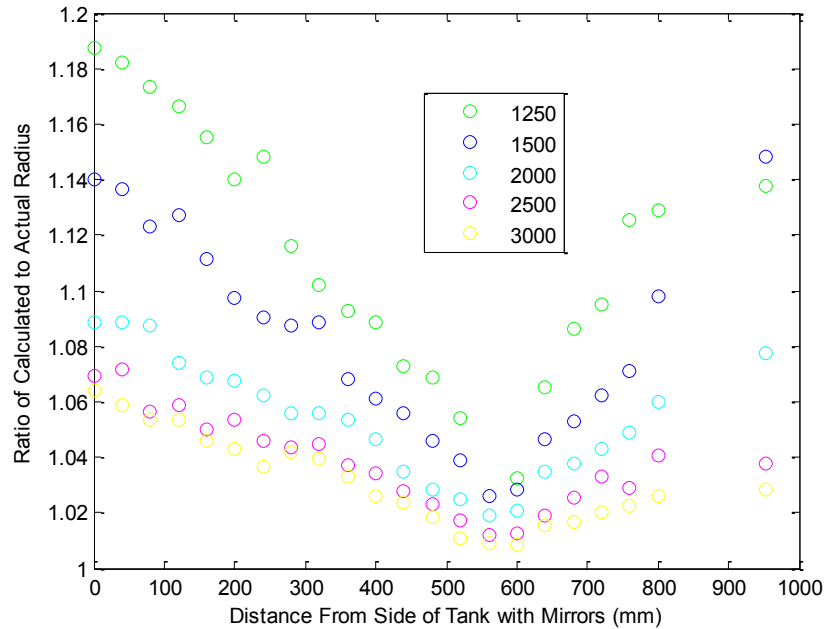


**Figure 3.12: Ratio of measured dot diameter to actual dot diameter versus position across the tank width for the top row of dots on the reticle (see Figure 3.3). The focal plane of the camera is at a distance of 560 mm and 0 mm is the location of the tank wall on the opposite side of the tank from the camera.**

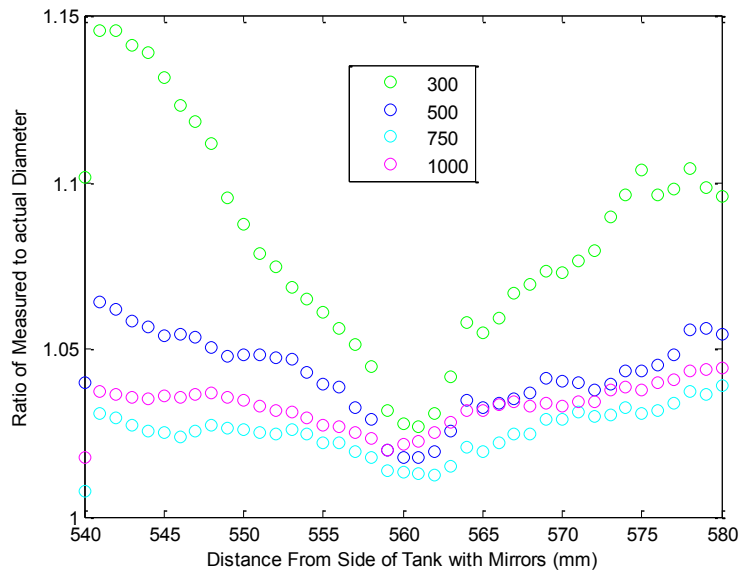


**Figure 3.13: Camera 9139—Ratio of measured dot diameter to actual dot diameter versus position across the tank width for dots ranging in size from 300 to 1000  $\mu\text{m}$ . The focal plane of the camera is at a distance of 560 mm and the reticle has been traversed in 1mm steps  $\pm$  20 mm from the focal plane.**

From this set of figures it is apparent that the droplets appear to increase in size as they are moved away from the focal plane. The largest dot, at 3,000  $\mu\text{m}$  is affected the least and generally experiences less than 10% change in its calculated diameter at the sides of the wave tank. The dot with a diameter of 1,250  $\mu\text{m}$ , however, appeared to increase in diameter by nearly 20% at the tank edge.

Whereas the calculated diameter of the dots increases as the distance from the focal plane increases, the inverted intensity ( $4095 - I$ , where  $I$  is the average intensity measured from the image) decreases with the increasing distance from the focal plane (see Figure 3.6 and 3.8). In the plot, higher values correspond to darker and more distinct dots. As the intensity decreases, the dot becomes fainter and the edge around it less sharp. In dots with intensities much lower than 3,000, diffraction patterns can be observed, thereby further complicating the calculation of its diameter.

The lower row of dots (ranging in diameter from 1,000  $\mu\text{m}$  to 50  $\mu\text{m}$ ) was assessed over a range less than the full width of the tank. These dots experience the same trends as the top row yet over a markedly smaller displacement of the reticle. At 30 mm from the focal plane, dots less than 100  $\mu\text{m}$  become invisible. The images of these dots can also experience over 150% dilation of their apparent radii. In Figure 3.10, an image of the reticle taken at 560 mm from the focal plane is shown to demonstrate the effects of diameter dilation and inverted intensity drop. Note that the out-of-focus and diffraction effect increase with decreasing dot diameter. Many of the dots in the bottom row are nearly invisible, and the ones that can be distinguished are too faint for any useful data to be extracted. The increase in dot diameter with distance is also apparent—the calculated diameter in red always is larger than that of the actual dot radius shown in green.

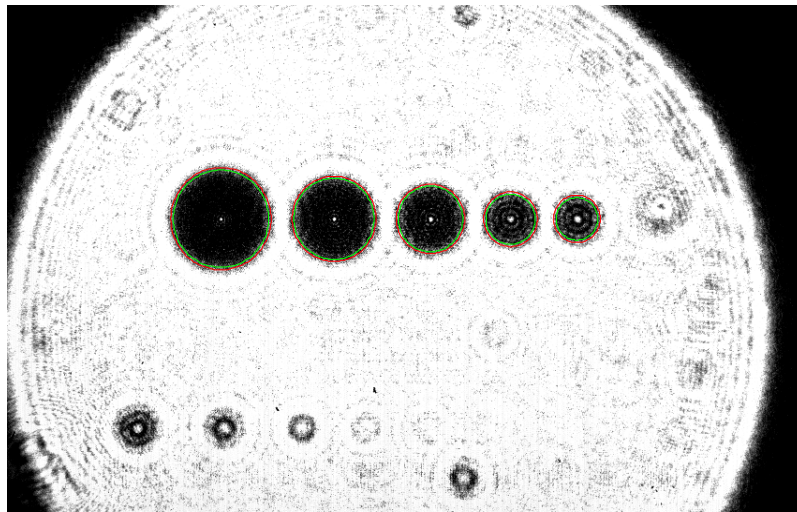


**Figure 3.14:** Image of the reticle taken from 560 mm away from the focal plane. The calculated diameter is shown in red while the actual diameter is shown in green.

It can be seen in Figures 3.6 through 3.9 that the intensity and diameter dilation calculations were noisy. This is because the border around each dot is not definitive and

the presence of dust on the lens or on the walls of the tank caused the calculated diameter to change even with successive images taken with the reticle in the same position. The speckle pattern from the laser light itself further contributed to the error in these calculations.

The actual radius, measured (from the image) radius and measured intensity for these dots at the varying positions of the reticle were consolidated into one three-dimensional plot per camera and are shown in Figures 3.11 and 3.12. In these plots, the dot radius is measured in pixels.

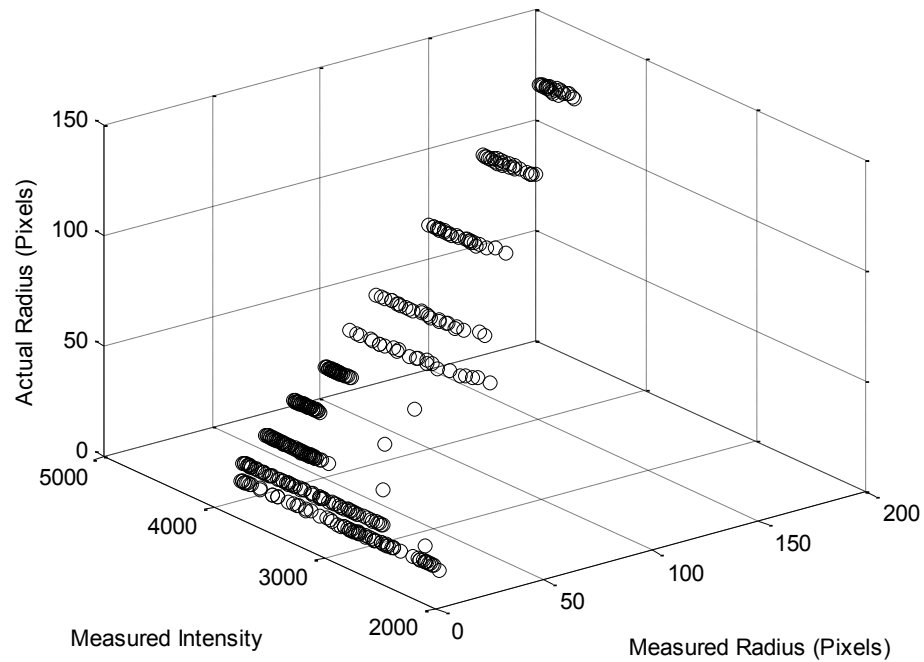


**Figure 3.15: Actual dot radius as a function of measured dot intensity and measured radius for Camera 9138.**

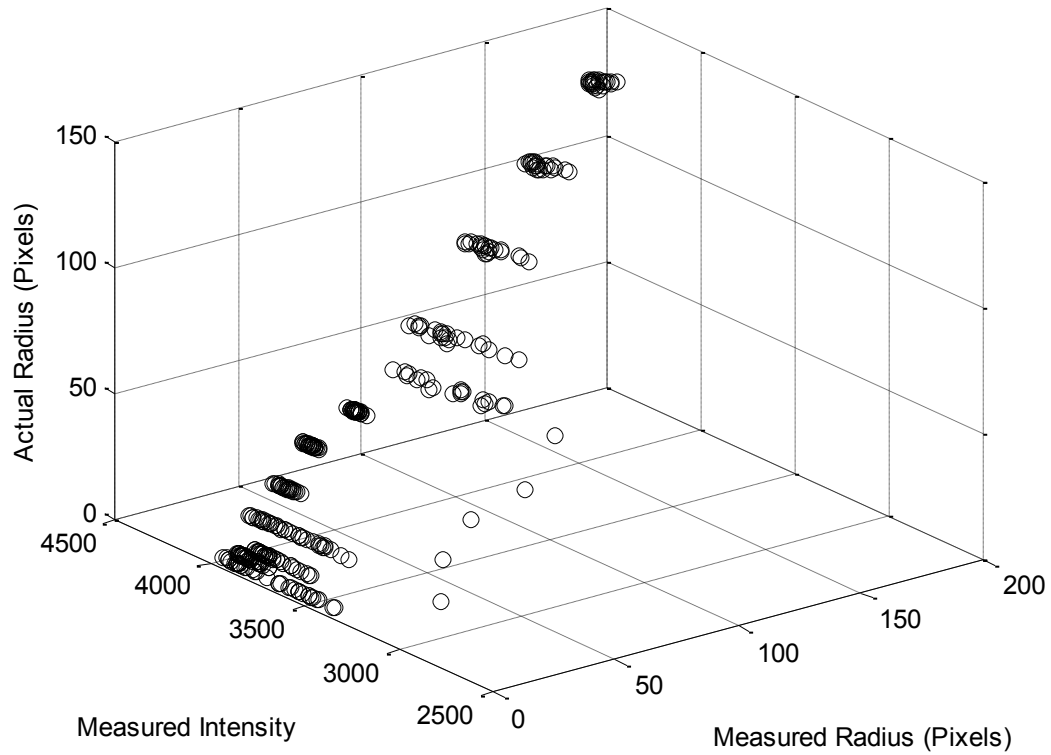


**Figure 3.16: Actual dot radius as a function of measured dot intensity and measured radius for Camera 9139.**

From these plots it is apparent that there is a functional relationship between the actual radius of the dot and the measured radius and intensity of the image of the dot:

$$\text{Actual Radius} = f(\text{Measured Intensity}, \text{Measured Radius})$$

The function selected to model the data in Figures 3.11 and 3.12 was of the first order in the measured radius and second order in the measured intensity. The justification for using this function is that the dots on the reticle constitute circles of confusion. The expansion of the circle of confusion is a linear function of the distance of

the object from the focal plane. The intensity, however, decreases as the square of the distance from the focal plane.

Using a least-squares fit of this function to the experimental data in Figures 3.11 and 3.12, the following functions for the out-of-focus correction were obtained:

$$9138: \quad R_a = -27.21 + 0.7372R_m + 0.0147I + 6.19 * 10^{-5}R_mI - 1.97 * 10^{-6}I^2$$

$$9139: \quad R_a = 6.395 + 0.1495R_m - 0.00334I + 2.04 * 10^{-4}R_mI - 4.319 * 10^{-7}I^2$$

where  $R_a$ ,  $R_m$ , and  $I$  are the actual radius in  $\mu\text{m}$ , measured radius in  $\mu\text{m}$  and measured intensity, respectively. The surfaces associated with these functions are plotted along with their respective data sets in Figure 3.13 and 3.14. The  $R^2$  value for these fits are 0.9999 for camera 9138 and 0.9995 for camera 9139. These fits intuitively make sense as the actual radius will always be less than the measured radius and higher intensity levels indicate a sharper image meaning that the calculated and actual radius are relatively close. In the breaking wave experiments, the droplet image diameters and intensities were entered into these functions to obtain an improved estimate of the actual droplet diameters.



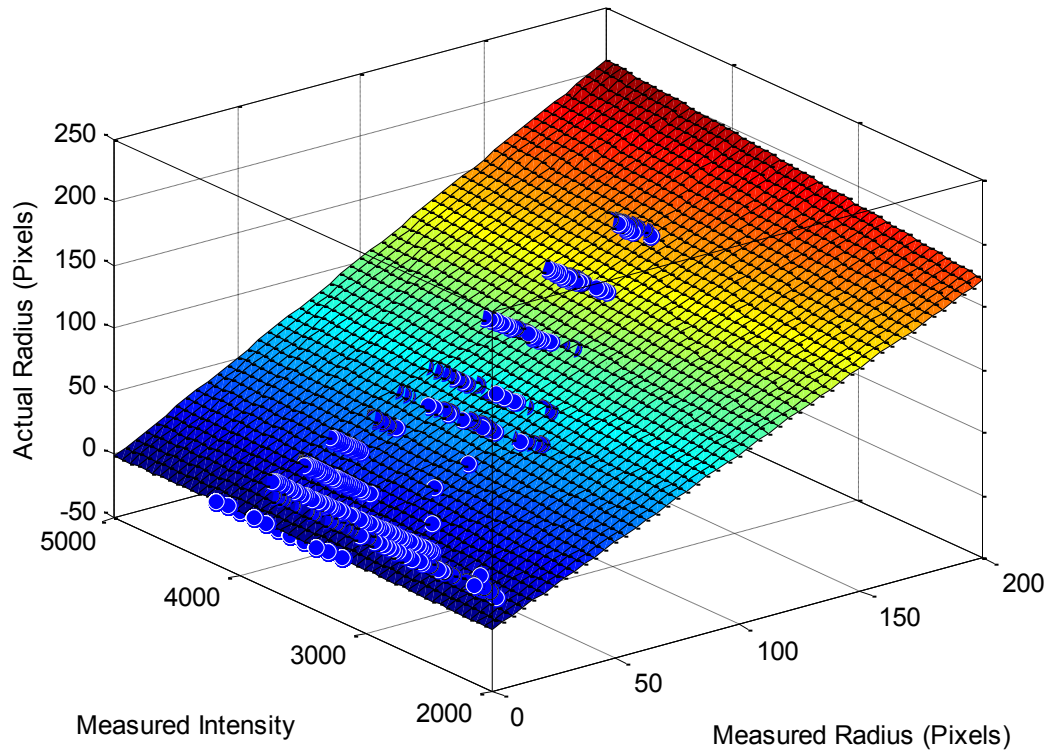


**Figure 3.17: Out-of-focus function fitted over the data from the reticle calibration for Camera 9138.**

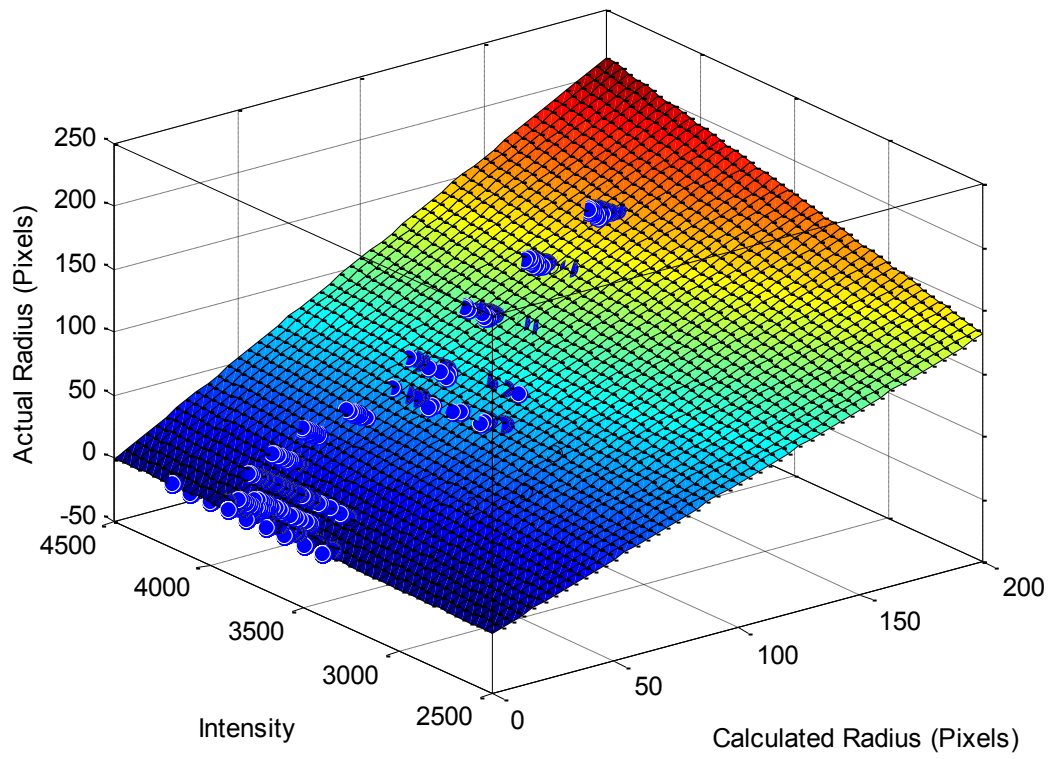


**Figure 3.18: Out-of-focus function fitted over the data from the reticle calibration for Camera 9139.**

### 3.2 The Diameter-Dependent Depth-of-Field Correction

It was shown previously that as the droplet position moves away from the focal plane, the diameters and intensities of the images of the smaller droplets change more rapidly than those of the larger droplets. One consequence of this phenomenon is that the effective distance from the focal plane (depth-of-field) over which droplets can be measured with a given accuracy is a function of a droplet's diameter. For example, a droplet with a diameter of 1250  $\mu\text{m}$  has a depth of field of 400 mm whereas a droplet with a diameter of 2000  $\mu\text{m}$  has a depth of field of 950 mm. This effect is displayed in Figure 3.15.

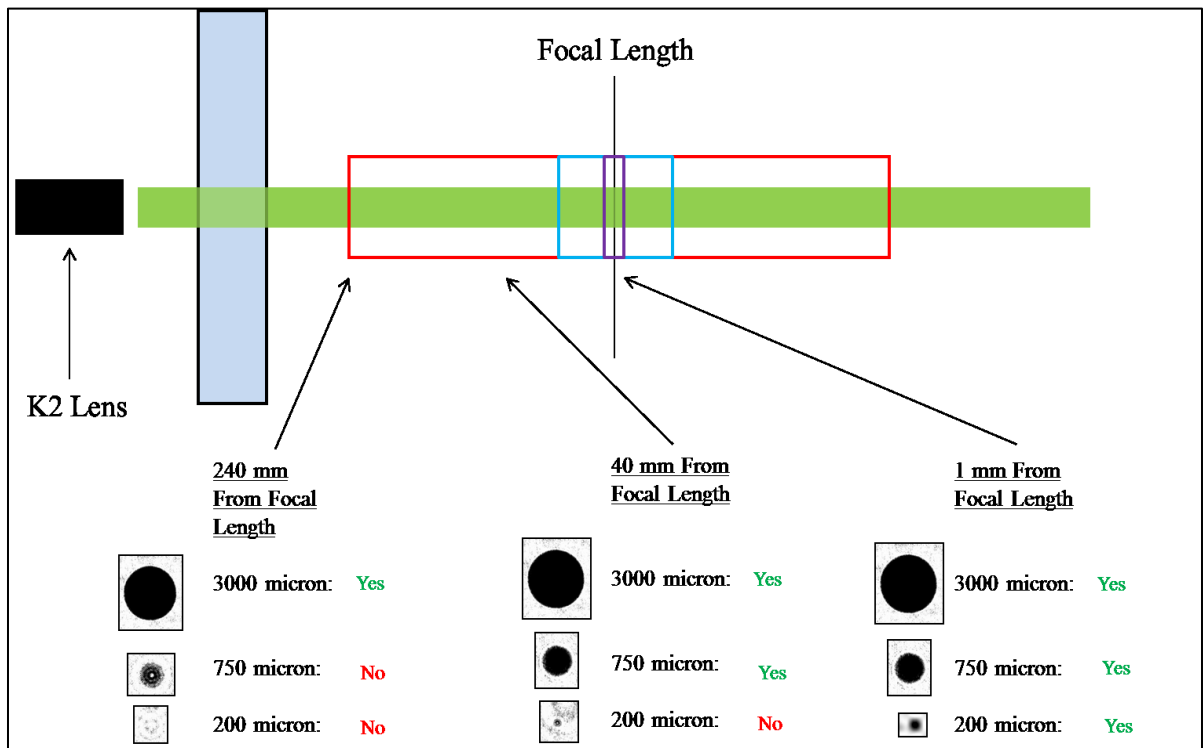


Figure 3.19: The differing effects of increasing distance from the focal plane as a function of droplet diameter.

Thus, to normalize number of droplets of a given diameter measured in the images to correspond to the same depth of field as the largest droplets, i.e. the 1.2 meter

width of the wave tank, a correction factor  $n$  must be applied to the number of droplets of each diameter. To estimate the number of droplets expected ( $N_c$ ) within this 1.2 m long experimental volume, the correction factor,  $n_i(d_i)$  was multiplied by the number of droplets for a given diameter,  $N(d_i)$ . Thus:

$$N_c(d_i) = N(d_i)n_i(d_i)$$

The correction factor  $n_i$  for a droplet of diameter  $d_i$  was determined from the maximum depth-of-field over which a droplet of that size could be measured and is computed as follows:

$$n_i = \frac{V}{V^*(d_i)} = \frac{L * A_c}{L^*(d_i) * A_c}$$

Where  $V^*$  denotes the volume over which a droplet of a given diameter  $d_i$  can be accurately processed,  $A_c$  denotes the cross-sectional area of the depth-of-field which is determined by the size of the camera sensor and  $L$  denotes the width of the tank. Since the cross-sectional area of the depth-of-field does not change over the width of the tank because the laser light is parallel, this equation simplifies to the ratio of the width of the tank to the width over which a droplet can be processed. Furthermore, this width,  $L^*$ , is a function of the droplet's actual diameter and the intensity cutoff that is used to ensure that the error in droplet diameter does not exceed  $\pm 5\%$ . From the data, this intensity was chosen as 3500. Therefore, the expression for the correction factor can be also written as follows:

$$n_i = \frac{L}{f(d_i, I_{cut})} = \frac{1200mm}{f(d_i, 3500)}$$

where  $L$  denotes the width of the tank and  $f$  denotes the function that governs the depth-of-field for a droplet of diameter  $d_i$  and an intensity cutoff of  $I_{cut}$ . The expression for the length over which the droplets of a given diameter can be processed was derived in a similar manner to the function governing the out-of-focus correction. Distance from the focal point was used as the dependent variable with actual dot radius and intensity as the independent variables. Figures 3.16 and 3.17 show these three dimensional plots for Cameras 9138 and 9139, respectively.

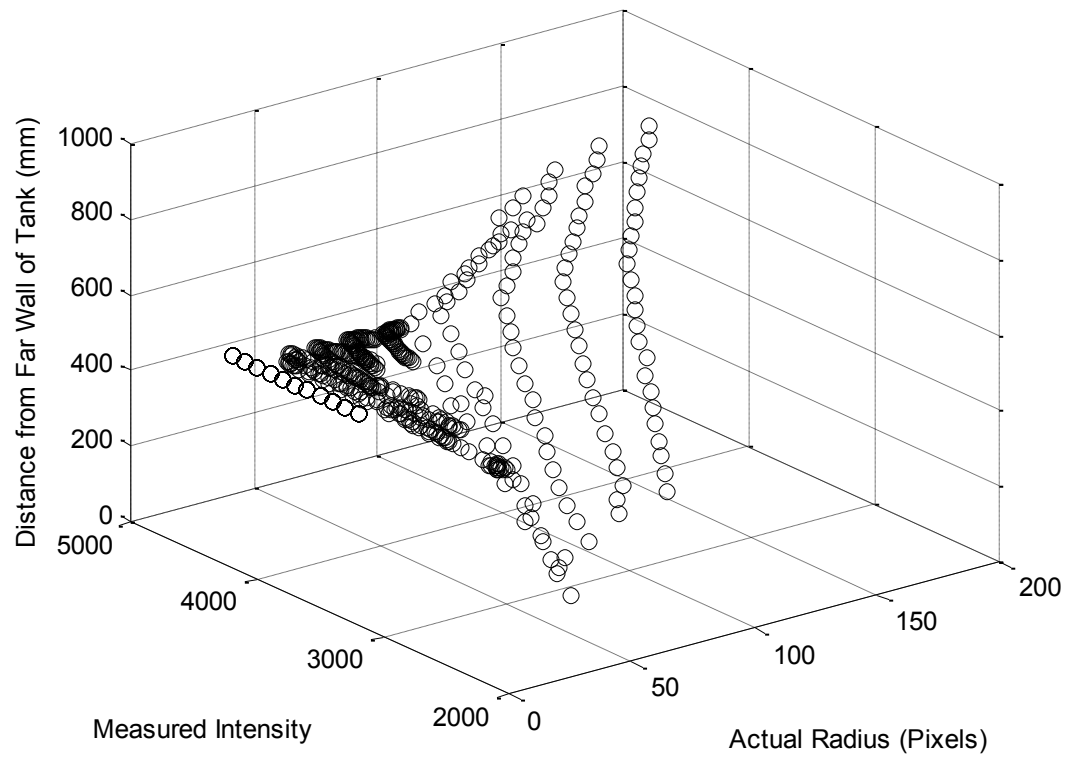


**Figure 3.20: Camera 9138—Plot of distance from the far wall of the wave tank as a function of measured dot radius and measured dot intensity.**

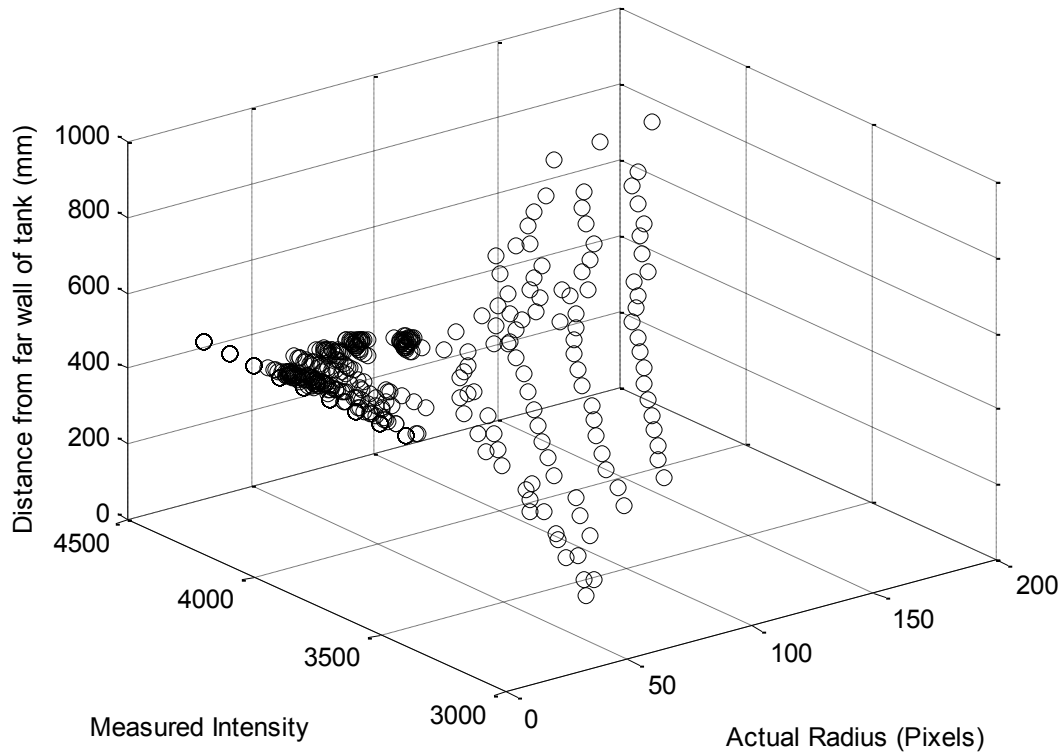


**Figure 3.21: Camera 9139—Plot of distance from the far wall of the wave tank as a function of measured dot radius and measured intensity.**

Like the fits for the out-of-focus corrections, the depth-of-field correlations were treated as third order in radius and third order in intensity. This choice in fit order was not dictated by any physical mechanism—these selections merely fit the data most closely. Using the same order as the out-of-focus corrections would have resulted in Camera 9139 have an unacceptable amount of error in its correction factors. More noise was observed in this Camera’s calibration so the goodness-of-fit for this data set was naturally worse than the other camera. These two functions were applied only over half of each respective data set: the function is fitted for calibration data extracted from images closer to the camera than the focal plane.

9138:

$$L^* = -478.1 - 14.72R + 0.1878I - 0.2692R^2 - 0.005771RI - 8.21 * 10^{-5}I^2 + 4.01 * 10^{-5}R^3 + 6.364 * 10^{-5}R^2I - 4.859 * 10^{-7}RI^2 + 1.003 * 10^{-8}I^3$$

9139:

$$L^* = -1246 + 20.19R + 1.457I - 0.5243R^2 - 0.01269RI - 3.907 * 10^{-4}I^2 - 5.283 * 10^{-5}R^3 + 1.251 * 10^{-4}R^2I + 1.978 * 10^{-6}RI^2 + 3.479 * 10^{-8}I^3$$

The  $R^2$  value for the 9138 and 9139 fits are 0.9798 and 0.8799, respectively.

Figures 3.18 and 3.19 show these functions fit over half of the data.



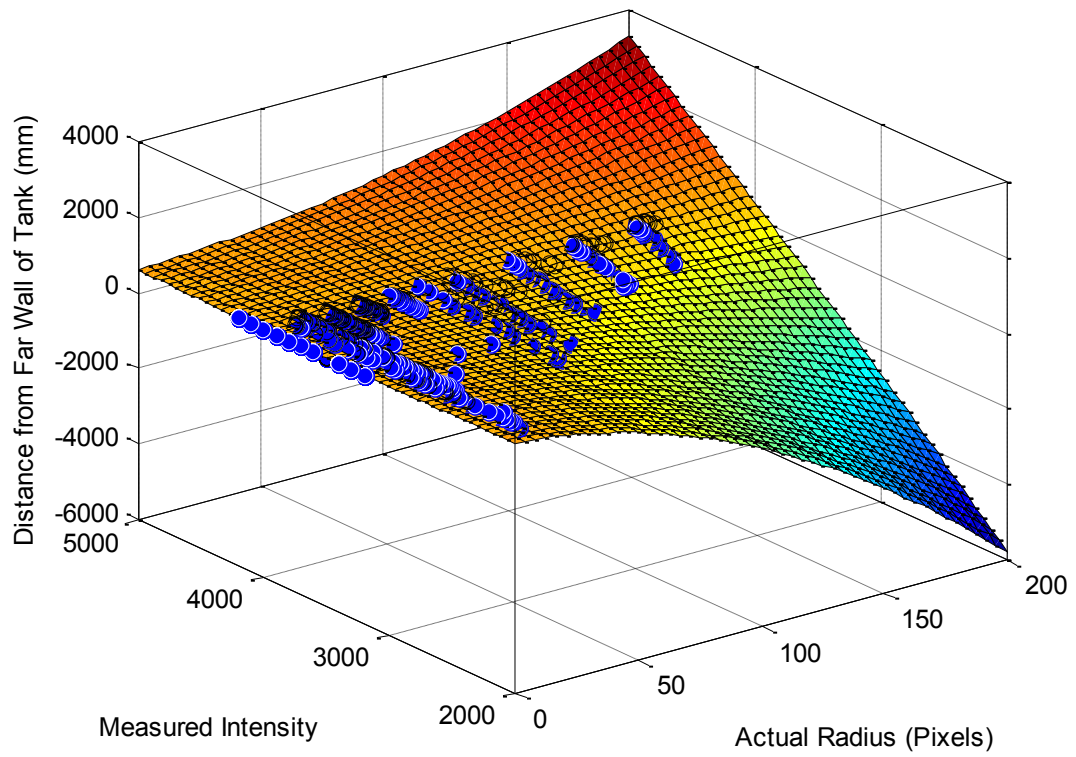


**Figure 3.22: Camera 9138—Distance from the far wall of the wave tank as a function of actual radius and measured intensity and the fit function corresponding to data collected on the near side of the focal plane.**

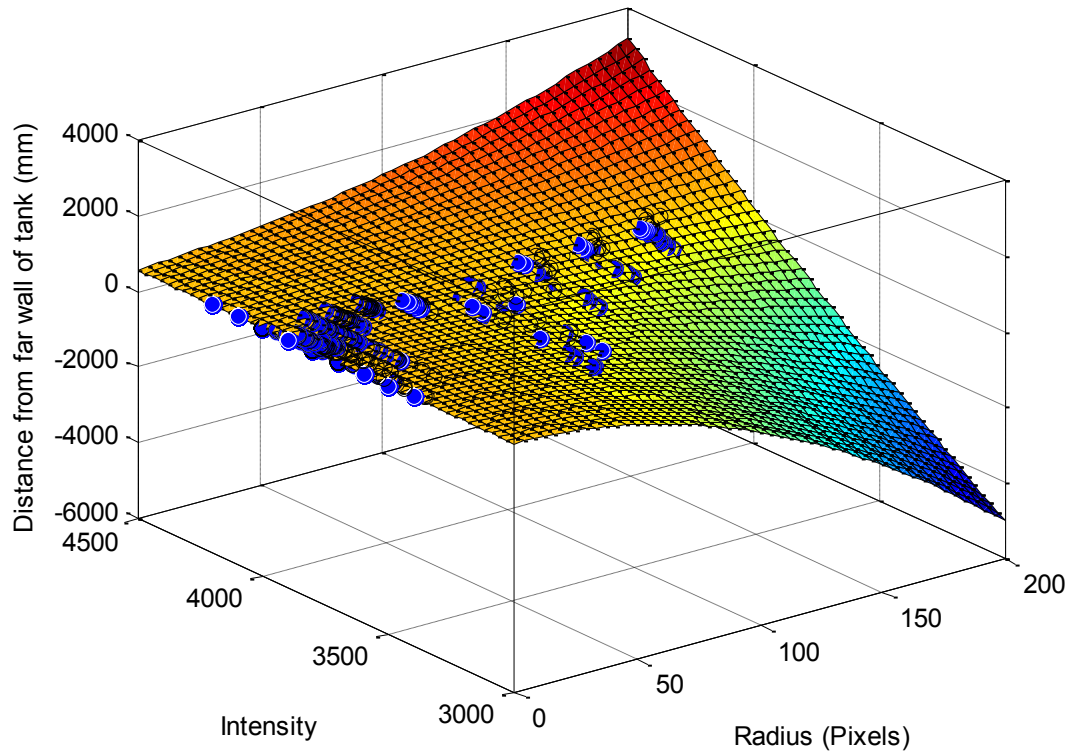


**Figure 3.23: Camera 9139— Distance from the far wall of the wave tank as a function of actual radius and measured intensity and the fit function corresponding to data collected on the near side of the focal plane.**

These functions, however, carry Intensity as a variable. In order for the correction factor to be applied, the cutoff intensity was substituted into these functions. Again, the experimental volume through which a droplet can be processed is not dictated by an individual droplet's intensity, but rather the diameter associated with the cutoff intensity of 3500 for that particular droplet. Substituting  $I = 3500$  into these functions yields the following:

$$9138: \quad L^* = 554.6 - 0.4973R - 0.006535R^2 - 1.831 * 10^{-5}R^3$$

$$9139: \quad L^* = 557.3 - 1.211R - 0.005900R^2 - 6.365 * 10^{-5}R^3$$

These functions intercept with the focal length of their respective lenses. In order to obtain the length over which a droplet of a specific diameter can be observed, this function must be subtracted from the focal length and then multiplied by two since each function is fitted over only half of the data. The correction factor  $n_i$  for a droplet of radius  $R_i$  expressed in pixels was then computed for each camera individually using these expressions:

9138:

$$n_i = \frac{1200}{0.9946R_i + 0.01307R_i^2 + 3.662 * 10^{-5}R_i^3}$$

9139:

$$n_i = \frac{1200}{2.422R_i + 0.0118R_i^2 + 1.273 * 10^{-4}R_i^3}$$

These correction factors were used later in the droplet diameter distribution graphs in figures displayed in the following chapter. This ensured that all droplets were being assessed over the same depth-of-field. As would be expected, the frequency of smaller droplets increased significantly when the corrected depth-of-field was considered. Very large droplets (> 2500  $\mu\text{m}$ ) made negligible contributions to these distributions after correction because they can be observed over depths-of-field greater than the width of the tank and therefore their correction factors were often less than one. The plots for the

correction factor as a function of droplet radius are shown for Cameras 9138 and 9139 in Figures 3.24 and 3.25, respectively.

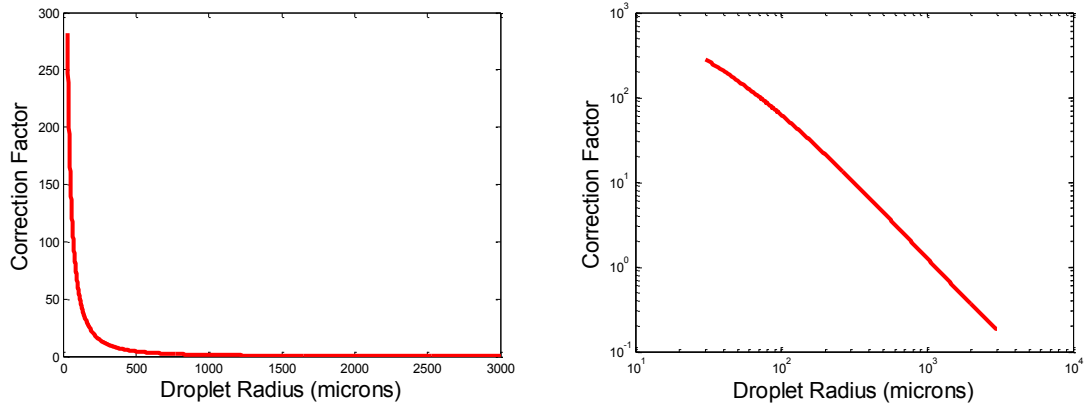


**Figure 3.24:** Plot of correction factor  $n_i$  as a function of droplet radius for camera 9138 (left). Same function plotted on log-log axes at right.

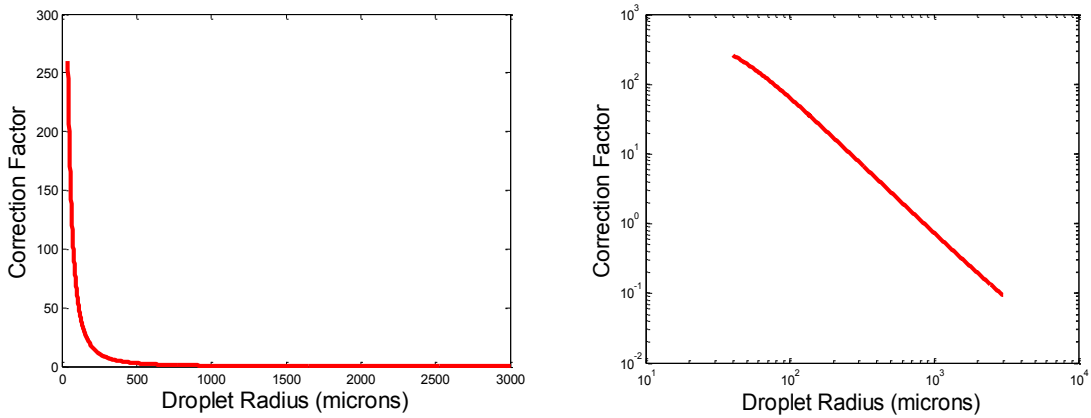


**Figure 3.25:** Plot of correction factor  $n_i$  as a function of droplet radius for camera 9139 (left). Same function plotted on log-log axes at right.

### 3.3 Assessing the Accuracy of the Corrections

Since the reticle has dots of known diameters it is possible to assess how accurately the out-of-focus correction function reproduces these values by feeding it the calibration data. Ideally, regardless of the position of the reticle, the function will be able to reliably reproduce the exact diameter of a given dot. The errors from these recalculations are shown in Figures 3.21 through 3.23.

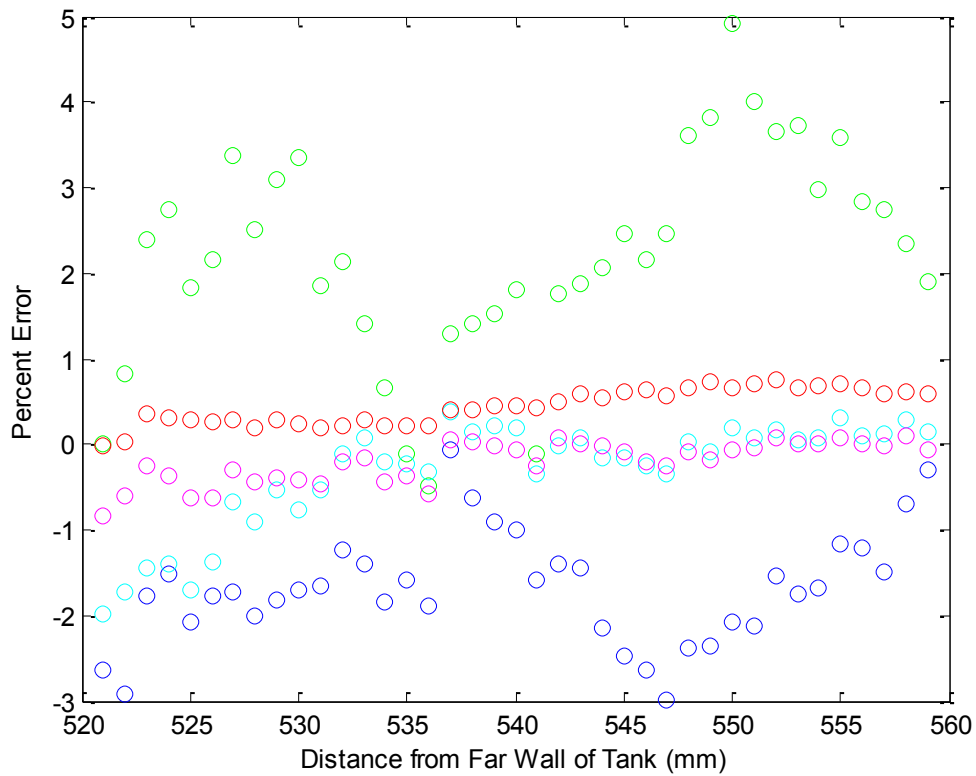


**Figure 3.26: Camera 9138—Error for calibration data after having applied the out-of-focus correction. Green: 100  $\mu\text{m}$ . Blue: 200  $\mu\text{m}$ . Cyan: 300  $\mu\text{m}$ . Magenta: 750  $\mu\text{m}$ . Red: 1000  $\mu\text{m}$ .**

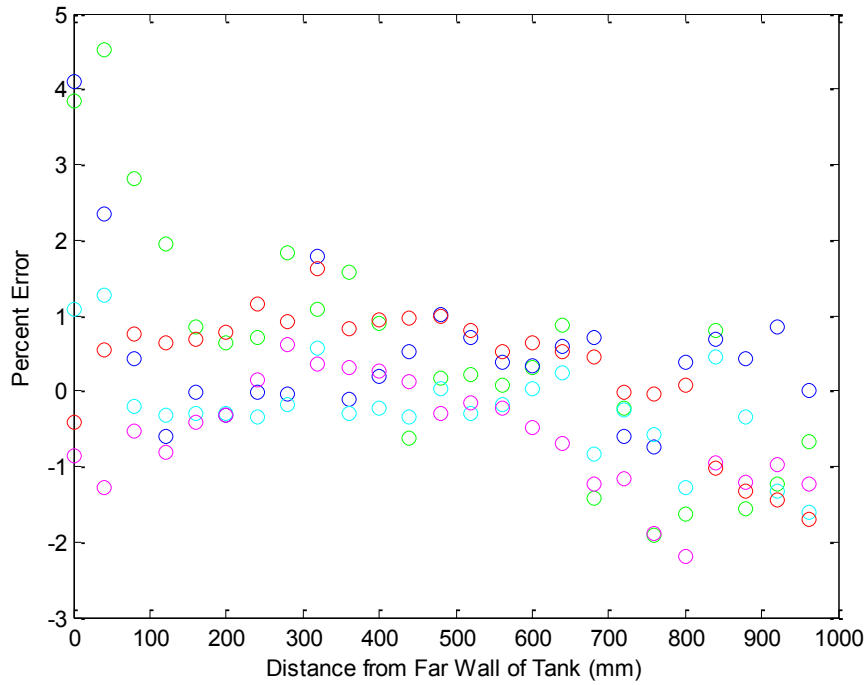


**Figure 3.27: Camera 9138—Error for calibration data after having applied the out-of-focus correction. Green: 1250  $\mu\text{m}$ . Blue: 1500  $\mu\text{m}$ . Cyan: 2000  $\mu\text{m}$ . Magenta: 2500  $\mu\text{m}$ . Red: 3000  $\mu\text{m}$ .**

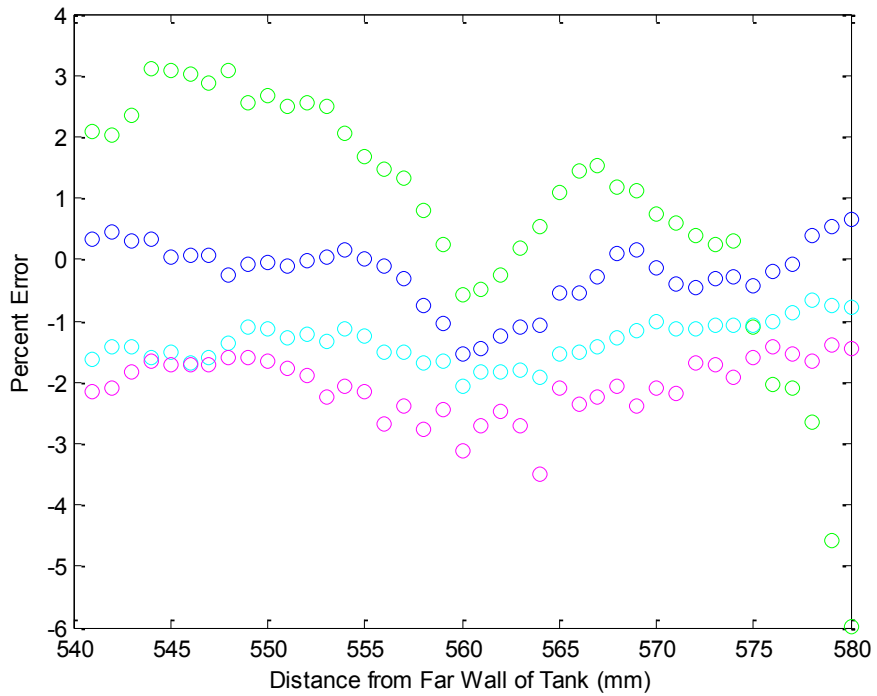


**Figure 3.28: Camera 9139—Error for calibration data after having applied the out-of-focus correction. Green: 300  $\mu\text{m}$ . Blue: 500  $\mu\text{m}$ . Cyan: 750  $\mu\text{m}$ . Magenta: 1000  $\mu\text{m}$ .**

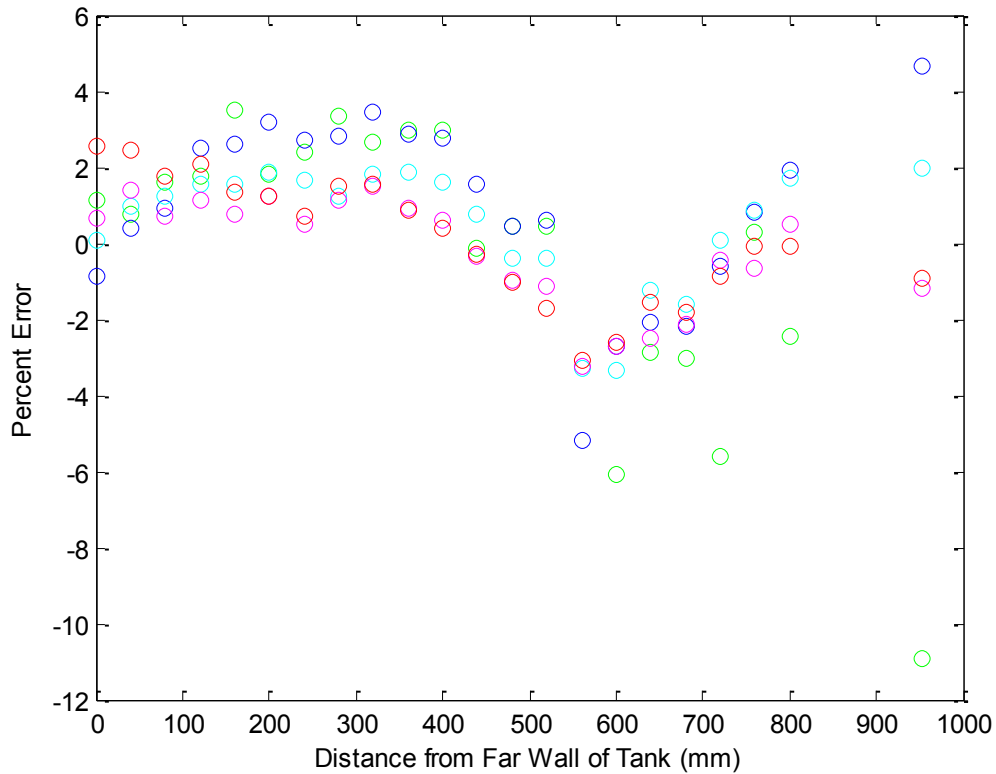


**Figure 3.29: Camera 9139—Error for calibration data after having applied the out-of-focus correction. Green: 1250 μm. Blue: 1500 μm. Cyan: 2000 μm. Magenta: 2500 μm. Red: 3000 μm.**

Across the range of dot diameters the error is confined to  $\pm 5\%$  except in a few cases where the calibration data was anomalous. Over the same distance, the uncorrected data ranged from +10% error for the 3000 μm dot to +40% error for the 100 micron dot (the uncorrected errors will nearly always be positive due to the dilation of the diameter away from the focal plane). Overall, smaller dots are subject to more error, but can also see greater improvements in measurement accuracy due to correction.

## Chapter 4: Droplet Measurement and Results for the 0.074 Amplitude Breaking Wave

The measurements for the 0.074 amplitude breaking wave were initially taken at 16 positions along the width of the viewing window. The naming scheme for the camera positions presented throughout the remainder of the paper is somewhat arbitrary. The camera positions range from 62 to 92 inches measured from the zero point of the instrument carriage from which the laser optics and cameras are suspended. The 62 inch carriage position corresponds roughly to 16 feet from the front bulkhead where the wave maker is located. The spacing between camera positions was 2 inches. The locations of the first and last camera positions were selected such that no droplets were observed throughout the course of 10 waves. This ensured that the remainder of the camera positions encompassed the full distance over which the wave produced droplets at 11.5 cm above the free surface.

After having conducted 10 runs at these 16 positions, it was noticed that a large number of droplets were produced at the 64 and 66 inch camera positions. The droplets at 64 inches were ejected from the wave with a horizontal component of velocity opposite to that of the wave packet's motion. At 66 inches the droplets were ejected with a horizontal velocity in the same direction as the travel of the wave packet. It was believed that the 65 inch camera position would also yield a large number of droplets with nearly completely vertical velocity. To confirm this, 10 additional runs were performed at the 65 inch carriage position. Indeed, this position yielded the most droplets of all positions and had droplet velocities which were almost completely in the vertical direction. Figure 5.1 below shows still frames with droplets and their general direction of travel.



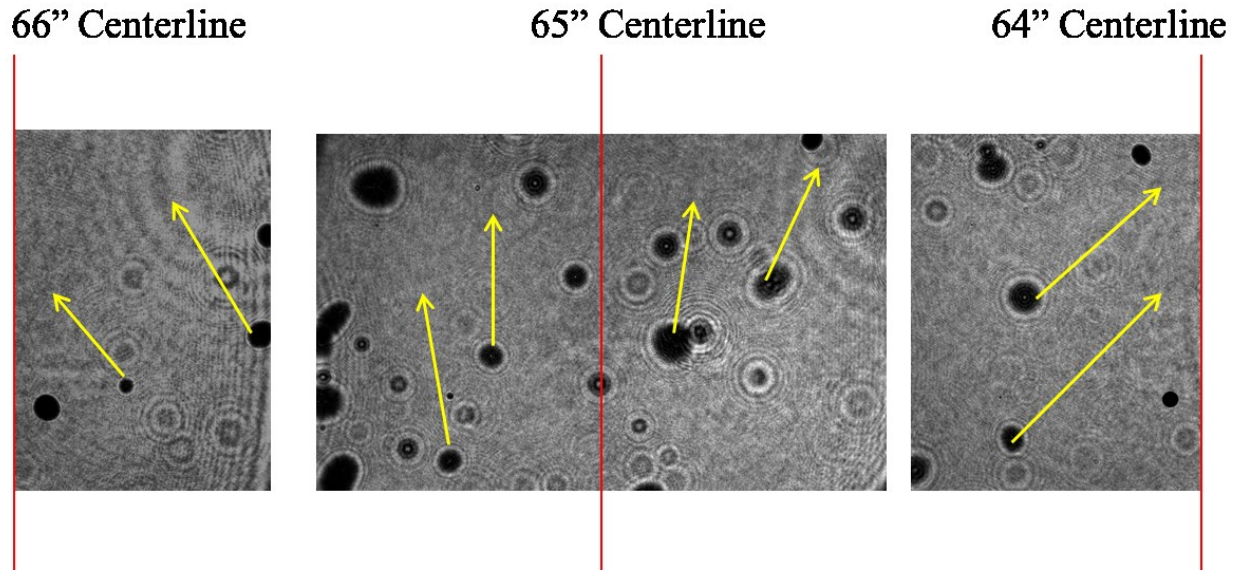


**Figure 4.1: Shadowgraph images from image sequences taken at the camera positions around the 65 in camera position with approximate velocity vectors.**

Thus, in all for the 0.074 amplitude wave, there were 17 measurement positions. Nine positions, including the additional runs at 65 inches were recorded with Camera 9138. The other eight positions were recorded with camera 9139. Figure 4.2 below shows these positions against the wave profile of the 0.074 amplitude wave.

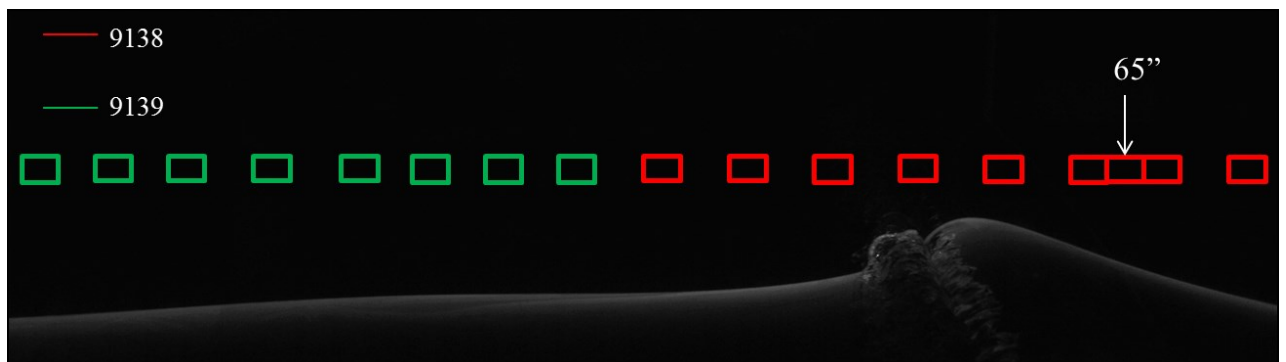


**Figure 4.2: Camera positions for the 0.074 amplitude breaking wave runs. Note the addition of a measurement position at 65 inches to capture the densest droplet production region along the length of the wave.**

To ensure that the surface tension was uniform from run to run, water was taken from the wave tank and the surface tensions was measured using the NIMA tensiometer mentioned previously. The results from these surface tension measurements are recorded in Table 4.1 below.

**Table 4.1: Surface tension of the water in the tank for all runs of the 0.074 amplitude breaking wave.**

Camera Position	Surface Tension (mN/m)
62-64''	72.4
66-68''	73.5
70-72''	73.0
74''	73.5
76''	72.8
65''	74.0

Following the completion of 10 runs each at all camera positions, the data was processed in a manner similar to the MATLAB script used for the calibration. The script used for the droplets, however, subtracted the intensity of the first image of each movie from each successive image. This removed much of the speckle, dust and droplets on the tank walls in the images and left the only the droplets. Then, the same hyperbolic tangent fit as was used before was applied to the droplets. For the remainder of this paper, a cutoff of 3900 for the *uncorrected* droplet statistics was selected to ensure a bias of no more than + 5%. These uncorrected statistics are only shown once (only for the 0.074 amplitude wave) to demonstrate the effect of this correction. They are not shown for the

remainder of the conditions. As noted previously, 3500 was used as the cutoff for the *corrected* distributions so that the error was limited to  $\pm 5\%$ .

One statistic compiled from the data was the total number of droplets observed at each position over the course of the runs. For all of the following data, the movies of image pairs were used to count only the droplets with a positive (upward) vertical velocity component and to only count each droplet once during the breaking event. Displayed below in Figure 4.3 are the droplet counts at each per position divided by the total number of droplets observed over the entire wave. This data is uncorrected for the effect of the droplet diameter-dependent depth-of-field on the measurement volume.

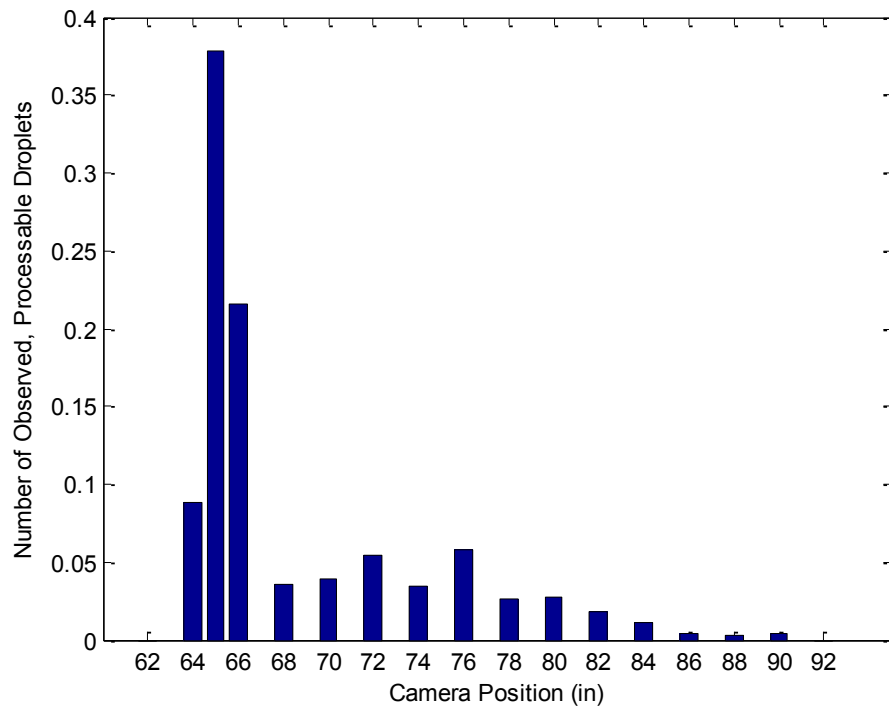


**Figure 4.3: Positional distribution of all droplets detected in the 0.074 amplitude breaking wave.**

As will be shown below, the droplets observed at the 64, 65 and 66 inch positions tend to be larger than the droplets observed further down the length of the wave tank. The positional droplet distribution after correcting for focus and depth-of-field is shown in Figure 4.4. Two of the three positions with the most droplets in Figure 4.3 still have the most droplets after correction, though the difference is reduced. Another potential bias, however, could have been that there were so many larger droplets in the imagery taken at the 64-66 inch range that they obscured some of the smaller droplets. Thus, the importance of the physical mechanism which contributed to the large number of observed droplet over this range of distances should not be ignored.

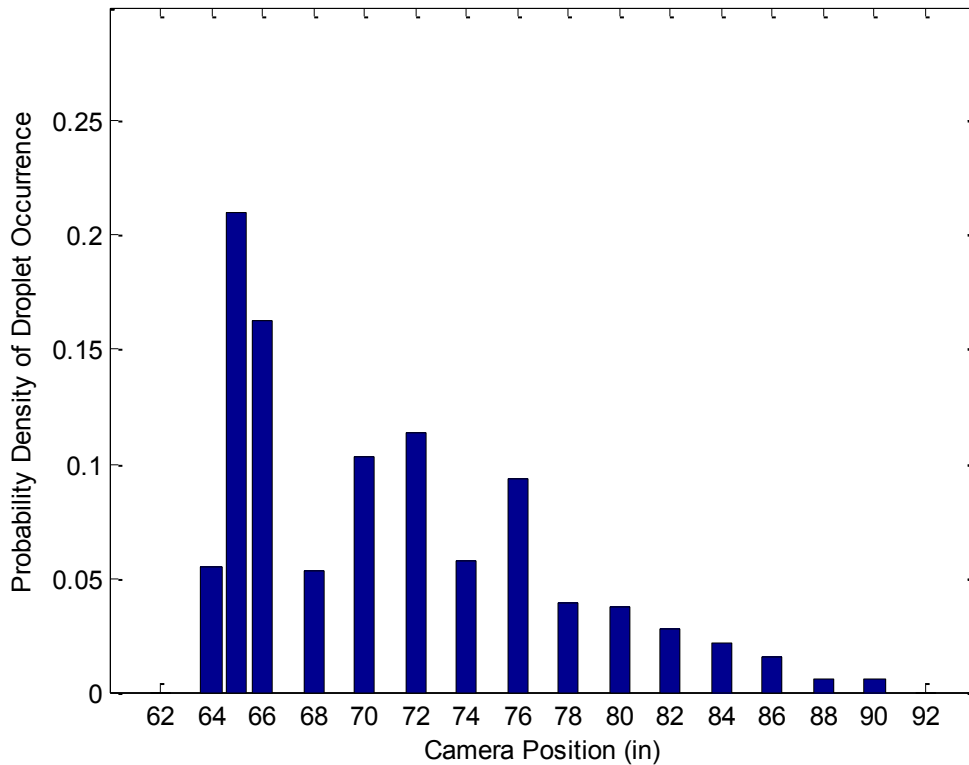


**Figure 4.4: Positional distribution of all droplets detected in the 0.074 amplitude breaking wave after applying the depth-of-field and focus correction.**

Droplet production is most abundant in the 64, 65 and 66 inch camera positions in the 0.074 amplitude wave. Overall, this region contributed over 40 % of all droplets observed. As the wave packet traveled down the length of the tank it generated droplets at a significantly reduced, albeit more steady rate. As the wave neared the end of the viewing window the fraction of total droplets produced waned and eventually went to zero at the final camera position. No droplets were observed at the two extreme camera positions over the course of 10 waves.

When this droplet distribution was correlated with the wave profile history, it became apparent that this observation coincided with the time and position of the impact of the wave's plunging jet with the front face of the wave. This event dissipates a portion of its turbulent kinetic energy in droplet generation.

Another issue of interest is the run-to-run variability in droplet generation. Figure 5.5 shows box plots for the droplet counts per run at each camera position. This graph displays the mean droplet count per run as a red horizontal line. The blue box surrounding this represents the middle 50 % of data recorded and the dashed black line extends to the maximum and minimum values. Red crosses represent statistical outliers from this distribution. As mentioned above, the first and last positions consistently recorded no droplets whatsoever. In the region of high droplet density from 64 to 66 inches a very large range of droplet counts per run was observed. Though the mean value reflects the spike recorded at these points, there are also runs at each one of these positions which record very few droplets at all. One potential explanation for this dearth of droplets is that the location of the impact of the wave crest varies slightly from run to run. Since each of the minima for these positions were recorded from different waves, it

may be possible that the wave broke in a manner that deposited significantly less droplets in this position while expending its energy elsewhere. Additionally, though the plunging jet impact occurred underneath the 65 inch camera position most often, one run from the 66 inch position recorded the highest number of drops of any run from any position. Of note, this run was a statistical outlier.

Throughout the remainder of the camera positions there are a significant number of statistical outliers. This is attributable to a large number of the camera runs in these positions recorded no droplets whatsoever. Despite there being more relative variation in runs at these positions, the range of droplet counts was much narrower.

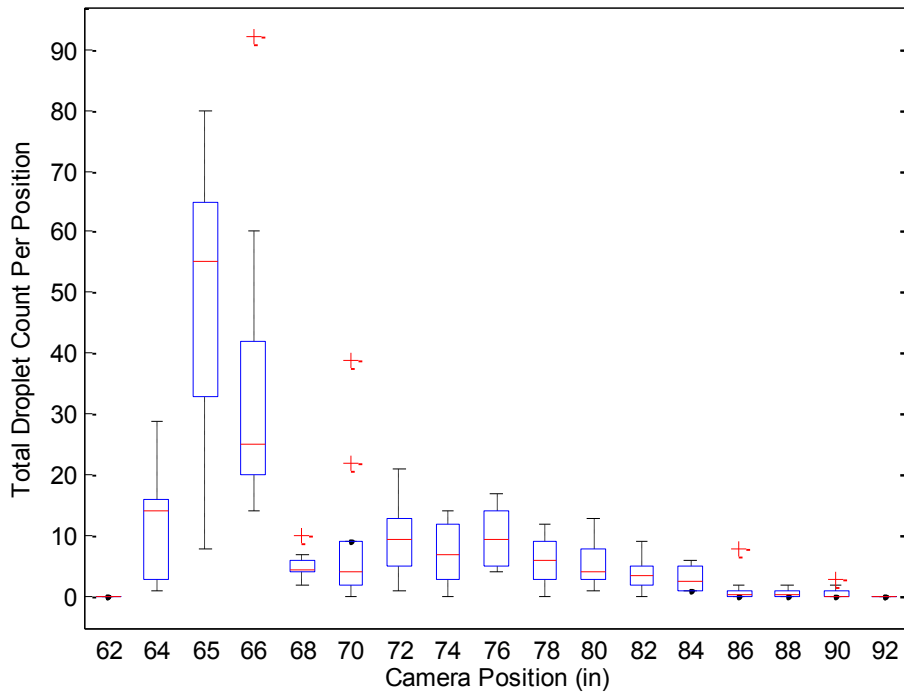


**Figure 4.5: Box plot of uncorrected droplet counts per wave per camera position. Blue box encircles middle 50% of data observed and black lines extend to maxima and minima excluding statistical outliers. Red line is the median droplet count of the 10 measurements at each position. Outliers are shown with a red cross.**

The observed droplet diameters were also calculated and consolidated for the entire wave event. The distribution of these diameters was normalized. Then, using the correction techniques discussed in the preceding chapters, these droplet measurements were adjusted. The uncorrected droplet distribution is shown in Figure 4.6 and the corrected distribution is shown in Figure 4.7.

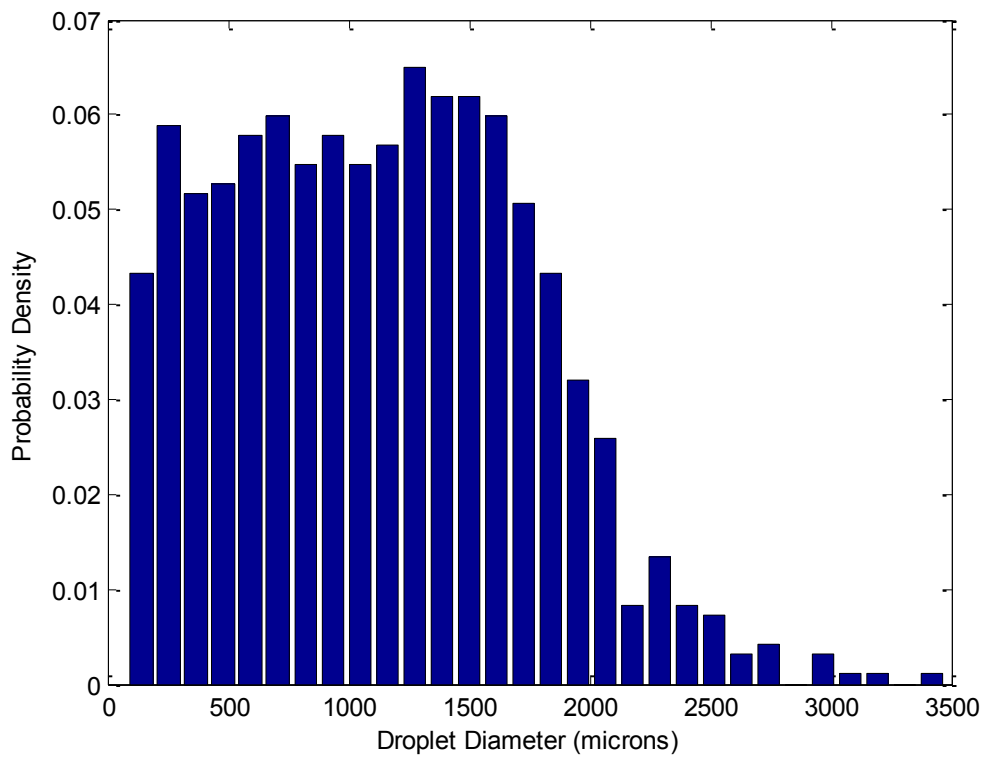


**Figure 4.6: Uncorrected droplet diameter distribution for all droplets observed in 10 breaking events of the 0.074 amplitude wave.**





In the uncorrected distribution, droplet diameters associated with splashing droplets predominate with significant contributions from the smaller diameter jet and film droplets from the bursting of bubbles rising to the surface. There are also a number of observed droplets that exceeded 3000  $\mu\text{m}$ . Most likely, these droplets were torn from the wave rather than being produced through the bursting of air bubbles. The shape of these droplets was asymmetric and oscillatory rather than spherical as was the case for the smaller droplets. This behavior is likely due to the influence of surface tension, which is known to decrease with increasing droplet diameter. For the processing of these droplets, the frame in which the droplet appeared most closely spherical was chosen to calculate the diameter. In many cases however, this was merely an approximation as the droplets sometimes never fully appeared spherical.

Due to the droplet diameter corrections, the diameter distribution was shifted from a sigmoidal shape to an exponential one—heavily favoring the smaller droplet diameters. At the very low end of droplet diameters, the distribution appears to decrease. This may not be present in the actual distribution of diameters because the experimental method used is not capable of detecting droplets down to an infinitesimally small size. As stated in Chapter 2, the absolute lower threshold on droplet detection is 3 pixels, which corresponds to approximately 30  $\mu\text{m}$ . Practically, when dust and speckle are introduced into the image, this limit is raised to 50  $\mu\text{m}$ . Thus, it may be possible that the probability density increases with decreasing droplet size beyond the diameter shown in Figure 4.7.

On the other hand, the probability density of the large, asymmetric droplets is very small in the corrected distribution. The distribution is not perfectly exponential, either. Due to the largest probability densities occurring from 1,000 to 1,500  $\mu\text{m}$  in the

uncorrected data, there appears to be a shelf around these lengths on the corrected distribution.

The droplet diameter distribution was re-plotted in a log-log coordinates and is shown above in Figure 4.8. This graph has two distinctive negatively sloped sections with a jump from the shallower to the steeper slope at approximately 1,250  $\mu\text{m}$ .

Interestingly, the shape of this distribution is similar to the findings of Wu, et al. (1984).

Also, the droplet diameter distributions were separated by camera position to investigate whether the droplet size was affected by the stage of the wave breaking event, which increases in distance from the wave maker as the breaker progresses in time. This is displayed in Figure 4.9 in which only the positions that had a sufficient number of droplets to compute a stable distribution are displayed. An interesting feature of this splitting of the diameter distributions is that the piecewise shape is confined to the positions where the jet impacts the surface, 64, 65 and 66 inches. The droplet diameter distributions of these positions resemble that of the all droplets from all positions. However, at the later positions, the distributions appear to follow a single power law. Because the majority of the droplets in the entire wave are observed within the 64-66 inch interval, the overall distribution appears piecewise as well. However, if one were merely interested in droplet generation away from the breaking event, this model would be inappropriate.

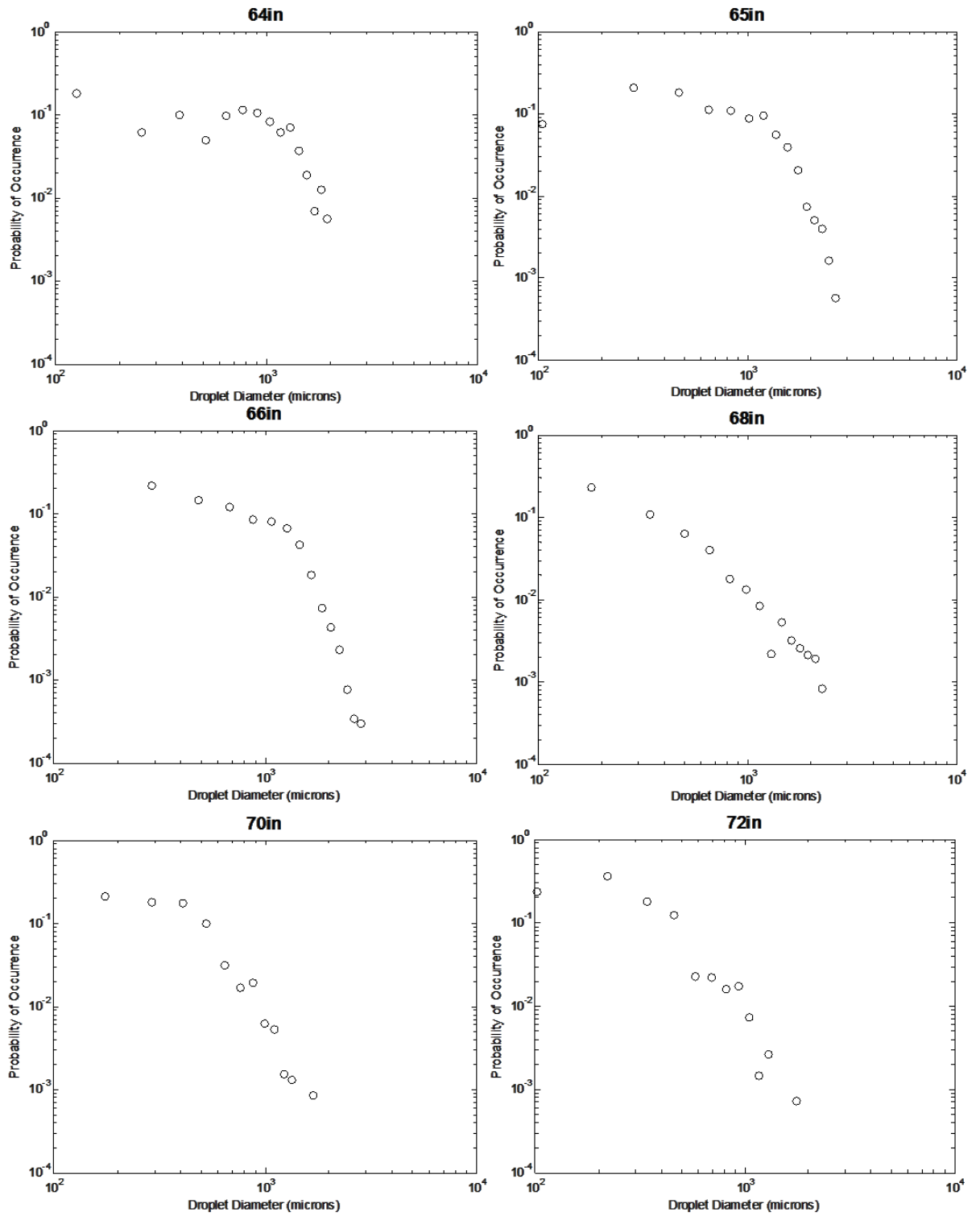


**Figure 4.9: Corrected (focus and depth-of-field) droplet diameter distributions for the 0.074 amplitude wave in log-log plots for various camera positions as noted above each plot.**

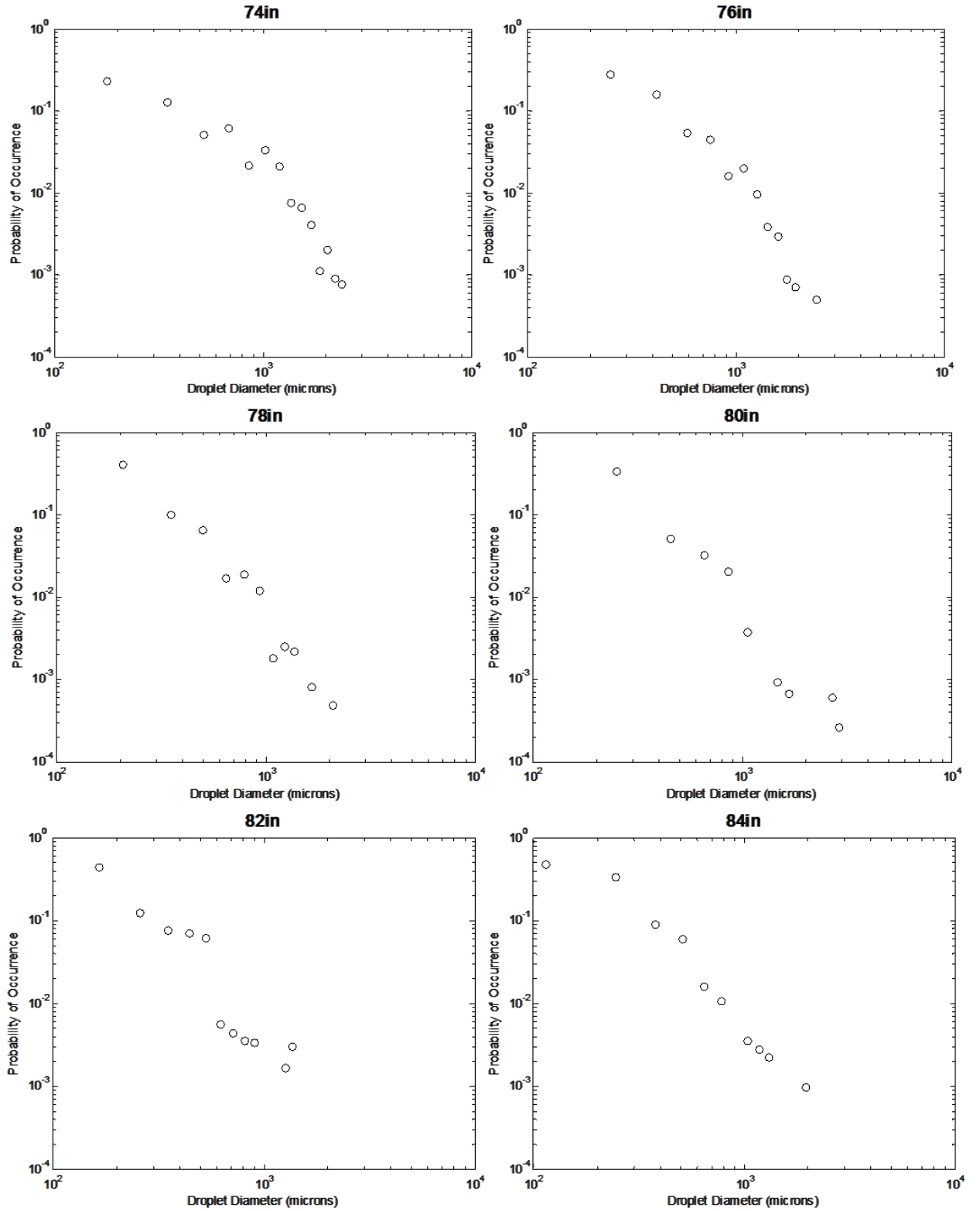
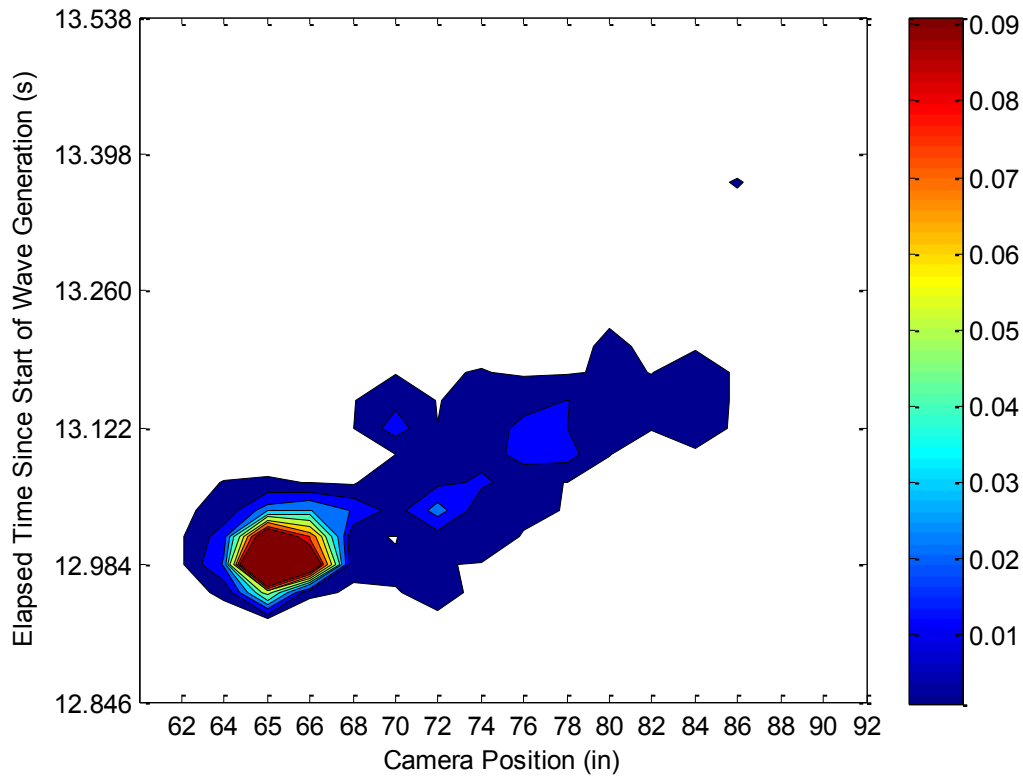


Figure 4.9 (Continued).

Next, the number of droplets produced per frame (recall that all the droplet movies are synchronized to the start of the wave maker motion) was plotted as a function of time and position in order to determine when and where the majority of the droplets were produced. Unsurprisingly, the 64, 65 and 66 inch positions see proportionately more droplets than any other locations as was shown in Figures 4.3 and 4.4. Not only are the majority of the droplets associated with the location of the crest impacting the front face of the wave, but this droplet production is also compacted into a relatively short amount of time. More than 50 % of all the droplet production is confined to an interval of less than 150 ms. As the wave travels down the tank, the camera positions further down the tank record droplets at correspondingly later times—though not nearly at the generation frequency of the three positions centered on the impact of the jet.

The dramatic influence of the sudden release of droplets is even more apparent in the normalized and corrected probability distribution. Again, this distribution indicates that many of the droplets in the 0.074 amplitude wave are being generated in this impact through the production of splashing droplets, rather than later as entrained air rising to the surface and producing film or jet droplets.



**Figure 4.10: Corrected (focus and depth-of-field), normalized total droplet number probability density versus distance along the wave tank and time for droplets at 12cm from the free surface in the 0.074 amplitude breaking wave.**

Graphs showing droplet production rate versus time were generated to further investigate the expending of energy. The corrected plot is shown in Figures 4.11. In these graphs the droplet count on a 15 frame interval was multiplied by the 650 Hz frame rate in order to track the droplet production rate. It was necessary to bin this rate together into 23 ms intervals in order to reduce noise in the distribution. The droplet production rate peaks very quickly and diminishes at approximately the same rate, with the center of the spike occurring at approximately 13 seconds after the wave maker was triggered. Again, this peak coincides with the plunging jet impact. There also appears to be a smaller, more gradual secondary increase in the production rate at approximately 150 ms

after the first maximum. To some extent, the timing of droplet observation is influenced by the location of the free surface relative to the camera. Prior to the passage of the wave packet, the free surface is undisturbed and the camera height is held at a constant 12cm. As the wave passes, however, the surface is at times much farther or closer than 12cm. Droplet densities increase with proximity to the surface. Thus, any following spikes in the production of droplets may be attributable to the free surface approaching the experimental volume, and correspondingly any troughs in droplet production could be caused by a more distant free surface.

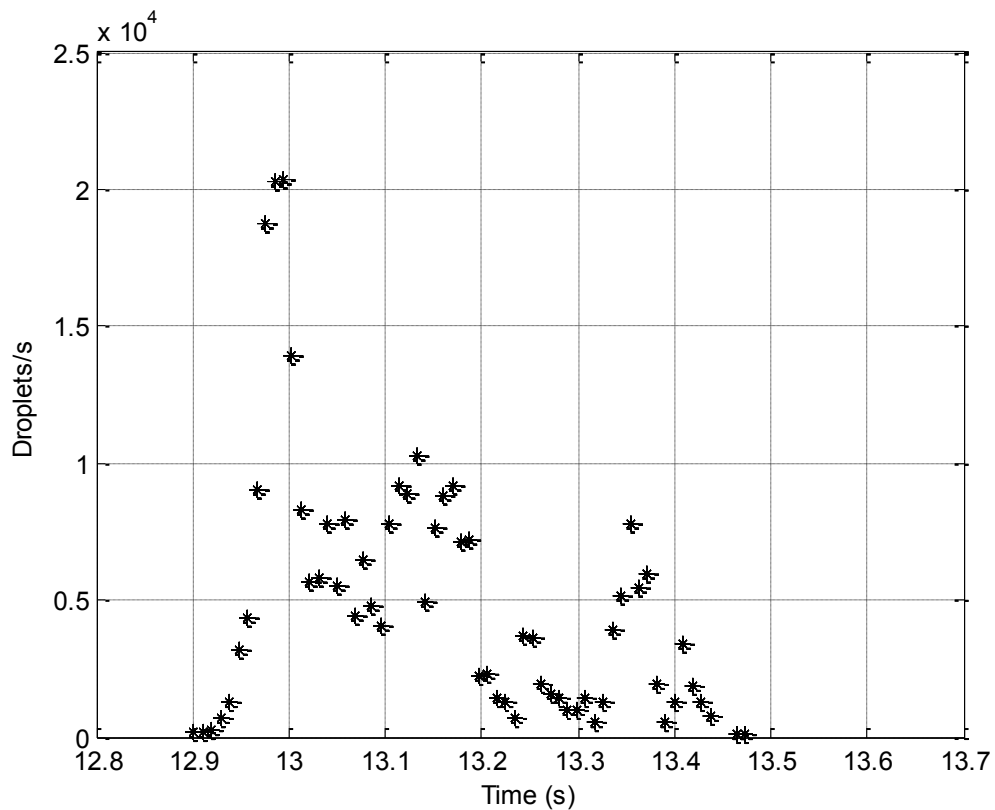


**Figure 4.11: Corrected (focus and depth-of-field) droplet production rate as a function of time for the 0.074 amplitude breaking wave.**

## Chapter 5: Droplet Measurement and Results for the 0.070 Amplitude Breaking Wave

The 0.070 amplitude breaking wave was measured using the 16 camera positions detailed in Chapter 2. Interestingly, this lower amplitude wave did not possess as extensive of a positional bias that the 0.074 amplitude wave did. Whereas previously nearly 50% of the droplet production was confined to a 3 inch wide volume, the droplets were more uniformly distributed in the 0.070 amplitude wave. Because of this, there was no need to include an additional measurement position.

Using the same method as the previous wave, the probability density of droplet detection was plotted as a function of distance from the wave maker. The breaking location of the lower amplitude wave was also very nearly coincident with the 65 inch camera position. Despite this, droplet probability density was not highest here. Overall the distribution was moved downstream relative to the 0.074 amplitude wave.

After having applied the droplet diameter corrections, the positional distribution shifted somewhat closer towards the breaking location of the wave. This is contrary to the shift observed in the higher amplitude wave wherein the probability density increased in the latter positions after having applied the correction. This was partly attributable to the higher incidence of smaller droplets across a wider positional distribution. The high density of droplets in some images may have blocked observation of some of the smaller droplets. In the 0.070 amplitude wave, however, smaller droplets are more commonly observed closer to the breaking location. The incidence of drops also trails off more quickly in the lower amplitude wave. The amplitude of the wave maker's motion is lower meaning that there is less energy in the wave. The lower amount of droplets



observed overall reflects this. Figure 5.1 shows the corrected positional distribution for spray droplets in the 0.070 amplitude wave.

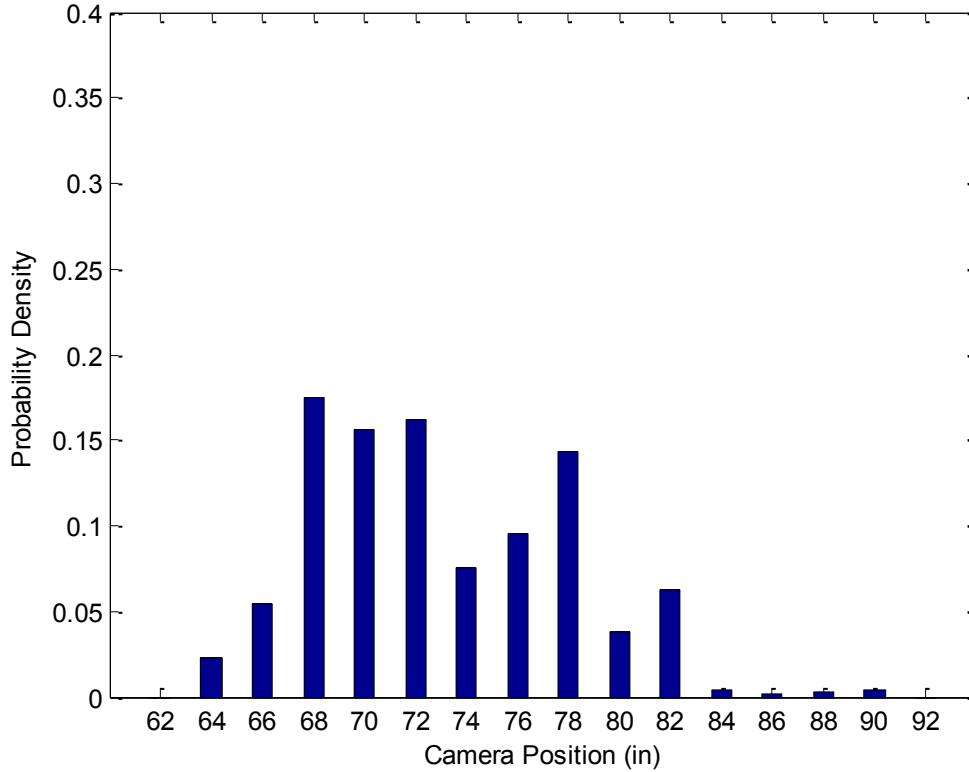


**Figure 5.1: Corrected (focus and depth-of-field) probability distribution of droplets as a function of position in the 0.070 amplitude breaking wave.**

As with the higher amplitude wave, the run-to-run variation was displayed with a box plot, shown in Figure 5.2. Beyond 82 inches, any detection of droplets is an outlier. Like the higher amplitude wave, the largest variation in droplet counts is observed in the positions with highest average counts. At each position throughout the distribution, it would not be unexpected to observe a wave run in which very few droplets were recorded. Overall, though, the average droplet count per position was significantly less than those observed in the 0.074 amplitude wave.

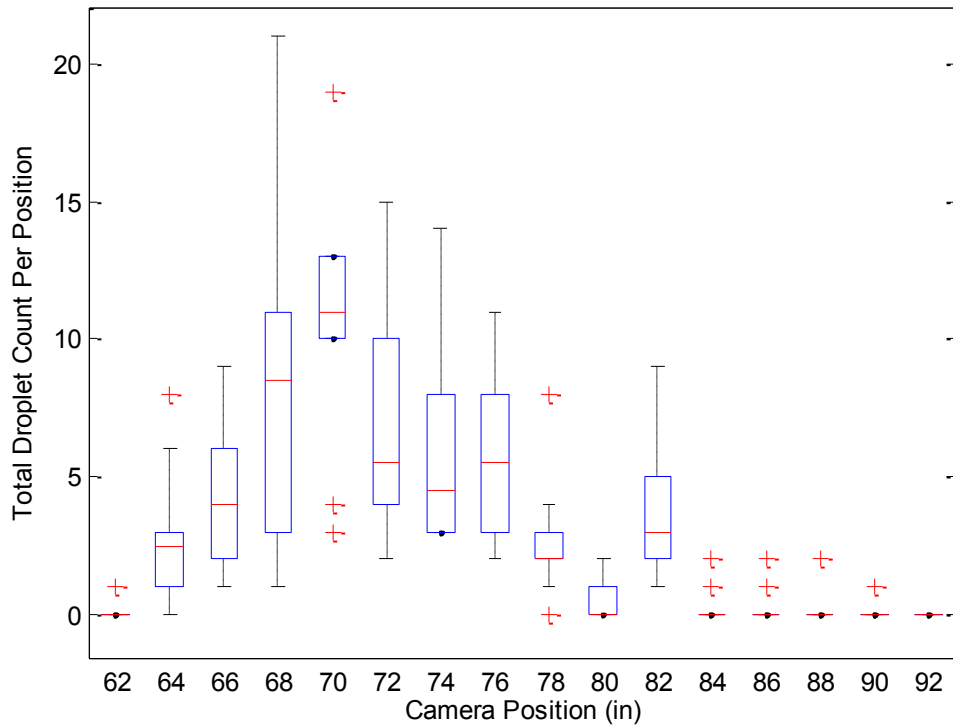


**Figure 5.2: Box plots of droplet counts for the 0.070 amplitude breaking wave.**

The raw droplet diameter distribution for the 0.070 amplitude wave is shown in Figure 5.4. This distribution appears to take a lognormal shape and is much less uniform than the higher amplitude wave through the middle range of droplet diameters. The distribution does fall off rapidly when the diameter increases beyond 1,250  $\mu\text{m}$ . Droplet observation beyond 2,000  $\mu\text{m}$  is sporadic.

The corrected droplet diameter distribution and associated log-log plot are displayed in Figures 5.3 and 5.4. The shape of the distribution was not as radically changed as the distribution for the 0.074 amplitude wave as it already favored smaller droplet diameters. The drop-off in the distribution is more accelerated, however. The transition from the shallow to steep slope regions seen in the higher amplitude wave is less definite in the 0.070 amplitude wave. At the extremes of this distribution there was

more noise in the 0.070 case. This would be expected as overall fewer droplets were observed in ten runs of the 0.070 amplitude wave than the 0.074 amplitude wave. For the same reasons cited in Chapter 4, the falloff in the distribution at the lowest observed diameters may be a result of measurement limitations rather than any physical phenomenon.

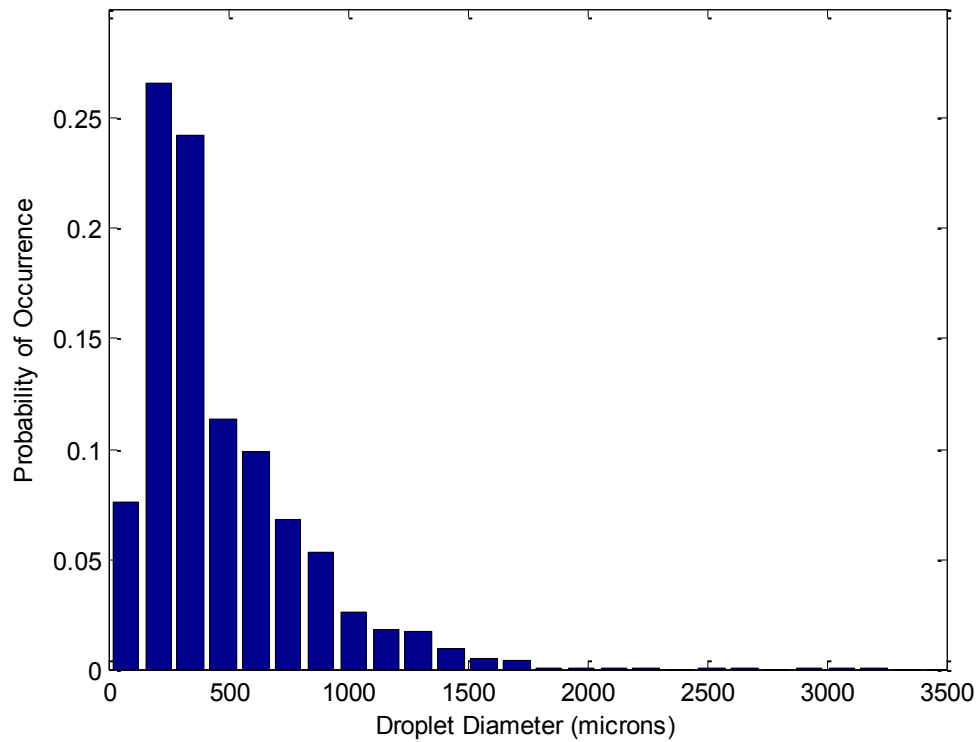


**Figure 5.3: Corrected (focus and depth-of-field) diameter distribution for 10 runs of the 0.070 amplitude breaking wave.**

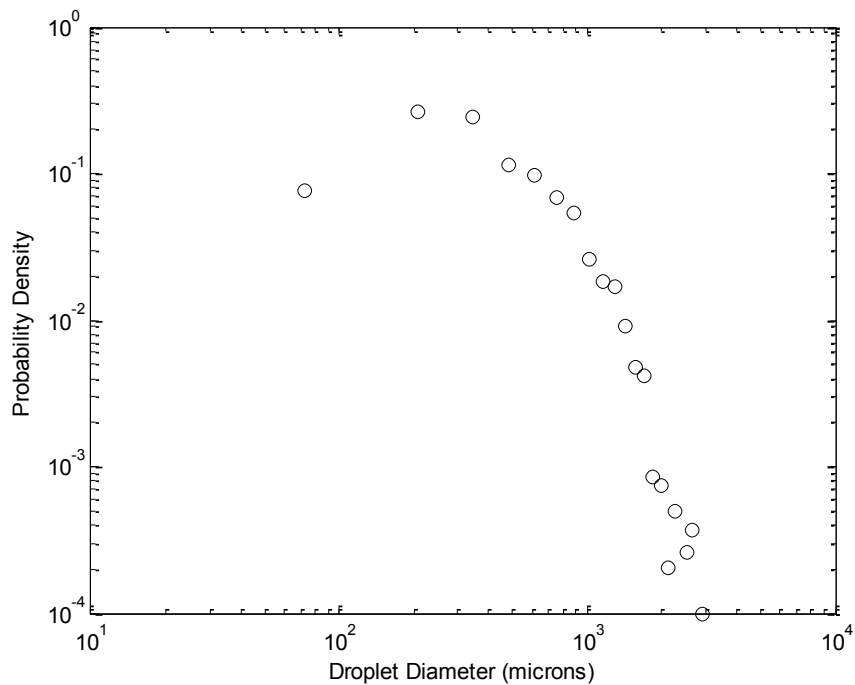


**Figure 5.4: Log-Log corrected (focus and depth-of-field) diameter distribution for the 0.070 amplitude wave.**

As was performed previously, the overall diameter distribution was separated by position and is displayed in Figure 5.5. The piecewise shape is not nearly as apparent in the overall distribution and is almost absent in the distributions separated by camera position. This wave did not display a breaking event that was nearly as energetic as the 0.074 amplitude wave. Since the two-slope shape of the distribution in the 0.074 amplitude wave resulted from droplets in the 64-66 inch positions, and very few droplets were observed around this position in the 0.070 wave, this shape is less distinct in the lower amplitude wave. Except for the 68 and 70 inch positions (which displayed higher droplet intensities than other positions) a single power law is sufficient to describe the distribution of droplet diameters. Less positions were displayed in the figure because

there were significantly less droplets overall, making it improper to display a distribution for the sparsely populated camera locations.

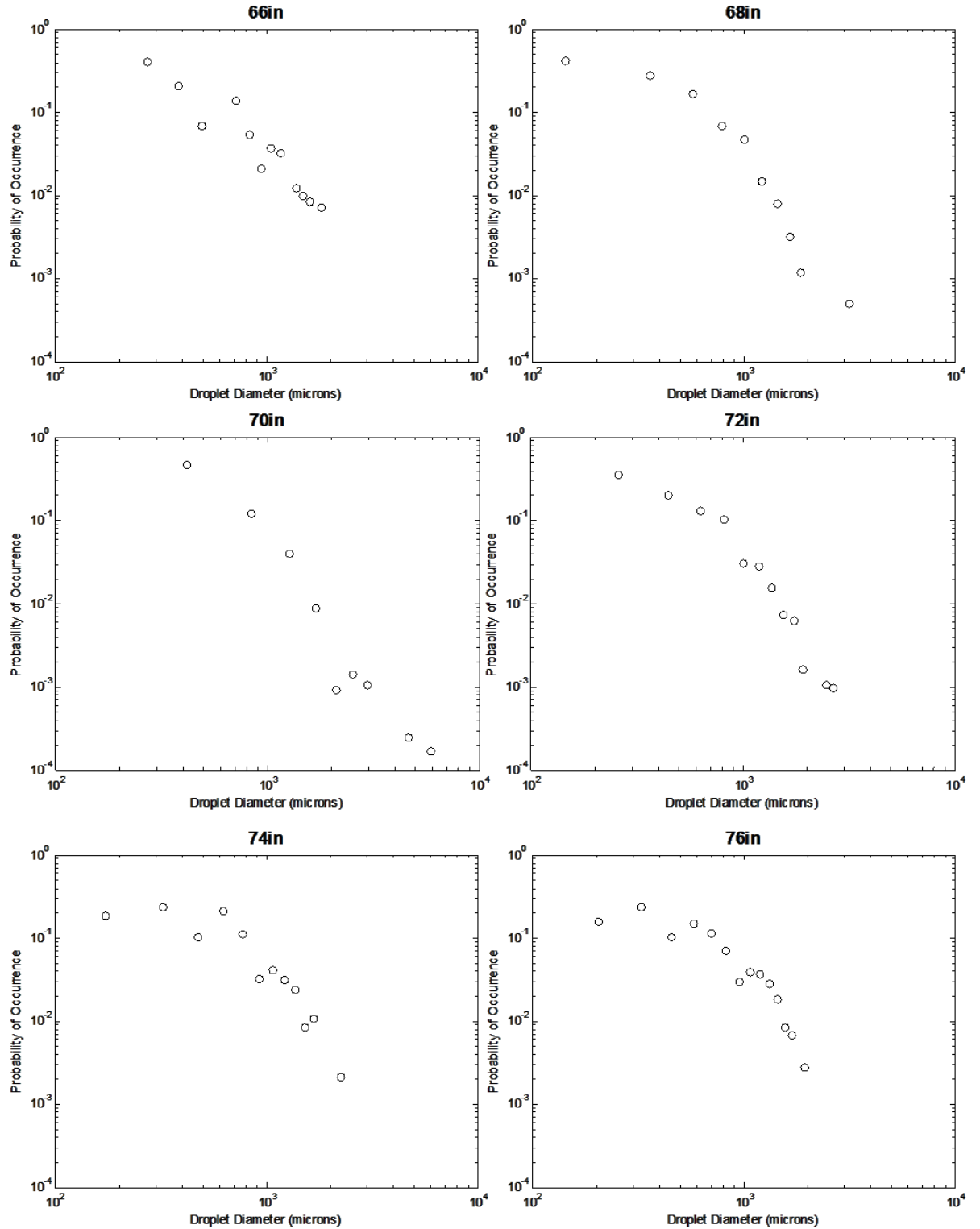
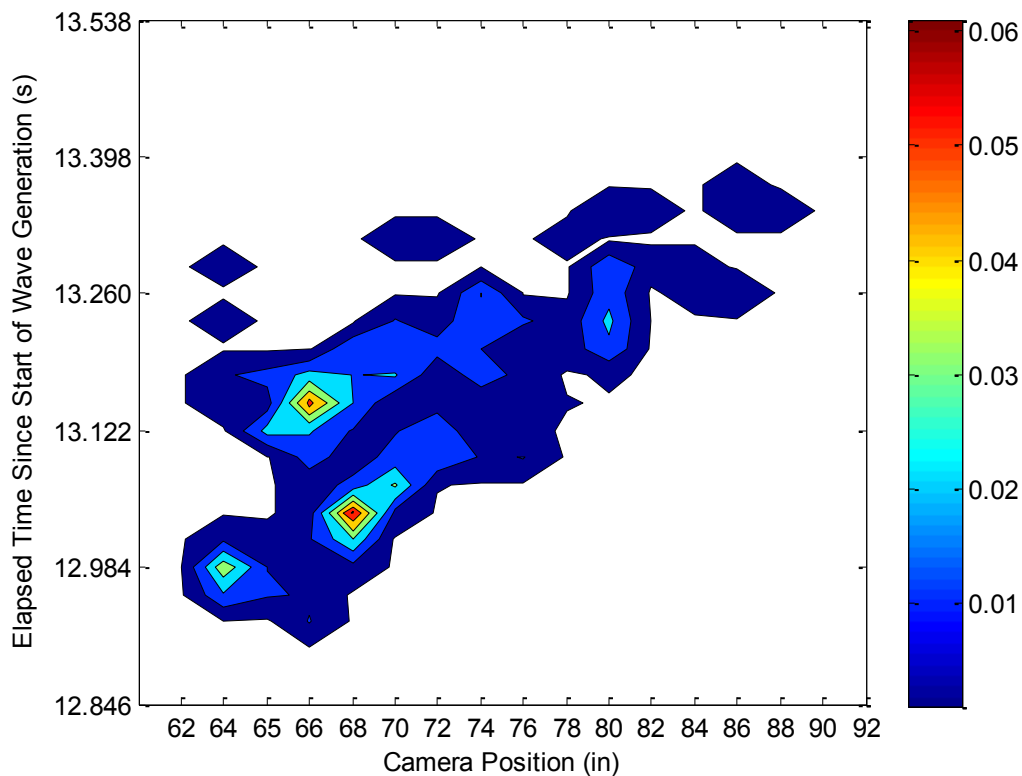


Figure 5.5: Corrected (focus and depth-of-field) droplet diameter distributions for the 0.070 amplitude wave in log-log plots separated by camera position.

The contour plot of droplet count as a function of position and time is displayed in Figure 5.6. The timing and position of the highest droplet intensities is approximately the same as the previous wave. However, there appears to be two peaks in droplet production at approximately the same position but different times. It is difficult to associate this shape to any distinct wave phenomenon, other than the more gradual and less dramatic plunging action of the wave crest in the 0.070 amplitude wave.



**Figure 5.6: Corrected (focus and depth-of-field), normalized total droplet number probability density versus distance along the wave tank and time for droplets at 11cm from the free surface in the 0.070 amplitude breaking wave.**

The corrected droplet production rate is displayed in Figure 5.7. This plot assumes a more gradual rise and fall than the production rates for the 0.074 amplitude wave. There is a small shelf in the distribution starting at 13 seconds which can be associated with the spike in droplet production near the 68 inch camera position. The

production rate reaches its high point later at 13.2 seconds which is roughly associated with the second positional peak. However, at this time droplet production is high at many other positions which contributed to the absence of the double peak feature. Overall, the magnitude of the production rate is significantly less than the higher amplitude wave due to the lower amount of energy being dissipated.

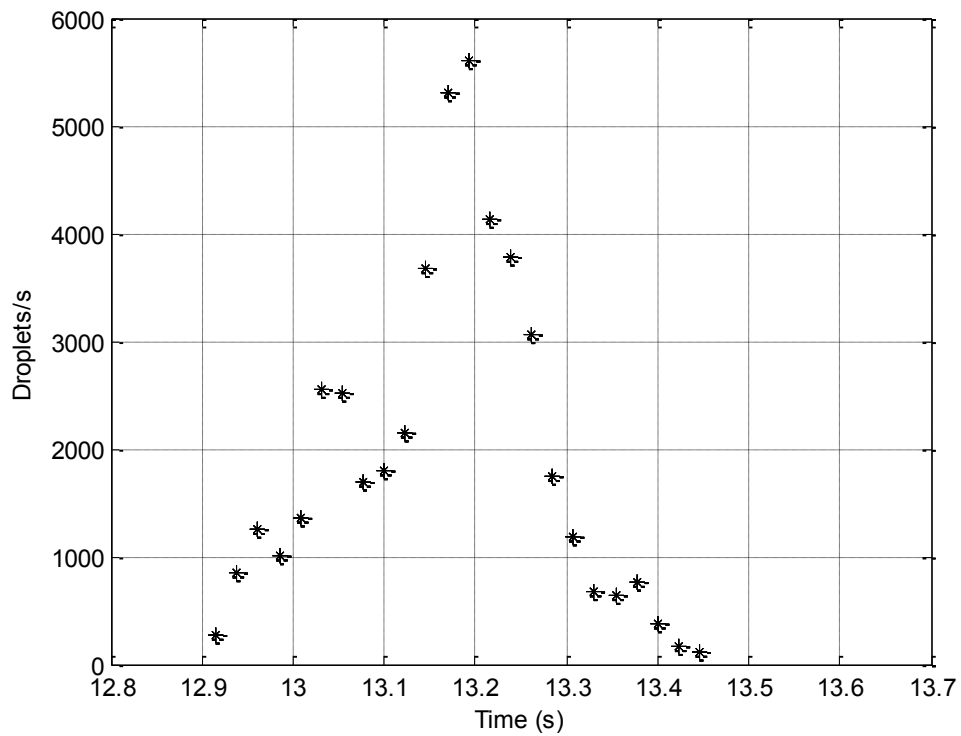


**Figure 5.7: Corrected (focus and depth-of-field) droplet production rate as a function of time for the 0.070 amplitude wave.**



## Chapter 6: Droplet Measurement and Results from the 0.074 Amplitude Wave with Surfactant

In the experiments described in this chapter, all of the parameters of the 0.074 amplitude wave were kept constant but surfactant was added to the tank. The measurement locations were altered to focus on the locations where the most droplets were observed in the 0.074 amplitude wave without surfactant. Additionally, measurements at 62 inches were dropped as no droplets were found at this position previously. One circumstance of omitting measurement at 62 inches on the Camera 9138 was that no measurements were taken at 78 inches on Camera 9139. The loss in overall data was initially presumed to be negligible, as the fraction of all droplets observed at this position previously was less than five percent. With this approach it was believed that only 5 runs instead of 10 would be sufficient to produce enough data to draw conclusions. The measurement scheme is shown below in Figure 6.1:

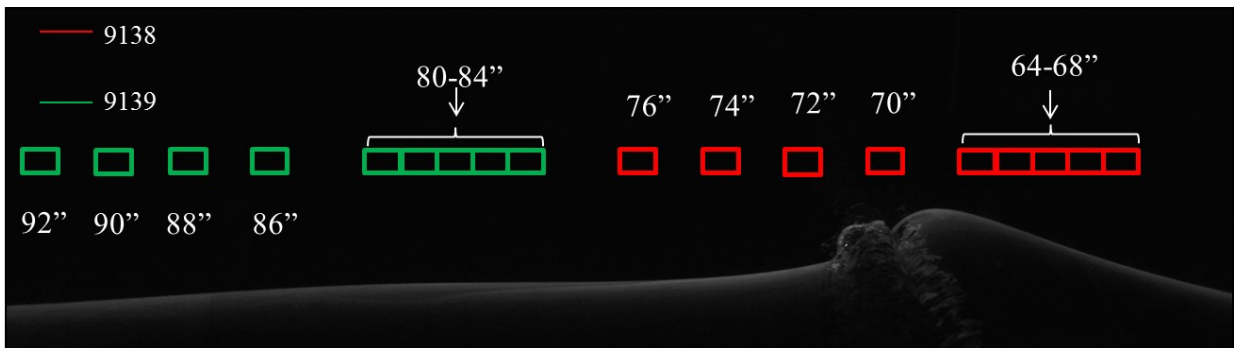


**Figure 6.1: Camera positions for the 0.074 amplitude with surfactant runs. Measurement locations have been concentrated around the location of the wave breaking phenomenon in the 0.074 amplitude wave.**

The addition of surfactant significantly altered the positional distribution of observed droplets compared to the 0.074 amplitude wave in clean water. This can be

seen in the probability distribution shown in Figures 6.2 compared to the distributions shown in Figure 4.3 and 4.4. Unfortunately, the positioning of the additional measurement locations was less than fortuitous: the locations of the highest droplet densities shifted farther down the wave tank and were not observed in the region of closely spaced measurement positions. The large spike around the 65 inch position seems to have been suppressed or at least delayed and reduced in intensity. The position-based probability is also more evenly distributed. Perhaps also, the most interesting part of the droplet generation was omitted unintentionally. Whereas the region after the 78 inch camera position produced very few droplets, the 78 inch position constitutes a transition from upstream positions where only a few droplets are generated. In the corrected distribution the 72 inch position is the maximum of the distribution. Thus, more runs are needed to make any definitive statement on droplet generation between 72 and 80 positions.

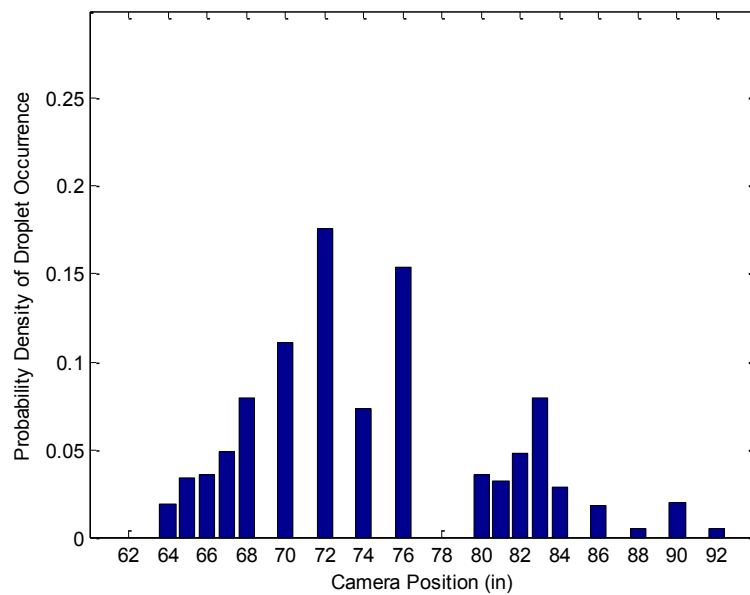


**Figure 6.2: Corrected (focus and depth-of-field) probability distribution of droplets as a function of position in the 0.074 amplitude wave with surfactant.**

The run-to-run variation in the surfactant waves is rather unremarkable. This distribution can be seen in Figure 6.3. For every position, it is possible to have a run in which no droplets were observed. In fact, the runs in which the majority of the droplets had been observed were quite far from the median value. One significant outlier was observed in the 5 runs taken at the 76 inch position. The movie associated with this event resembled the behavior from the 65 inch position in the same wave without surfactant, except that the observed droplets were smaller in size.

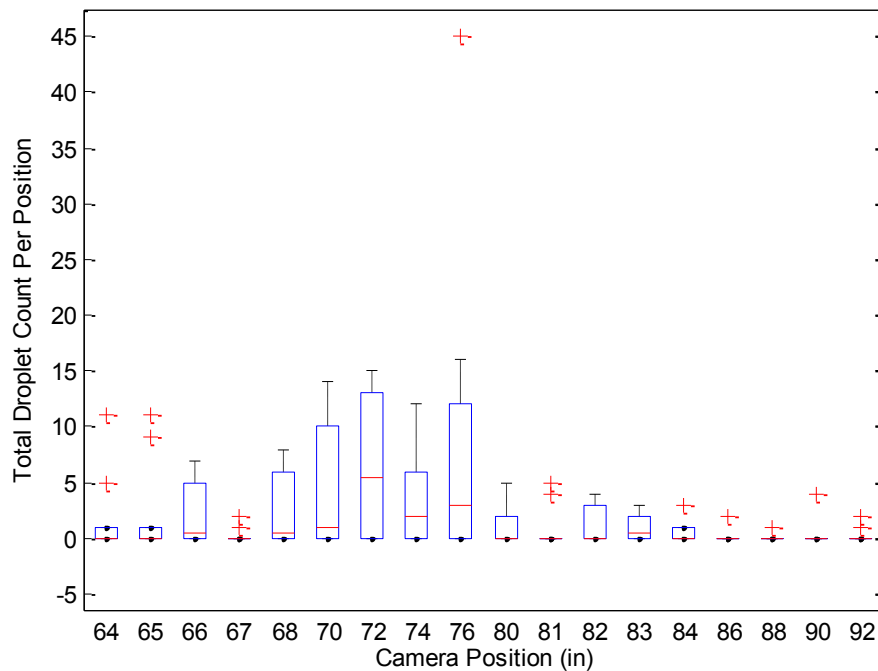


**Figure 6.3: Box plots of droplet counts for the 0.074 amplitude wave with surfactant.**

Unlike the dramatic change to the positional droplet distributions, the diameter distributions reflected the anticipated change: the droplets observed were generally smaller than before. After applying the corrections for focus and depth-of-field, over 60% of the droplets generated are less than 500  $\mu\text{m}$ . The occurrence of droplets around

1,500  $\mu\text{m}$  and beyond is significantly lower than the same wave except without surfactant. These effects can be seen in Figure 6.4. In the log-log distribution, shown in Figure 6.5, the droplet size seems as though it may not obey a piecewise distribution as seen before.

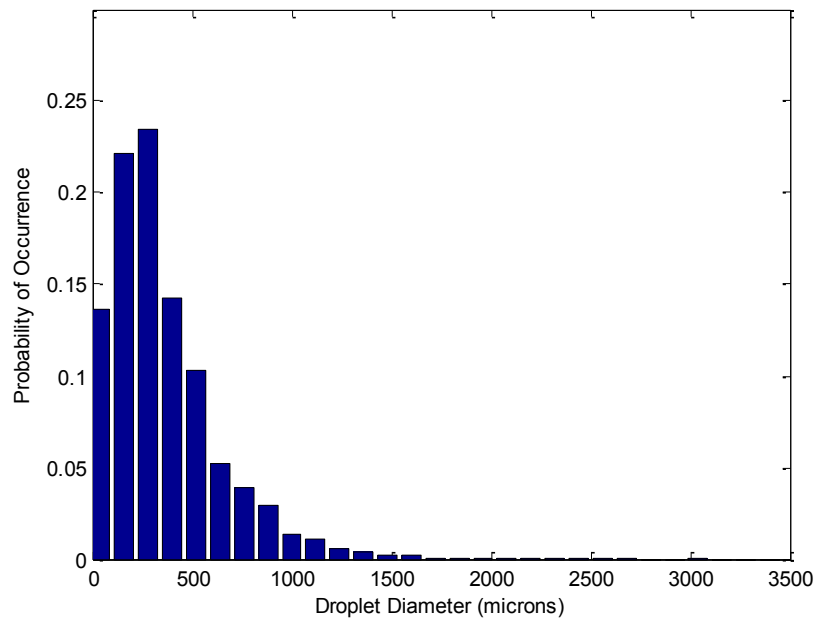


**Figure 6.4: Corrected (focus and depth-of-field) diameter distribution for 10 runs of the 0.074 amplitude wave with surfactant.**

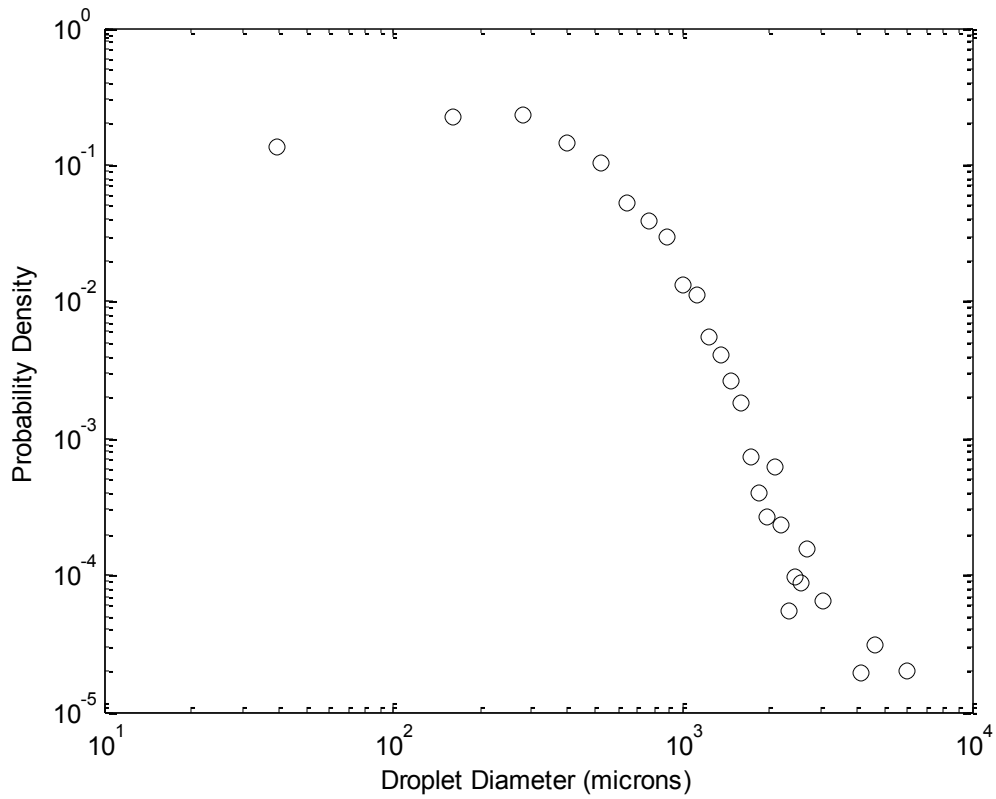


**Figure 6.5: Log-log diameter distribution for the 0.074 amplitude wave with surfactant.**

Additionally, the droplet diameter distributions have been broken down by camera position and are displayed below in Figure 6.6. While the 0.074 amplitude wave without surfactant had piecewise distributions at the locations of highest droplet density this effect was largely absent from the wave after surfactant was added to the tank. On the log-log axes, these distributions take a roughly linear shape.

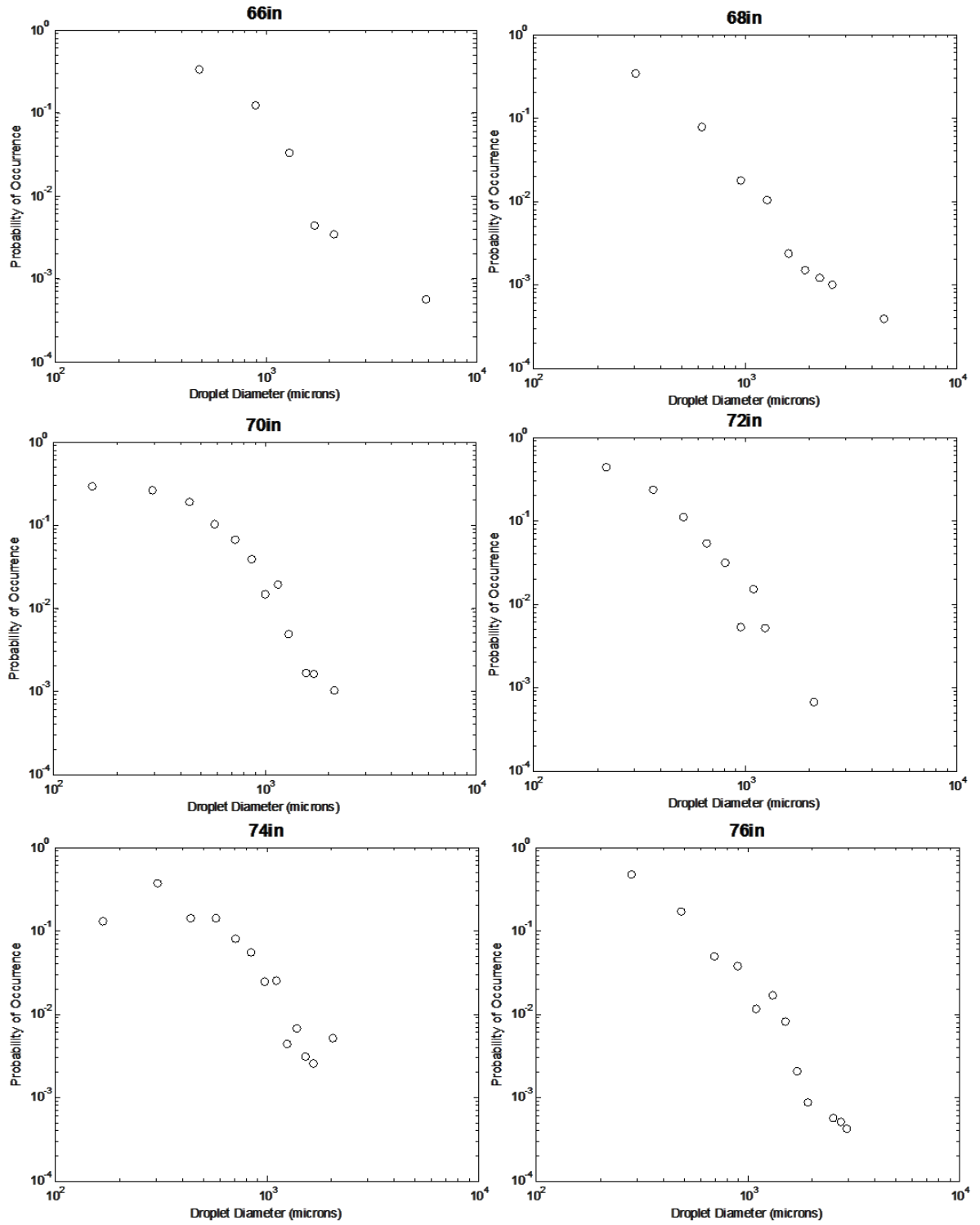


**Figure 6.6: Corrected (focus and depth-of-field) droplet diameter distributions for the 0.074 amplitude wave with surfactant in log-log plots separated by camera position. Positions selected represent those with the highest droplet densities. Note that the piecewise shape previously observed in this wave without surfactant is largely absent.**

The contour plot of probability versus time and measurement position for the surfactant runs is displayed in Figure 6.7. One significant difference from the wave without surfactant is that droplet production seems to be confined to the same time range across the length of the measurement positions. Without surfactant, measurement positions that were further down the tank detected droplets at a later time than the positions closer to the wave maker. With surfactant present, this is no longer true: regardless of position, detection occurs within the same time frame. Similar to the wave without surfactant, there is a large spike in which a large portion of droplets were observed. However, instead of being located around 65 inches it is now at 76 inches and occurs approximately  $1/10^{\text{th}}$  of a second later.

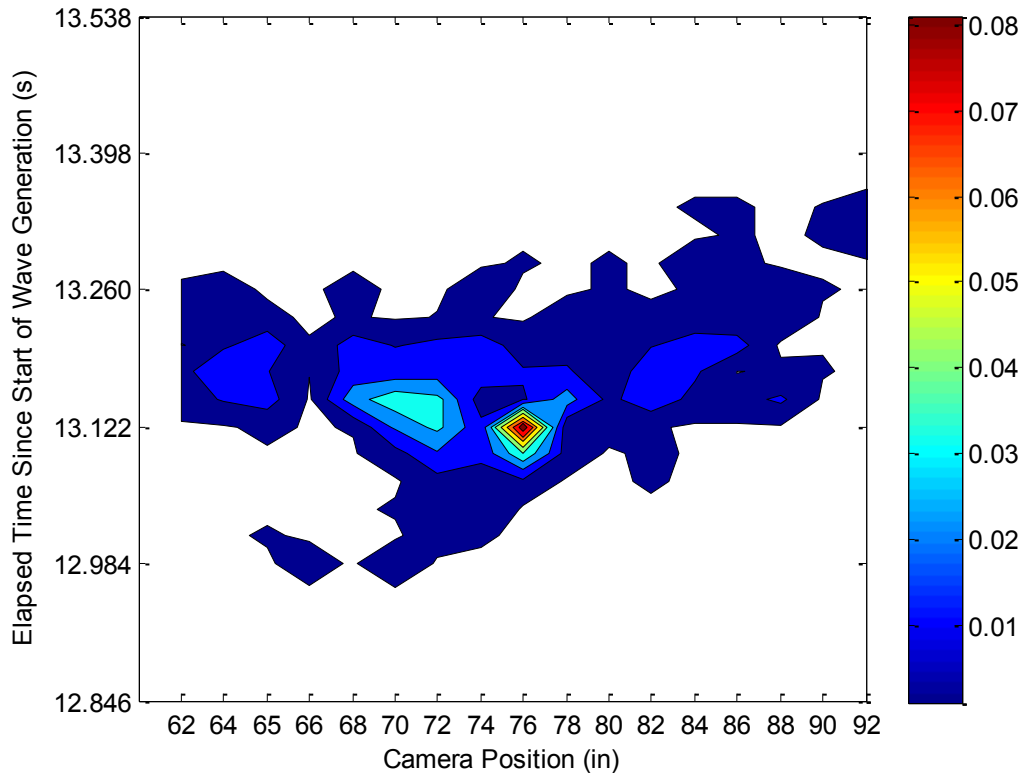


**Figure 6.7: Corrected (focus and depth-of-field), normalized probability density for droplets at 12cm from the free surface in the 0.074 amplitude wave with surfactant.**

Droplet production rates were altered significantly when compared to the wave without surfactant. The peak in production is much wider and reaches its apogee later in time. Overall, the amount of droplets produced per wave after the addition of surfactant was lower for the 0.074 amplitude wave.

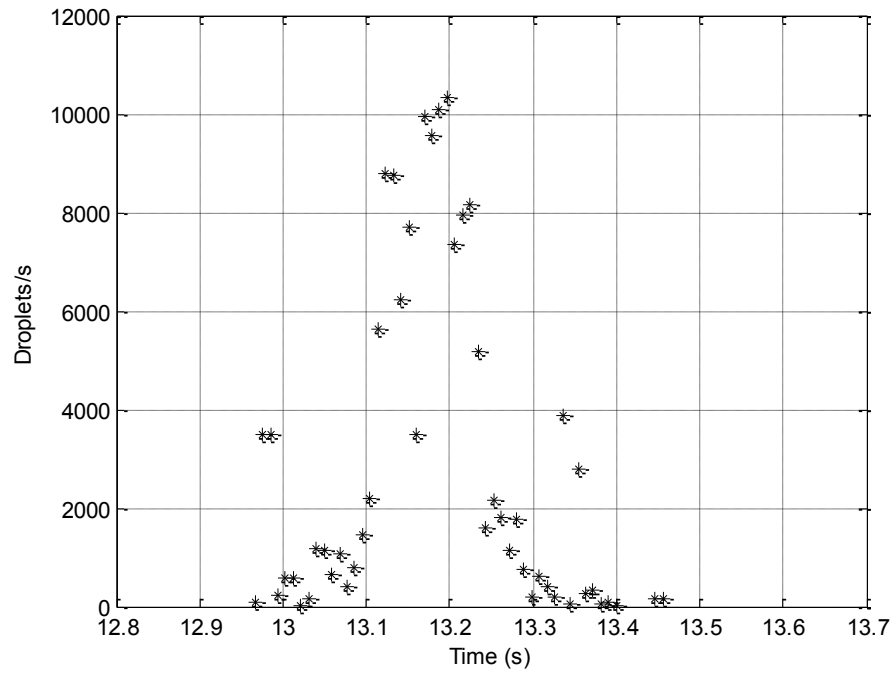


**Figure 6.8: Corrected (focus and depth-of-field) droplet production rate as a function of time for the 0.074 amplitude wave with surfactant.**



## Chapter 7: Wave Comparison and Concluding Remarks

### 7.1 Comparing the 0.074 and 0.070 Amplitude Waves

The droplet diameter distributions were organized in log-log plots. Both waves were plotted together on the same axes in Figure 7.1. Superimposed over the data points are the power laws fits to these distributions. A two power law fits were selected for the steep and shallow slope sections of the 0.074 amplitude wave diameter distribution while a single power law was fit to the 0.070 amplitude wave. These power laws excluded the data points at the extreme low end of droplet diameters due to the aforementioned issues with detecting droplets near the lower limit of image resolution.

The transition between functions occurs at very nearly the same diameter in both waves: 1250  $\mu\text{m}$ . Other than this transition point and the general shape of the distribution, the wave distributions lack similarity. Whereas the stepped shape of the distribution is sharp in the 0.074 amplitude wave, it is much less distinctly defined in the 0.070 amplitude wave. It would be expected, though, that the lower amplitude wave distribution exhibit more error because less than half of the droplets as the other wave were observed over the course of all 16 positions and 10 runs.

A caveat to the use of these power laws is the fact that the piecewise shape of the droplet diameter distributions is confined to the region of the wave in which the breaking action is most violent. Outside of this region, the droplets appear to follow a single power law distribution over the entire range of diameters. In these locations, jet and film droplets may be more prevalent than the splashing droplets that are ejected as a result of the plunging jet impact. However, because the droplets produced as a result of the

breaking event are much more numerous than the droplets observed in other locations, the overall droplet distribution assumes a piecewise shape.

The droplet generation frequency for the lower amplitude wave was frequencies in the lower end of the droplet diameter distribution. For the higher amplitude wave, larger droplets are observed more frequently than in the 0.070 amplitude waves. One potential explanation of this phenomenon is that the higher amplitude wave possessed higher levels of turbulent kinetic energy which produced more massive droplets. What is notable also for the higher amplitude wave is the location of these larger droplets. Whereas the droplet diameter distributions at the further camera positions are similar for both waves, there is a considerable difference between them at the camera positions closest to the location of the plunging jet impact. In the higher amplitude wave, the droplets produced by the plunging jet tend to have much larger diameters than at the other positions. In the lower amplitude wave, since the breaking event is less dramatic, this increase in droplet diameters is not observed.

Overall, it remains to be seen whether or not the amplitude of the wave will consistently have the effect of shifting the diameter distribution in this manner. It may be possible that more energetic waves will produce relatively more droplets at higher diameters and lower amplitude waves will do the opposite.

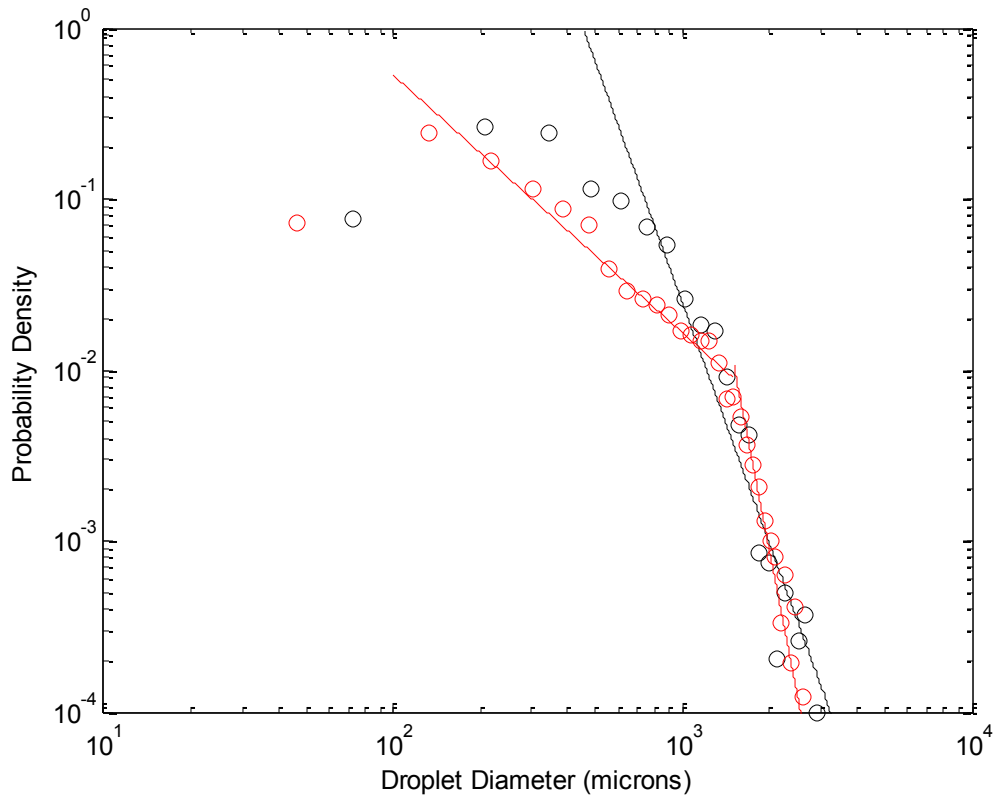


**Figure 7.1: Droplet diameter distributions for the 0.070 (black) and 0.074 (red) amplitude waves. Their respective power laws are fitted over the distributions.**

The fit for the 0.074 amplitude wave was made piecewise whereas the fit for the 0.070 amplitude wave was fitted to a single function of the diameter. Some precedent does exist for piecewise droplet diameter distributions: similar observations were made by Wu (1984). The equations governing the normalized probability density for the diameters encountered in the 0.070 and 0.074 amplitude waves are shown below.

$$f_{0.070} \cong (2.86 * 10^1)d^{-4.68}$$

$$f_{0.074} \cong \begin{cases} (6.30 * 10^0)d^{-1.50} & d < 1250 \mu m \\ (5.97 * 10^1)d^{-8.79} & d > 1250 \mu m \end{cases}$$

When comparing the number of raw droplets observed between the two waves there are considerable differences. Despite all parameters besides the wave amplitude (and height of observation—which was tied to the amplitude) being the same, the shape and total droplet counts are quite dissimilar. A comparison of the total droplet counts between the three wave conditions at the two different intensity cutoffs is shown in Table 7.1 below. The observed droplets at positions beyond 68 inches, however, do coincide fairly well between the waves. The lower amplitude wave even has more droplets present at these positions than the higher amplitude wave. The reason behind this reversal is the delay in the droplet maximum in the lower amplitude wave. The most noticeable disparity, however, is the spike in observed droplets at the first few camera positions on the 0.074 amplitude wave.

**Table 7.1: Comparison of measurable droplets for each wave condition for the two image intensity cutoffs. 3900 was used for the uncorrected droplet statistics and 3500 was used for the statistics corrected for focus and depth-of-field.**

<u>Wave Condition</u>	<u>Measurable Droplets with I &gt; 3900 Cutoff</u>	<u>Measurable Droplets with I &gt; 3500 Cutoff</u>
0.070 Amplitude (10 Runs)	532	608
0.074 Amplitude (10 Runs)	968	1,582
0.074 Amplitude with Surfactant (5 Runs)	380	634

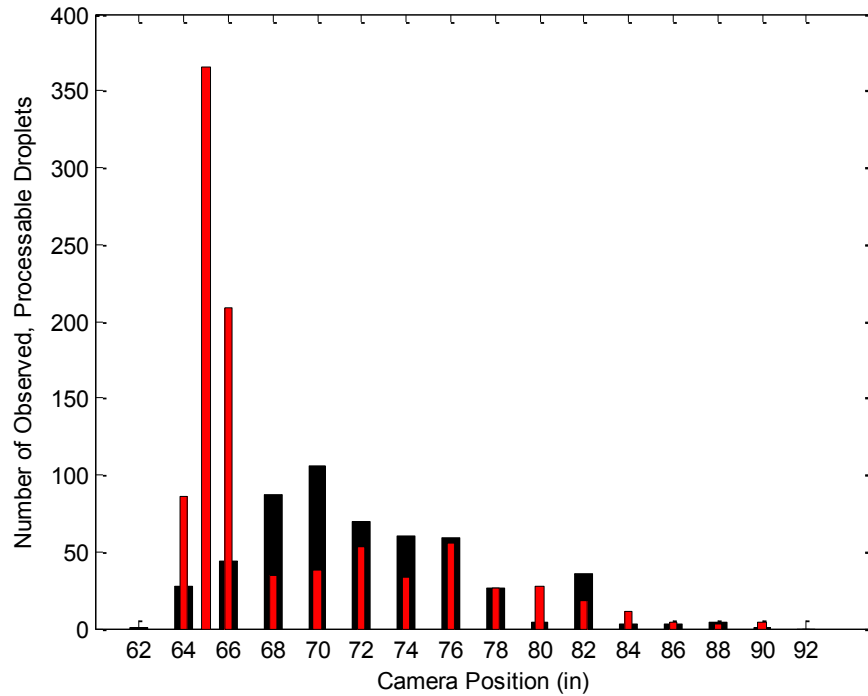


**Figure 7.2: Comparison of number of observed (uncorrected) droplets per position for the 0.074 amplitude (red) wave and the 0.070 amplitude (black) wave.**

Two generalities can be drawn from the droplet measurements: Increasing the non-dimensionalized mechanical wave maker amplitude by 0.004 increased the observed number of droplets by over double and the location of spray droplet generation is more localized for the larger amplitude wave. Also, the larger amplitude waves produced spray with higher concentrations of larger droplets. The distributions of droplets nearest to the plunging jet impact take the shape of a two power laws. Droplets generated outside of this region of intense droplet density follow single power laws.

## 7.2 Comparing the 0.074 Amplitude Wave with and without Surfactant

The diameter distributions for the same wave with and without surfactant are shown in Figure 7.3. Droplets with diameters less than approximately 800  $\mu\text{m}$  are more probably produced by the wave with added surfactant. Beyond 800  $\mu\text{m}$ , the wave with clean water generates larger droplets more often than the wave with surfactant. Additionally, whereas the distribution for the wave generated in clean water showed a piecewise shape, the wave with surfactant was more closely linear beyond 500  $\mu\text{m}$ .

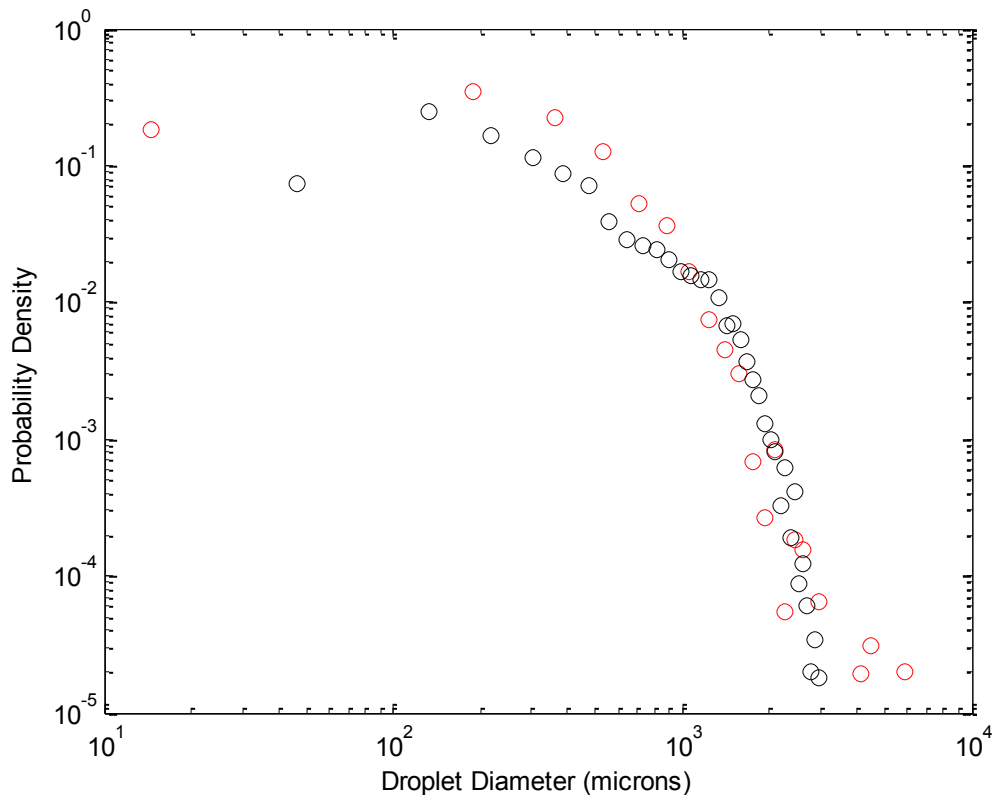


**Figure 7.3: Droplet diameter distributions for the 0.074 amplitude wave with (red) and without (black) surfactant.**

The addition of surfactant resulted in immense changes to the positional distribution. The large spike observed in the clean water wave is absent in the presence of surfactant. The droplets are distributed more uniformly over a much wider range of positions in the surfactant waves. Adding surfactant additionally led to suppression of the overall number of droplets observed per wave, and delayed their observation in time and distance.

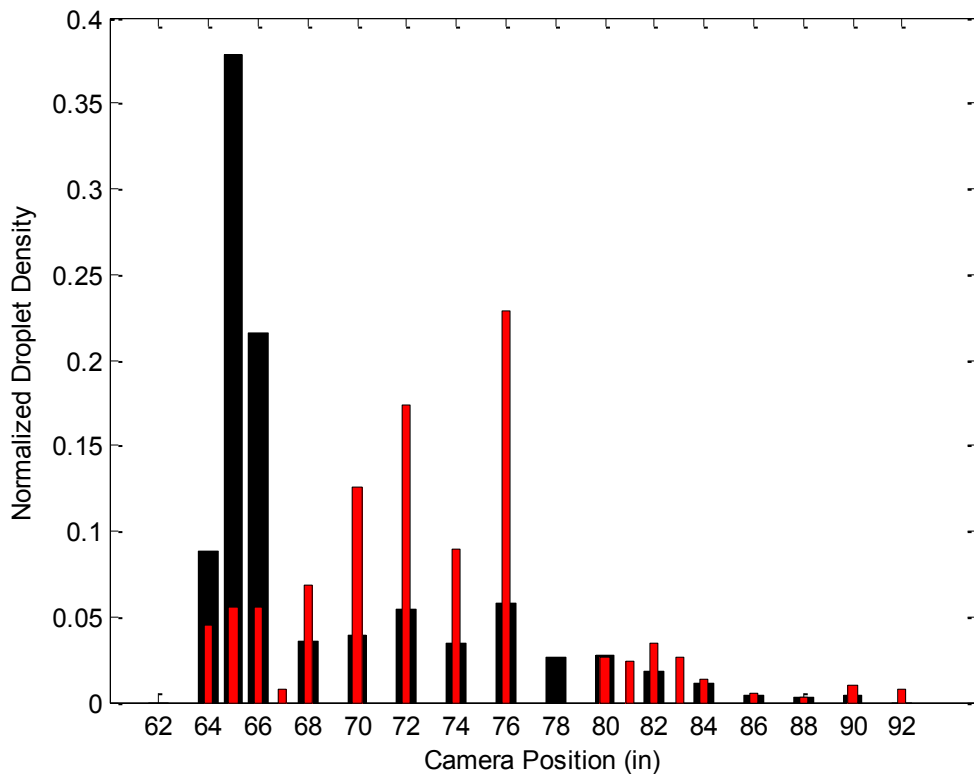


**Figure 7.4: Comparison of uncorrected normalized droplet densities for the 0.074 amplitude wave with (red) and without (black) surfactant.**

### 7.3 Comparing the Three Wave Conditions

A log-log plot of the diameter distribution of all three wave conditions is shown in Figure 7.5. From this it can be seen that the 0.070 amplitude wave was more likely to produce droplets with diameters less than 1,250  $\mu\text{m}$  than the 0.074 amplitude waves. The addition of surfactant, however, to the 0.074 amplitude wave drastically increased the probability of generation for droplets below this threshold and was quite close to the overall shape of the 0.070 amplitude distribution. Droplets less than 100  $\mu\text{m}$  are far more likely to be produced in the 0.074 amplitude in water with surfactant than in the other two waves that were produced in clean water. Unsurprisingly, droplets with diameters greater than 1,250  $\mu\text{m}$  were most commonly produced by the 0.074 amplitude wave in clean water. Additionally, the shapes of the distributions are quite similar, especially above 1,250  $\mu\text{m}$ .



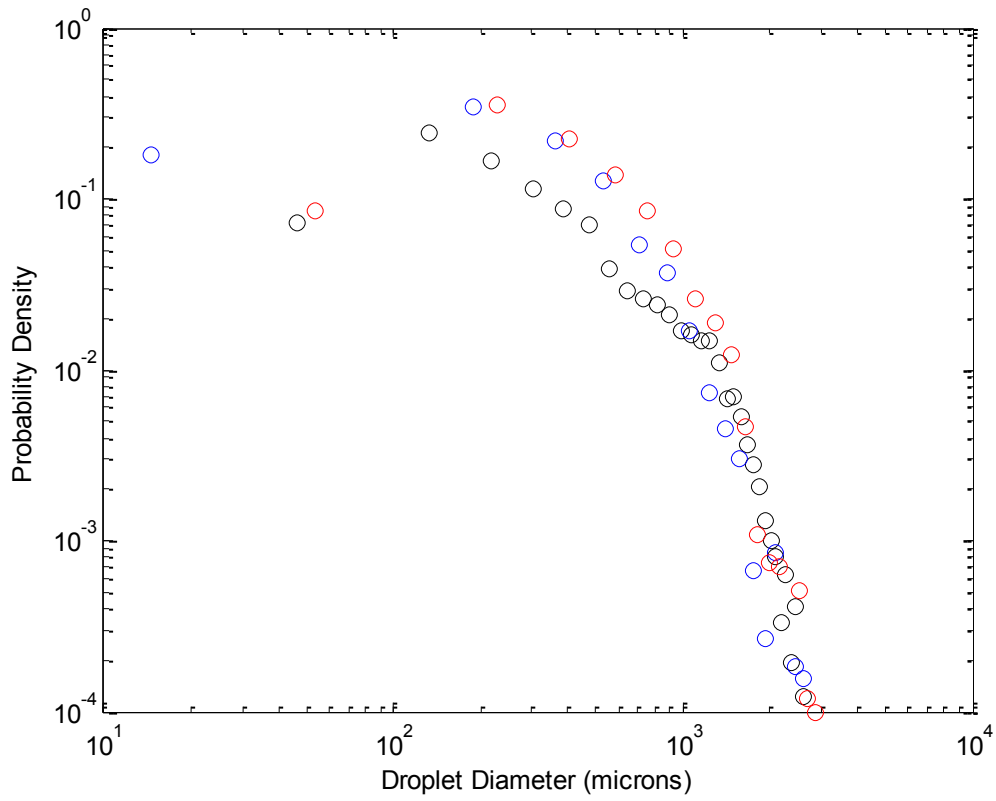


**Figure 7.5: Droplet diameter distributions for the 0.070 wave (red) and the 0.074 wave with (blue) and without (black) surfactant in the wave tank.**

## Bibliography

- Andreas, Edgar L. "A new sea spray generation function for wind speeds up to 32 m s<sup>-1</sup>." *Journal of Physical Oceanography* 28, no. 11 (1998): 2175-2184.
- Andreas, E. and Emanuel, K. (2001). Effects of sea spray on tropical cyclone intensity. *Journal of the atmospheric sciences*, 58(24):3741–3751.
- Barger, W. R., and W. D. Garrett. "Surface active organic material in the marine atmosphere." *Journal of Geophysical Research* 75, no. 24 (1970): 4561-4566.
- Bock, Erik J., Tetsu Hara, Nelson M. Frew, and Wade R. McGillis. "Relationship between air-sea gas transfer and short wind waves." *Journal of Geophysical Research: Oceans* (1978–2012) 104, no. C11 (1999): 25821-25831.
- Bonmarin, P. (1989). Geometric properties of deep-water breaking waves, *J. Fluid Mech.*, 209, 405.
- Cox, Charles, and Walter Munk. "Statistics of the sea surface derived from sun glitter." *J. mar. Res* 13, no. 2 (1954): 198-227.
- Duncan, J. H., V. Philomin, M. Behres, and J. Kimmel. "The formation of spilling breaking water waves." *Physics of Fluids* 6 (1994): 2558.
- Duncan, James H., Haibing Qiao, Vasanth Philomin, and Alexandra Wenz. "Gentle spilling breakers: crest profile evolution." *Journal of Fluid Mechanics* 379 (1999): 191-222.
- Erickson, D., Seuzaret, C., Keene, W., and Gong, S. (1999). A general circulation model based calculation of hcl and clno<sub>2</sub> production from sea salt dechlorination: Reactive chlorine emissions inventory. *Journal of geophysical research*, 104(D7):8347–8372.
- Ermakov, S. A., A. M. Zujkova, A. R. Panchenko, S. G. Salashin, T. G. Talipova, and V. I. Titov. "Surface film effect on short wind waves." *Dynamics of atmospheres and oceans* 10, no. 1 (1986): 31-50.
- Fryinger, Glenn S., William E. Asher, Gerald M. Korenowski, William R. Barger, Mark A. Klusty, Nelson M. Frew, and Robert K. Nelson. "Study of ocean slicks by nonlinear laser processes: 1. Second-harmonic generation." *Journal of Geophysical Research: Oceans* (1978–2012) 97, no. C4 (1992): 5253-5269.
- Hoppel, W. A., Frick, G. M., and Fitzgerald, J. W.: Surface source function for sea-salt aerosol and aerosol dry deposition to the ocean surface, *J. Geophys. Res.-Atmos.*, 107, 4382, doi:10.1029/2001jd002014, 2002.

- Johnson, J. W., and W. F. Crosswell. "Characteristics of 13.9 GHz radar scattering from oil films on the sea surface." *Radio Science* 17, no. 3 (1982): 611-617.
- Liss, P. S., A. J. Watson, E. J. Brock, B. Jahne, W. E. Asher, N. M. Frew, L. Hasse et al. "Report of group I—physical processes in the microlayer and the air-sea exchange of trace gases." *The sea surface and global change*. Cambridge University Press, Cambridge, p1 (1997).
- Liu, Xinan, and James H. Duncan. "The effects of surfactants on spilling breaking waves." *Nature* 421, no. 6922 (2003): 520-523.
- Liu, Xinan, and James H. Duncan. "An experimental study of surfactant effects on spilling breakers." *Journal of Fluid Mechanics* 567 (2006): 433.
- Melville, W. K., and Ronald J. Rapp. "The surface velocity field in steep and breaking waves." *J. Fluid Mech* 189, no. 1 (1988).
- Monahan, E. (1968). Sea spray as a function of low elevation wind speed. *Journal of Geophysical Research*, 73(4):1127–1137.
- Norris, S. J., I. M. Brooks, B. I. Moat, M. J. Yelland, G. de Leeuw, R. W. Pascal, and B. Brooks. "Near-surface measurements of sea spray aerosol production over whitecaps in the open ocean." *Ocean Science* 9, no. 1 (2013): 133-145.
- Qiao, Haibing, and James H. Duncan. "Gentle spilling breakers: crest flow-field evolution." *Journal of Fluid Mechanics* 439, no. 1 (2001): 57-85.
- Rapp, R. J., and W. K. Melville. "Laboratory measurements of deep-water breaking waves." *Philosophical Transactions of the Royal Society of London. Series A, Mathematical and Physical Sciences* (1990): 735-800.
- Sellegrri, K., C. D. O'Dowd, Y. J. Yoon, S. G. Jennings, and Gerrit de Leeuw. "Surfactants and submicron sea spray generation." *Journal of geophysical research* 111, no. D22 (2006): D22215.
- Tang, Shih, and Jin Wu. "Suppression of wind-generated ripples by natural films: A laboratory study." *Journal of Geophysical Research: Oceans* (1978–2012) 97, no. C4 (1992): 5301-5306.
- Wang, Y., Kepert, J., and Holland, G. (2001). The effect of sea spray evaporation on tropical cyclone boundary layer structure and intensity. *Monthly weather review*, 129(10):2481–2500.
- Wu, J., Murray, J., and Lai, R. (1984). Production and distributions of sea spray. *Journal of Geophysical Research*, 89(C5):8163–8169.

Wu, J. (1993), Production of spume drops by the wind tearing of wave crests: The search for quantification, *J. Geophys. Res.*, 98(C10), 18221–18227, doi:10.1029/93JC01834.